ECN

Energy research Centre of the Netherlands

IEA Annex XX: Comparison between calculations and measurements on a wind turbine in the NASA-Ames windtunnel

J.G. Schepers

ECN-E--07-066

Acknowledgement

'Financial support for this research was given in part by Senter-Novem, Project: 'IEA Annex XX: Analysis of NASA-Ames wind tunnel measurements' Project Reference: 2020-02-11-10-005. ECN project number: 74189.

This project could not be performed without the supply of data by the National Renewable Energy Laboratory, NREL in the USA, where in particular the support from Scott Schreck is highly appreciated.

Abstract

This report describes a study in which calculational results from ECN's aeroelastic code PHATAS and the free wake lifting line code AWSM are compared with wind tunnel measurements which were carried out by NREL on a wind turbine, placed in the large NASA-Ames wind tunnel.

Measurements have been taken at a large variety of conditions but in this report data at non-yawed conditions are considered only.

The study was carried out within the framework IEA Annex XX 'Analysis of NASA-Ames wind tunnel measurements'.

Summary

In this report an investigation is described, which forms part of IEA Annex XX. IEA Annex XX is an international cooperation between several parties from 7 countries, coordinated by the National Renewable Energy Laboratory, NREL from the USA. The main aim of IEA Annex XX is to analyse the measurements which were performed by NREL on a wind turbine placed in the large (24.4x36.6m) NASA-Ames wind tunnel. This wind turbine was 2-bladed and it had a rotor diameter of 10 meter. One of the blades was instrumented with pressure taps at 5 radial positions to measure the local pressure distribution and the resulting sectional aerodynamic loads. A large number of measurements at very different conditions were stored into a database and made accessible to the IEA Annex XX participants. In the present study calculational results from ECN's aeroelastic code PHATAS and the free wake lifting line code AWSM are compared with measurements at non-yawed conditions where the tunnel speed ranges between 5 and 25 m/s and where the pitch angle varies between 0 and 6 degrees. Calculations from the AWSM code have only been performed for low tunnel speeds (5, 7 and 9 m/s). The comparison between calculations and measurements is based on dimensional aerodynamic loads by which the uncertainty in dynamic pressure and angle of attack, which often complicates the interpretation of aerodynamic wind turbine measurements, does not play a role.

The most important conclusions from the present study are:

- Most investigated loads are predicted well with PHATAS as long as the tunnel speed is relatively low (say below 10-12 m/s which corresponds to an angle of attack below the stall angle of attack). The most pronounced exception is the overprediction of the normal force at the most outboard position (95% span);
- At higher tunnel speeds, the PHATAS code underpredicts the normal forces and overpredicts the tangential forces. The discrepancies are most likely caused by 3D effects in stall. The latter observation implies the prediction of too strong a force towards the leading edge. It indicates that the 3D correction from [5] as implemented in PHATAS yields a too low increase in lift coefficient, where at the same time the drag should be increased. It is noted that similar observations were found in the Annexlyse project where field measurements on different turbines were analysed, see [6]. The empirical corrections which have been derived for those measurements lead, for the present configuration, to an 'overcorrected' lift increase and drag increase. It is also noted that part of the discrepancies can be caused by the uncertainty of the basic 2D aerodynamic coefficients at stalled conditions;
- The overpredicted tangential force is reflected into an overprediction of the rotor shaft torque at the high tunnel speeds. The underpredicted normal force is reflected into an underpredicted flatwise moment;
- The calculations from the AWSM code (which are only done at a low tunnel speed) show a good agreement with the measured loads. Even at the 95% span the agreement is reasonable and better than the agreement from the corresponding PHATAS calculation. The added value of ASWM mainly lies on a better prediction of the induction by which the improvement from AWSM is limited at high tunnel speeds;

Contents

Notations

a	axial induction factor	-
c	chord	m
c_{d}	profile drag coefficient	-
c_{l}	profile lift coefficient	-
c_{m}	profile moment coefficient	-
f_{cl}	factor in 3D correction for lift coefficient	-
n	normal force (normal to the chord) per unit length	N/m
M_{flat}	flatwise moment (perpendicular to tip chord)	Nm
M_{torq}	rotorshaft torque	Nm
r	radial position relative to rotor centre	m
t	tangential force (tangential to the chord) per unit length	N/m
V_{tun}	tunnel speed	m/s
α	angle of attack	deg
θ	pitch angle	deg
σ	standard deviation	

index

2D	two dimensional (non-rotating) value
3D	three dimensional (rotating) value

1 Introduction

This report describes a validation of ECN's wind turbine codes PHATAS, [3] and AWSM, [1]. The study is carried out within IEA Annex XX. IEA Annex XX is an international cooperation between several parties from 7 countries, coordinated by the National Renewable Energy Laboratory, NREL from the USA. The main aim of IEA Annex XX is to analyse the measurements which were performed by NREL on a wind turbine placed in the large (24.4x36.6m) NASA-Ames wind tunnel. This wind turbine was 2-bladed and it had a rotor diameter of 10 meter. One of the blades was instrumented with pressure taps at 5 radial positions to measure the local pressure distribution and the resulting sectional aerodynamic loads. A large number of measurements at very different conditions were stored into a database and made accessible to the IEA Annex XX participants.

The present set of measurements offers a unique base for validation of wind turbine design codes. An important advantage lies in the fact that aerodynamic forces are measured at different radial positions, by which local quantities can be validated. Usually wind turbine codes need to be validated with measurements of integrated blade and rotor loads which hide the details on sectional level. As a matter of fact, local aerodynamic loads were also measured in IEA Annex XVIII, [7], but these measurements were taken on turbines in the free atmosphere, where the uncertainty due to the instationary, inhomogeneous and uncontrolled wind conditions formed an important problem (as it is in all field measurements). Hence a very important additional advantage of the present measurements lies in the wind tunnel environment, which yields (almost) stationary and homogeneous conditions. The huge size of the wind tunnel allows a rotor diameter of 10 m, with little blockage effects. Obviously this rotor diameter is still (much) smaller than the diameter of the nowadays commercial wind turbines, but nevertheless the blade Reynolds number (in the order of 1 Million) is sufficiently high to make the aerodynamic phenomena at least to some extent representative for modern wind turbines.

NREL performed measurements at very different conditions, but in this report the measurements which have been taken at non-yawed flow are selected for comparison with the above mentioned PHATAS and AWSM codes. In other ECN reports, measurements at yawed flow and at fast pitching steps are analysed. The PHATAS code is a wind turbine design code taking into account structural dynamic effects. The aerodynamic modelling of PHATAS relies on the relatively simple blade element momentum theory where several empirical models are added, among others to account for stall aerodynamics. The aerodynamic model of the AWSM code is based on a free wake lifting line model. Such model represents the wake physics, and the resulting induction, in a much more realistic way. On the other hand, AWSM does not account for structural dynamic effects and for stall effects.

The measurements and the calculational codes are described in section 2 and 3. Then the comparison on the normal forces, the tangential forces and the rotorshaft torque and flatwise moment is given in the sections 4.1, 4.2 and 4.3. Most of the measurements have been taken at stalled conditions where a correction needs to be added for rotational effects. The effect of this 3D correction is discussed in section 5.

2 Description of measurements

A detailed description of the experimental set-up and the available measurements is given by NREL in [9].

2.1 Wind tunnel, wind turbine and instrumentation

A picture of the wind turbine placed in the NASA-Ames wind tunnel test section is shown in Figure 1. The wind tunnel is located in the NASA-Ames Research Center. The tunnel is open loop with a closed test section of 24.4x36.6 m. The tunnel speed is variable between almost zero and 50 m/s, where the minimum speed for the present measurements was 5 m/s and the maximum speed was 25 m/s. As noted in [11] the turbulence levels decrease with tunnel speed. At a tunnel speed of 5 m/s the turbulence intensity is in the order of 2.5 % and it decreases to 0.2% at a tunnel speed of 24 m/s.

The main characteristics of the turbine are as follows:

- The rotor diameter is 10 m. This implies that 9% of the test section area is covered by the rotor swept area. This is below the 10% which is commonly considered to be acceptable for closed wind tunnel test sections. In [9] it is noted that the maximum blockage can be in the order of 2% but for the majority of the cases, the blockage is less than 1%;
- The turbine is 2-bladed (with blade numbers given as number 1 and **3**, note that blade number 3 is the instrumented blade).
- The blades have a linear taper with a maximum chord of 0.737 m at 25% span and 0.356m at 100% span. As already pointed out in [2] this results in a relatively low aspect ratio and high solidity compared to modern (2 bladed) wind turbines.
- The blades have a non-linear twist of 22.5 degrees over the blade.
- The airfoil is the S809 profile over the entire span.
- The turbine has an asynchronous generator with a rated rotor speed of 72 rpm. For a 10 m rotor and for the present tunnel speeds, this results in a relatively low tip speed ratio.

One of the blades (blade number 3) was heavily instrumented at 5 radial positions with 22 pressure taps each. The measurement sections (relative to the rotor centre) are located at 30%, 47%, 63%, 80% and 95% span, i.e. at r= 1.510 m, 2.343 m, 3.185 m 4.023 m and 4.780 m. The resulting pressure distributions are integrated to normal forces and tangential forces. It should be noted however, see [6], that the integration to tangential forces is rather inaccurate due to the limited number of pressure taps.

In addition the inflow velocities and inflow angles are measured from five hole probes. These probes were placed 4% outboard of the pressure taps, i.e. at r= 1.710 m, 2.5653m, 3.370 m and 4.225 m and 4% inboard of the outer station, i.e. at r=4.5773 m.

2.2 Selected measurements

NREL performed measurements for a large variety of conditions (tunnel speeds, pitch angles and yaw angles) and different configurations (upwind, downwind, teetered, non-teetered). The data are stored on a (password protected) database.

In the present study the measurements at non-yawed conditions from the so-called H, I and J sequences have been considered. In these sequences the rotor is rigid (i.e. non-teetered) and located upwind from the tower. The difference between the sequences lies in the pitch angle: The pitch angle for the H sequence is 'nominal', i.e. 3 degrees. The pitch angle for the I sequence is 0 degrees and the pitch angle for the J sequence is 6 degrees. For every sequence, time series have been selected at tunnel speeds which vary between 5 and 25 m/s with a 1 m/s interval.

The identification of the measurement cases remained similar to the identification used by NREL, i.e. the cases are denoted through 'Hxx00000', 'Ixx00000' and 'Jxx00000'. In these identifications 'xx' refers to the tunnel speed (hence xx varies between 05 and 25), and H, I and J refer to the above mentioned measurement sequence (i.e. pitch angle).

In the analysis of the results, it is important to have a global idea on the local aerodynamic conditions at the different campaigns. Thereto the PHATAS calculational code (see section 3.1) has been used to calculate the axial induction factor and the angle of attack at 3 radial positions (30% or 47% span, 63% span and 80% span). The results are shown graphically as function of tunnel speed and the three pitch angles in Figures 2 and 3. As expected the angle of attack increases with tunnel speed and it decreases with pitch angle and radial position. At a tunnel speed of 10 m/s, most angles of attack have already exceeded the (2D) stalling angle of attack of $\approx$ 10 degrees. Furthermore substantial induction factors are only found at a tunnel speed of 5 m/s and a pitch angle of zero degrees. At a tunnel speed of 10 m/s the axial induction factors are between 0,1 and 0.15 and at 15 m/s the induction factors are even maller than 0.1.

Finally it is noted that the present report mainly addresses averaged quantities over the measurement period of 30 seconds.

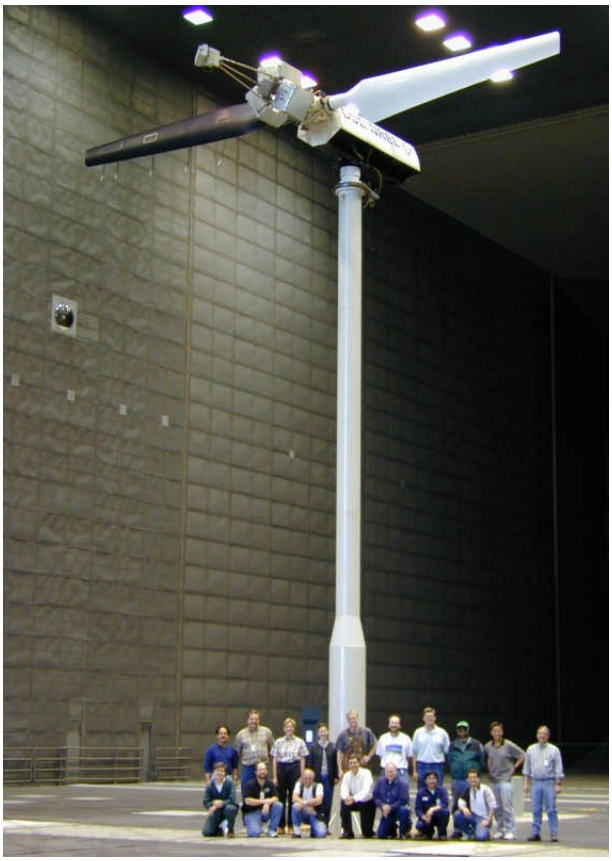

Figure 1: Wind turbine in wind tunnel

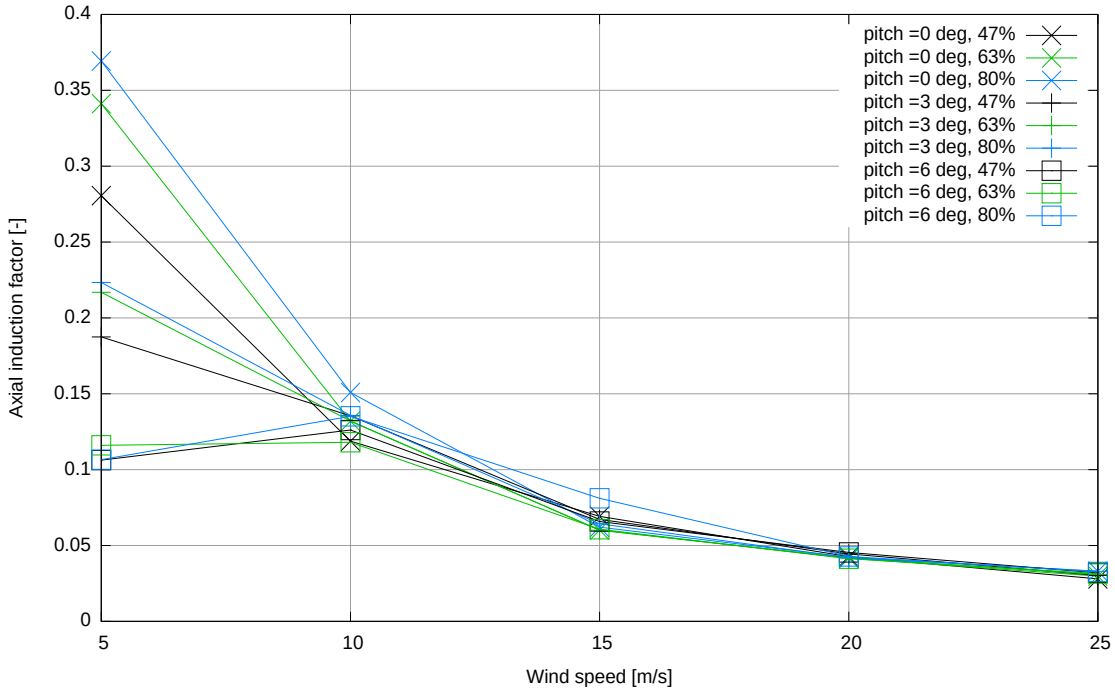

Figure 2: PHATAS calculation: Axial induction factor as function of tunnel speed, pitch angle and percentage of span

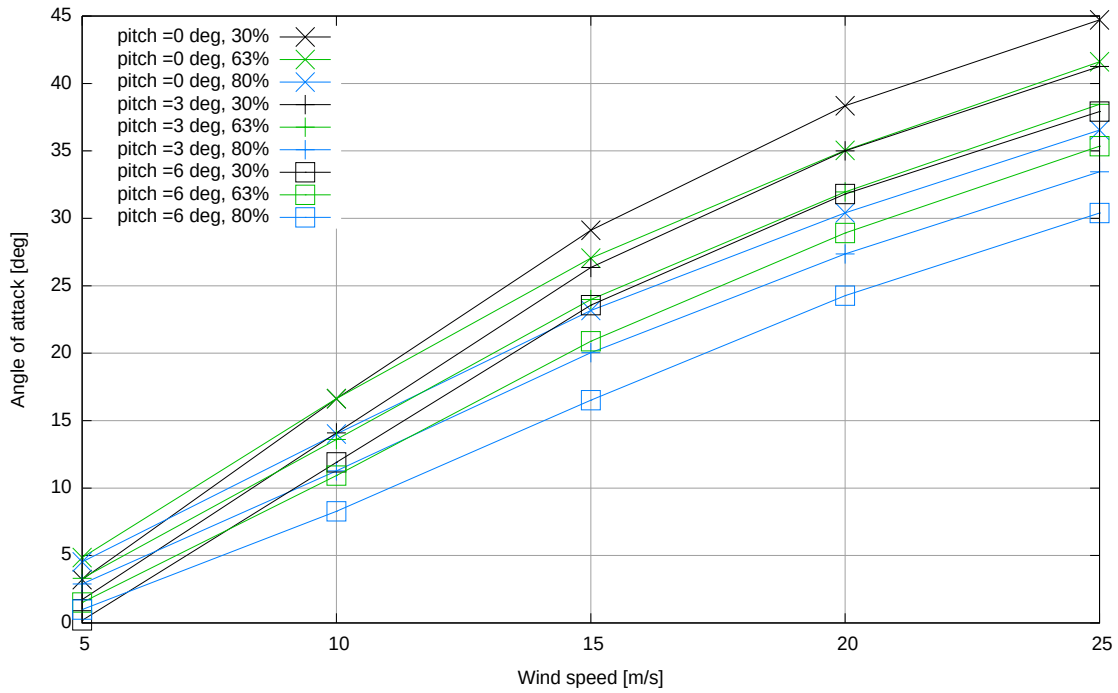

Figure 3: PHATAS calculation: Angle of attack as function of tunnel speed, pitch angle and percentage of span

3 Calculational codes

The measurements which were described in section 2.2 have been compared with calculational results from two of ECN's codes:

- The aero-elastic wind turbine design code PHATAS, see [3]. This code has been used to calculate all the measurement cases.
- The free wake lifting line code AWSM [1]. This code has been used to calculate the cases at low tunnel speeds. For high tunnel speeds (say tunnel speeds $>$ 10 m/s), the angle of attack exceeds the stall angle of attack where, in principle, AWSM does not account for stall effects. Furthermore it must be noted that the potential advantage of AWSM lies in its calculation of induction. As such, a comparison between AWSM and the measurements makes most sense for conditions where the induction is relatively large, i.e. for low tunnel speeds, see Figure 2.

3.1 PHATAS

The calculations in the present report have been performed with a PHATAS release "Apr-2005". This version of the code is described in [3]. The aerodynamic modelling of this version is reported in chapter 5 of [2].

The following remarks can be made on the PHATAS simulations:

- The input on the NREL wind turbine is based on the description given in [2]. Several degrees of freedom are taken into account, e.g. the blade flexibility in the edgewise and flatwise direction, blade torsion, shaft torsion and the dynamics of the tower. Furthermore the asynchronous generator has been modelled;
- The tunnel speed is assumed to be homogeneous and constant in time. Tower shadow has been included;
- The pitch angle is assumed to be constant;
- The calculations have been performed over a period of 20 s;
- The aerodynamic modelling of PHATAS is based on the blade element momentum theory. This requires tables of aerodynamic characteristics (i.e. $\mathrm{c_l}(\alpha)$, $\mathrm{c_d}(\alpha)$ and $\mathrm{c_m}(\alpha)$). It is recalled from section 2.1 that the aerodynamic airfoil along the blade is the NREL S809 profile. The 2D, stationary (non-rotating) aerodynamic characteristics of this airfoil have been constructed by combining wind tunnel measurements from the University of Delft with wind tunnel data from Ohio State University. The data have been extended to deep stall according to the methodology as described in chapter 2 of [2]. The resulting 2D aerodynamic characteristics are presented in Figures 4 and 5;
- In the sequel much attention will be paid to the modelling of 3D effects in stall. These effects are accounted for by the model from [5], where a factor $\mathrm{f_{cl}}$ is used to correct the above mentioned 2D lift coefficients ($\mathrm{c_{l,2D}}$). The factor $\mathrm{f_{cl}}$ is the ratio of the actual increase in $\mathrm{c_l}$ (i.e. $\mathrm{c_{l,3D}} - \mathrm{c_{l,2D}}$) and the difference $\mathrm{dc_l}$ between the non-viscous lift coefficient, $\mathrm{c_{l,potential}}$ (with 'potential' slope $\mathrm{dc_l/d}\alpha$ =2π) and the 2D value of $\mathrm{c_{l,2D}}$. Hence:

  $$\mathrm{c_{l,3D}} = \mathrm{c_{l,2D}} + \mathrm{f_{cl}} \cdot (\mathrm{c_{l,potential}} - \mathrm{c_{l,2D}}) \tag{1}$$

  The factor $\mathrm{f_{cl}}$ is given by

  $$\mathrm{f_{cl}} = 3 \cdot (\mathrm{c/r})^2 \tag{2}$$

  Note that the method only corrects the lift coefficients and not the drag and the moment coefficients;
- Dynamic stall is modelled with the first order dynamic stall model from [4]. Again it is only the lift which is corrected.

3.2 AWSM

The AWSM code, see [1], is based on a non-linear lifting line vortex wake model. The code is of a free wake character but for distances larger than 4 rotor diameters downstream of the rotor, the wake is assumed to be 'frozen'.

The blades are modelled as lifting lines. This implies that, similar to the PHATAS code, aerodynamic profile data should be prescribed as function of the angle of attack. Thereto the same airfoil data as used in PHATAS have been applied. 3D and dynamic stall corrections are not taken into account (although instationary effects which result from the shed vorticity are modelled). In principal a 3D stall correction could be added to the airfoil characteristics, but AWSM has only been used to simulate low tunnel speed cases, for which stall corrections are less relevant.

The AWSM calculations were made under the following assumptions:

- The construction is assumed to be rigid and mass induced loads are neglected;
- The wind speed is constant in time and homogenous. The aerodynamic tower shadow effect has been neglected;
- The rotor speed and pitch angle are constant;
- The calculations have been performed over a period of 11 seconds.

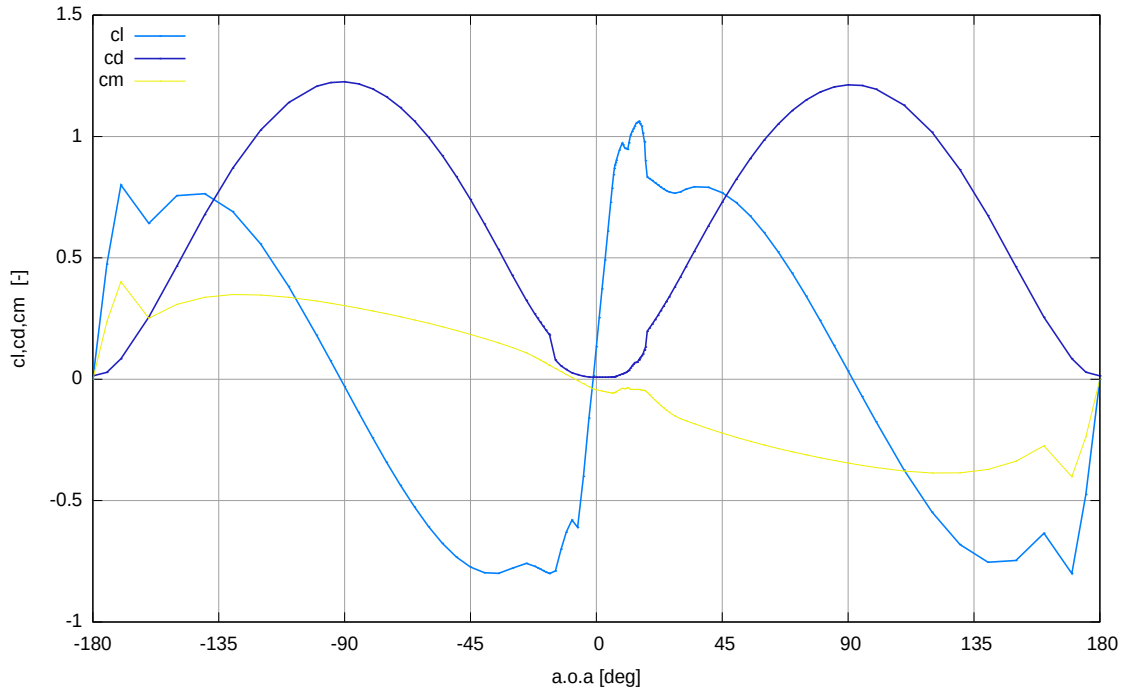

Figure 4: S809 airfoil: Basic 2D aerodynamic coefficients for -180 < α < 180

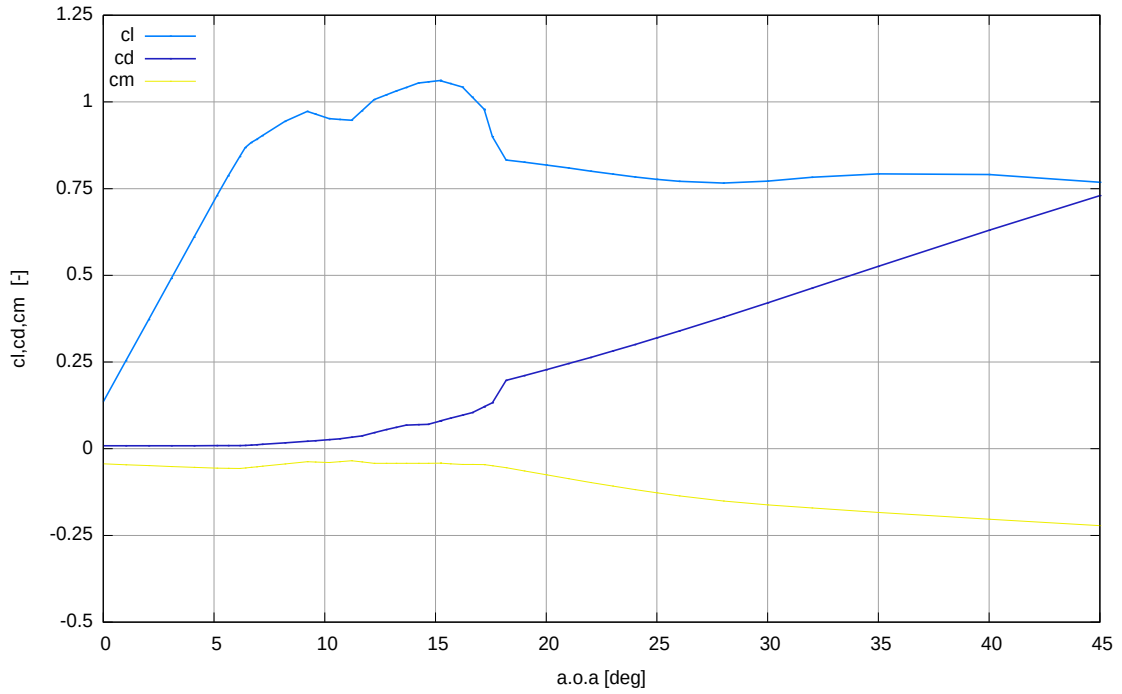

Figure 5: S809 airfoil: Basic 2D aerodynamic coefficients for 0 < α < 45

4 Comparison between calculated and measured results

In this section a comparison is made between calculated and measured results. Thereto the mean blade segment loads (normal and tangential forces), the flatwise moment at the blade root and the rotorshaft torque are considered in the sections 4.1, 4.2 and 4.3. It is emphasized that the present comparison is based on dimensional quantities which are calculated at given external conditions (although the comparison on normal and tangential force is made in terms of $\mathrm{c_n}(\mathrm{c_t})\cdot 0.5\rho \mathrm{V}^2$ which differ from the actual normal and tangential force through the (constant) value of the chord).

Such comparison avoids the uncertainty in the measured angle of attack and dynamic pressure which is commonly experienced when the comparison is made in terms of dimensionless aerodynamic characteristics as function of the angle of attack.

Much attention will be paid to 3D effects which occur at stalled conditions, which are accounted for by the equations 1 and 2. The observations and conclusions on these effects will be summarized in section 4.4.

4.1 Normal forces

In this section the analysis of the sectional normal forces is given. In sections 4.1.1 the mean calculated and measured normal forces as function of tunnel speed and pitch angle are presented, where the calculated and measured results are given in separate figures. In section 4.1.2 the calculated and measured results are compared by presenting the ratios between the calculated and measured normal forces. It is noted that the sections 4.1.1 and 4.1.2 only consider calculational results from the PHATAS code. In section 4.1.3 the normal forces are presented as function of radial position for a limited number of tunnel speeds. This comparison also includes results from the AWSM code. Finally section 4.1.4 compares some PHATAS calculated azimuthally binned averaged normal forces with the corresponding measured results.

4.1.1 Measured and (PHATAS) calculated normal forces as function of tunnel speed and pitch angle

In Figures 6, 8, 10, 12 and 14, the measured normal forces are presented as function of tunnel speed for the 3 pitch angles considered. In Figures 7, 9, 11, 13 and 15, the corresponding results obtained with PHATAS are plotted. It must be noted that the results are averaged over the calculational/measurement period. In order to get an indication for the variations in normal force during the measurement time series, table 1 gives the ratio between the standard deviation (σ_n) and the mean value ($\overline{\mathrm{n}}$) for some of the H-cases (at θ = 3 degrees). In section 4.1.4 some azimuthally averaged normal forces are presented which also give an indication for the variation of the loads over a revolution.

A more detailed discussion on the comparison between calculated and measured normal forces is given in section 4.1.2 but at first sight the following global observations can already be given:

- Some qualitative differences (i.e. differences in shape) between the calculated and measured $\mathrm{n}(\mathrm{V_{tun}})$ curves are very obvious at all spanwise positions, compare e.g. Figure 10 with Figure 11;
- At 30% span the measured normal forces are much higher than the calculated values, at least for the high tunnel speeds. It is also remarkable to see that the measured normal force at 30% span is higher than the value at 47% and 63% span, despite the lower rotational speed at 30% span;
- It can be noted that, generally speaking, the calculated curves show little dependency on the pitch angle at the higher tunnel speeds, i.e. the calculated normal force at θ = 0 degrees is often very close to the calculated normal force at θ = 6 degrees. The measured curves show a much stronger dependency on the pitch angle;

Tunnel speed (m/s)	$\sigma_{n,30}/\overline{n_{30}}$ [-]	$\sigma_{n,47}/\overline{n_{47}}$ [-]	$\sigma_{n,63}/\overline{n_{63}}$ [-]	$\sigma_{n,80}/\overline{n_{80}}$ [-]	$\sigma_{n,95}/\overline{n_{95}}$ [-]
5.0	0.07	0.04	0.03	0.03	0.04
10.0	0.05	0.05	0.06	0.02	0.01
15.0	0.06	0.05	0.08	0.12	0.06
20.0	0.08	0.09	0.10	0.17	0.08
25.0	0.07	0.06	0.05	0.16	0.07

Table 1: Ratio of standard deviation of the measured normal force and its mean value at a pitch angle of 3 degrees

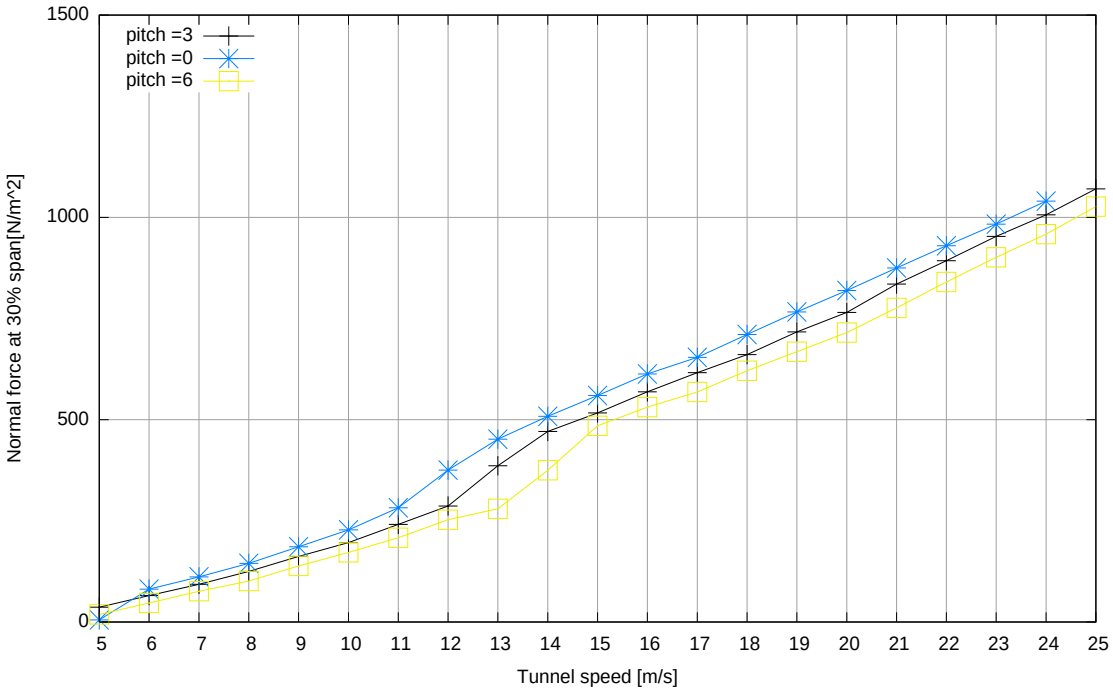

Figure 6: Measured normal force as function of tunnel speed for 30% span

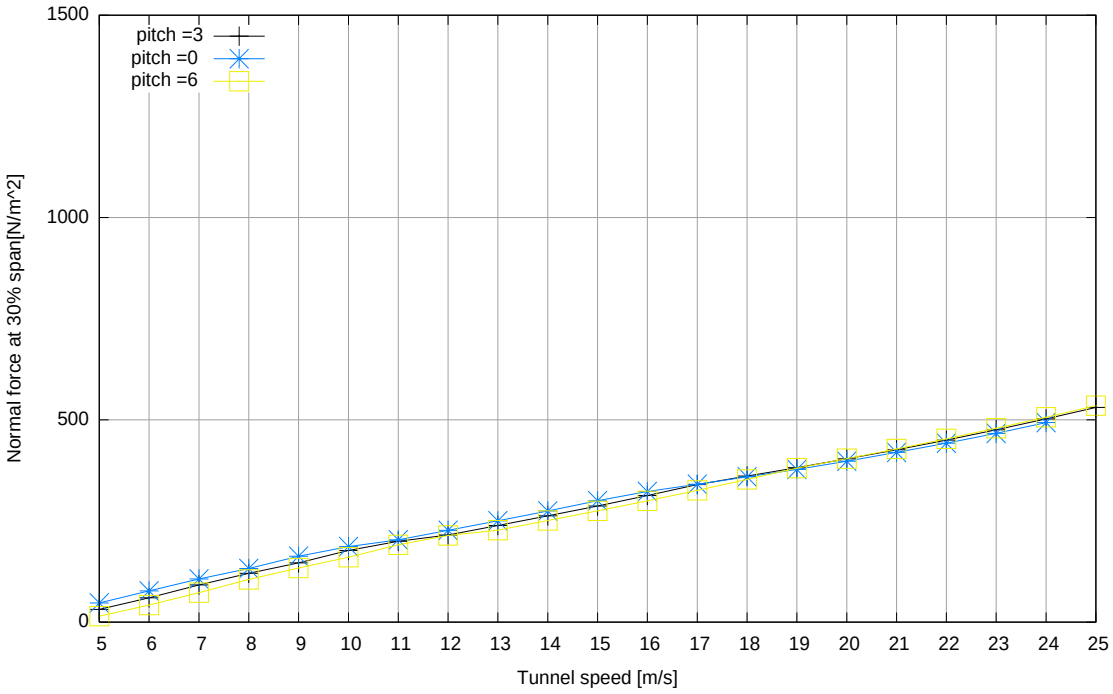

Figure 7: Calculated normal force as function of tunnel speed for 30% span

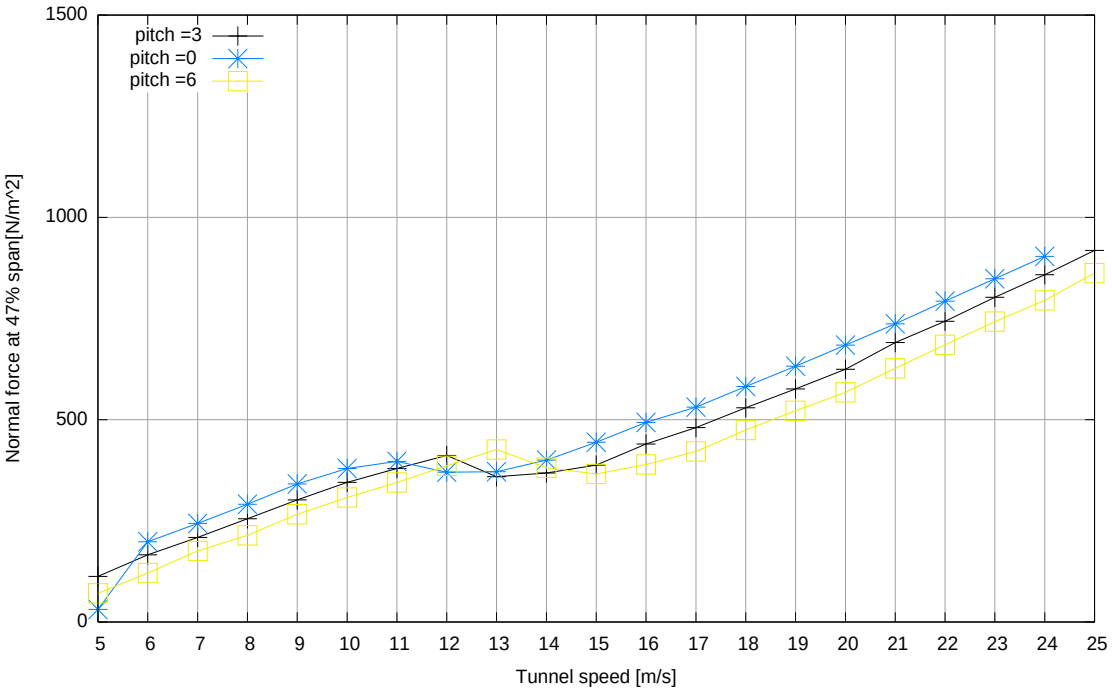

Figure 8: Measured normal force as function of tunnel speed for 47% span

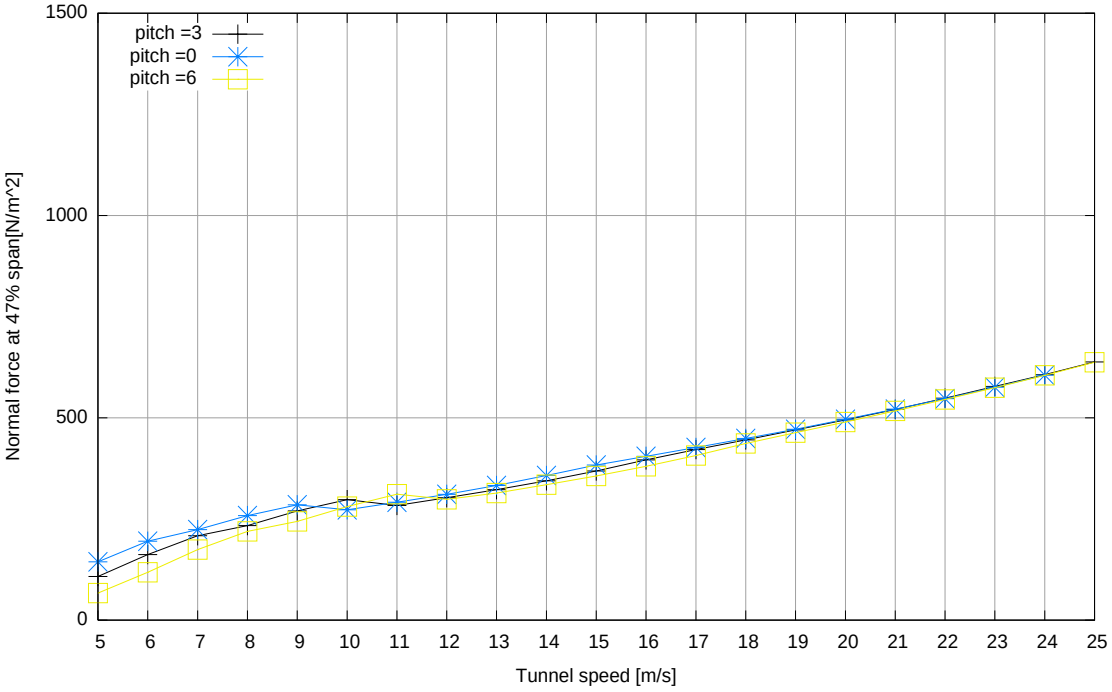

Figure 9: Calculated normal force as function of tunnel speed for 47% span

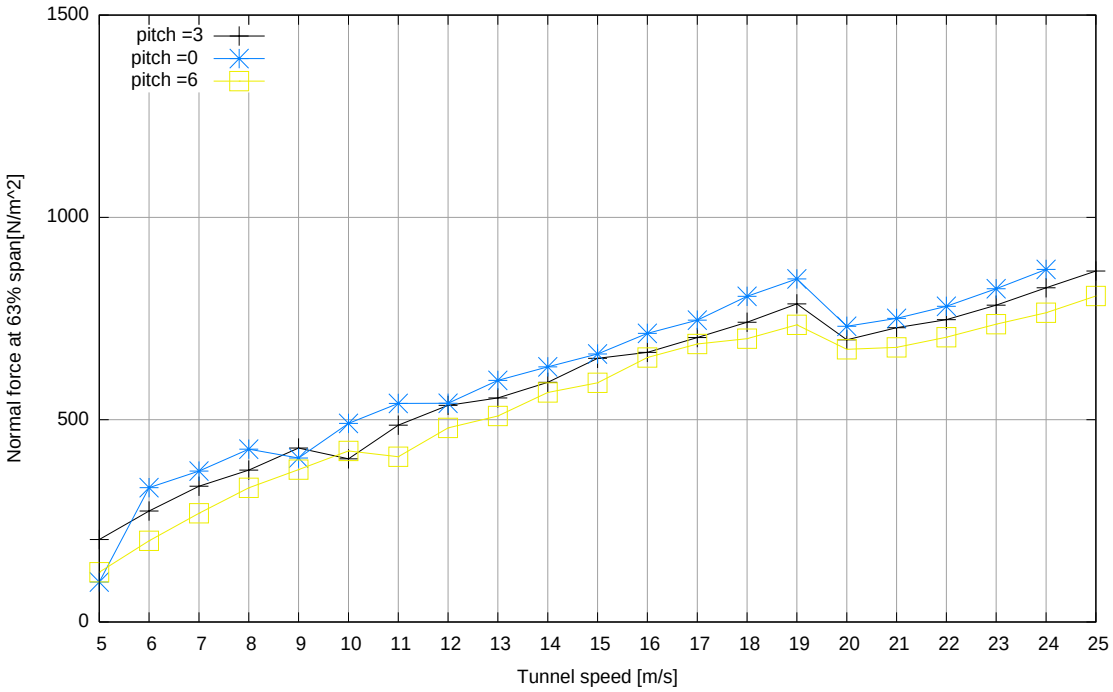

Figure 10: Measured normal force as function of tunnel speed for 63% span

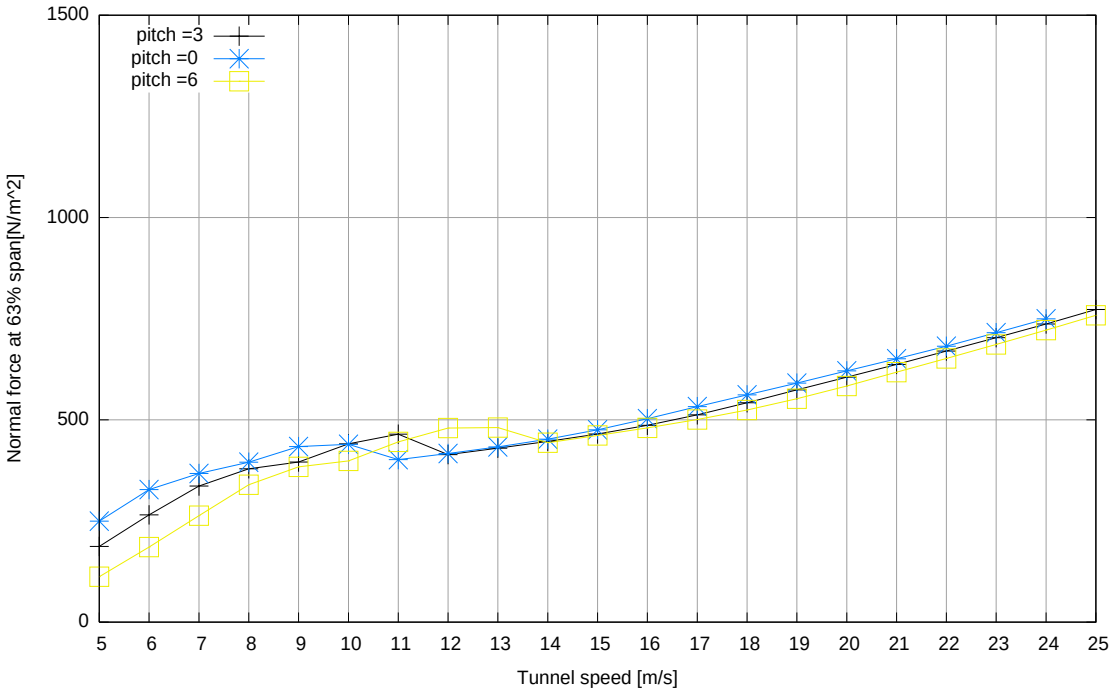

Figure 11: Calculated normal force as function of tunnel speed for 63% span

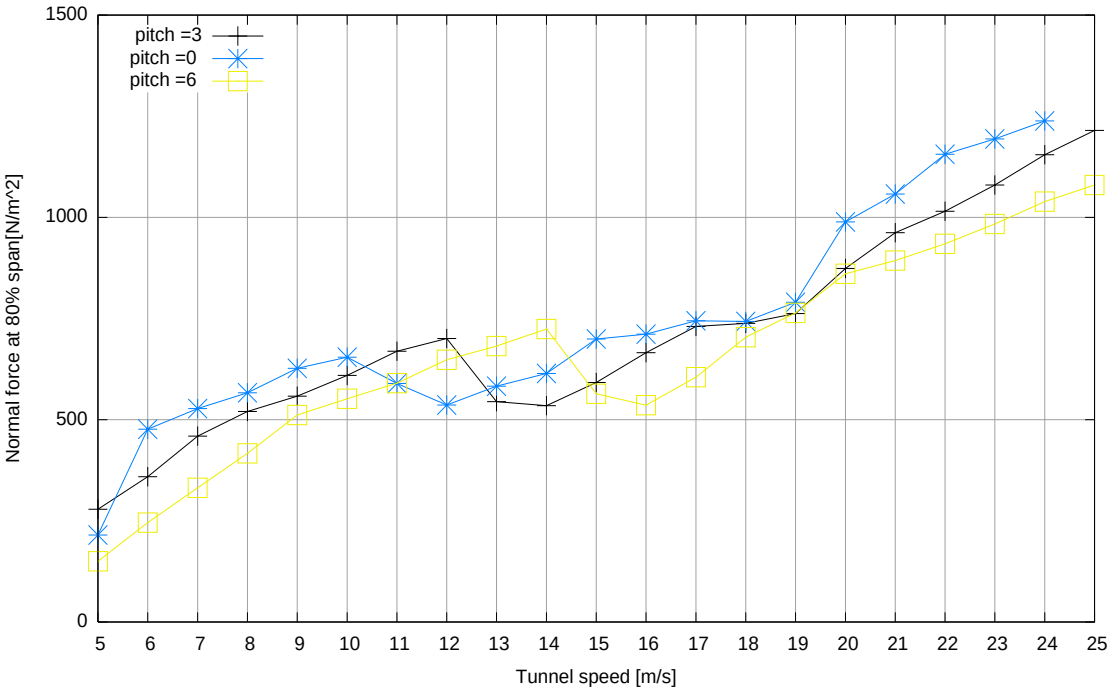

Figure 12: Measured normal force as function of tunnel speed for 80% span

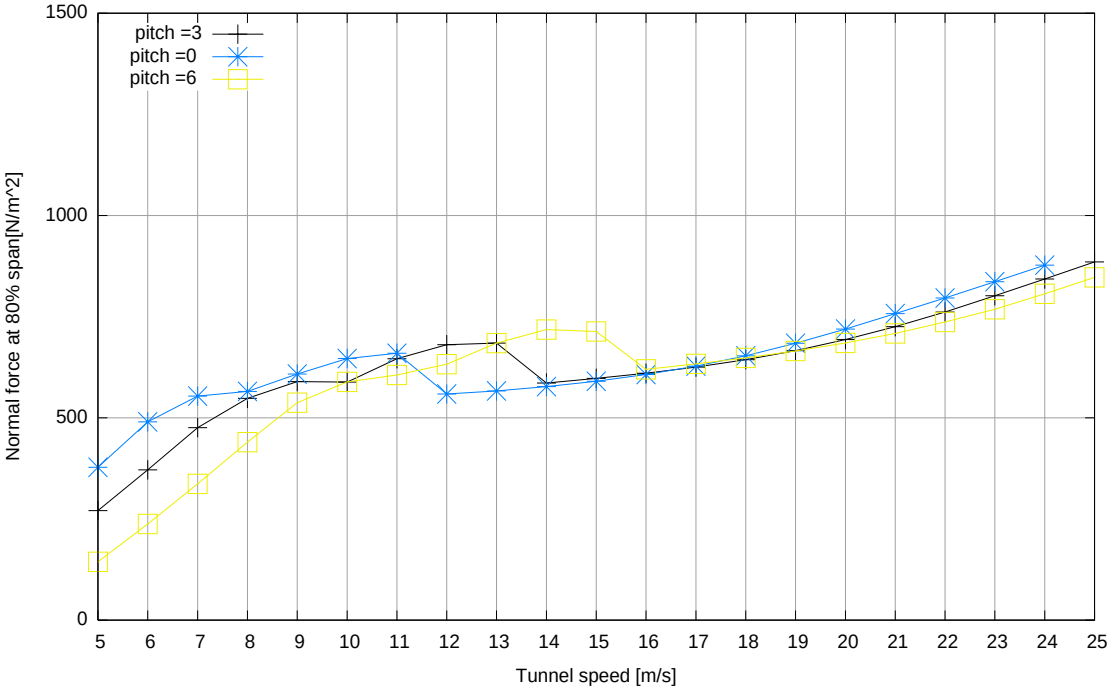

Figure 13: Calculated normal force as function of tunnel speed for 80% span

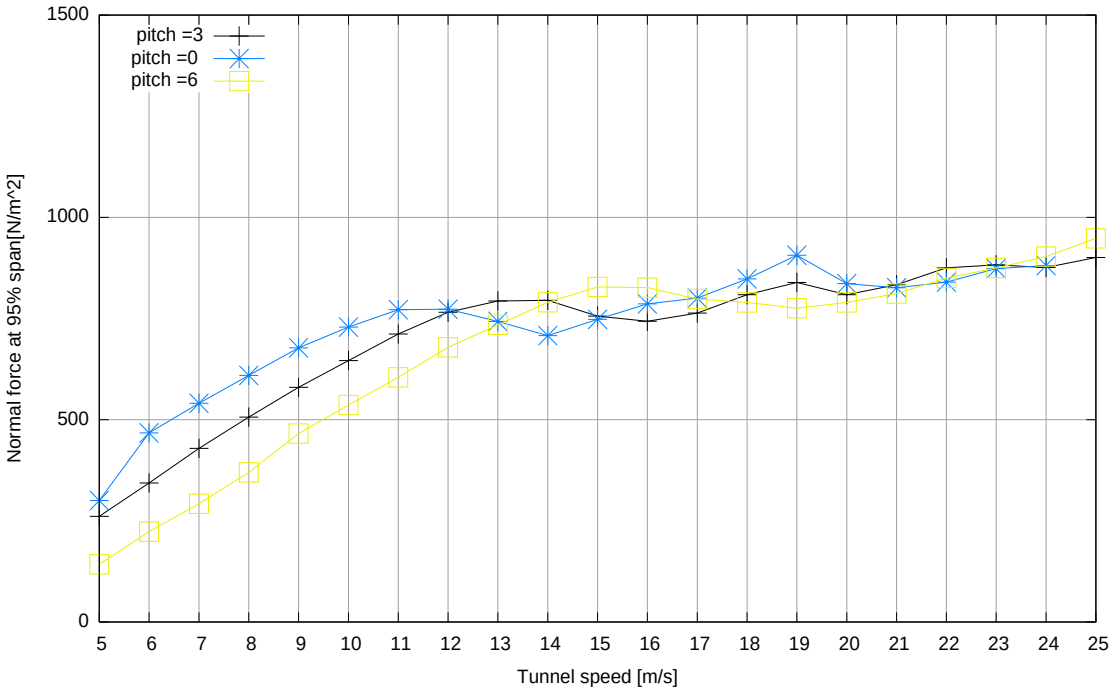

Figure 14: Measured normal force as function of tunnel speed for 95% span

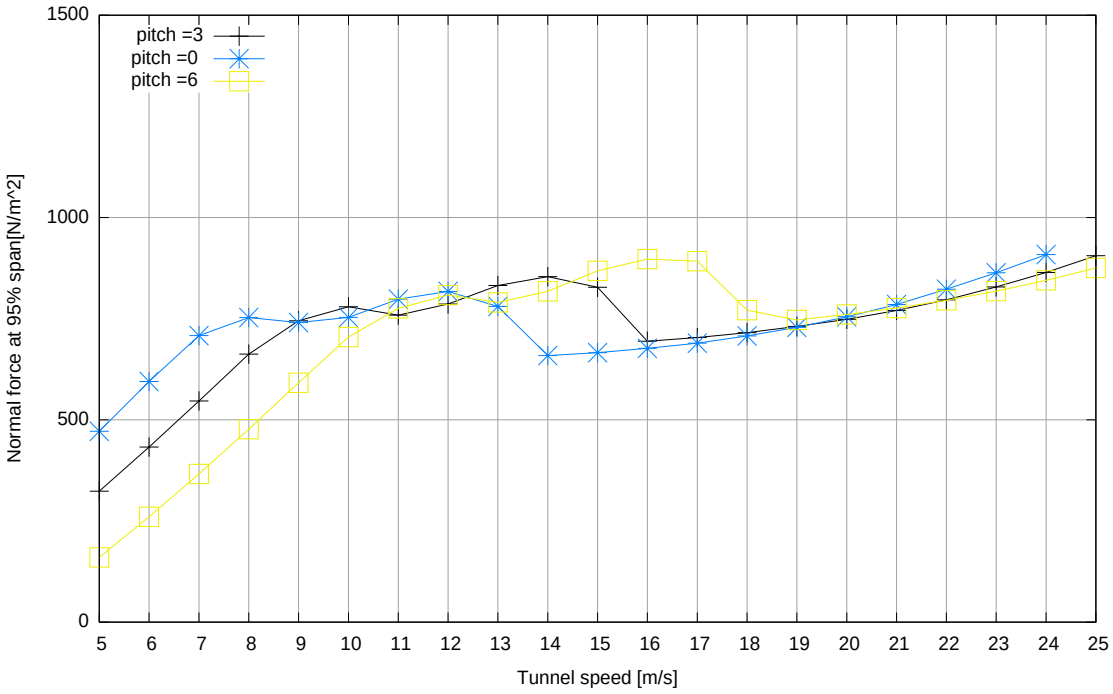

Figure 15: Calculated normal force as function of tunnel speed for 95% span

4.1.2 Ratios between measured and (PHATAS) calculated normal forces as function of tunnel speed and pitch angle

In Figures 16 through 20, the ratios between the calculated and measured normal forces are given as function of tunnel speed (e.g figure 16 shows the data from Figure 7 divided by the data from Figure 6).

As a first observation, the shape of the curves seems very similar for the different pitch angles but they are shifted in tunnel speed. This is obvious since a higher tunnel speed is needed to compensate the smaller angle of attack from the larger pitch angle. It would therefore be more convenient to discuss and present the ratios as function of the angle of attack even though it is recognized that then the aforementioned uncertainty in the definition of the angle of attack comes into play (section 4). Nevertheless it is felt that a comparison based on the PHATAS (BEM) angle of attack may yield additional and useful insights, in particular if the results are used to assess empirical corrections for BEM methods, i.e. the 3D correction from section 3.1.

The ratios between calculated and measured normal forces as function of angle of attack are given in Figures 21 through 25. The following observations can be made:

- The presentation of results as function of angle of attack often eliminates the dependency on the pitch angles, but some slight differences remain at the higher angles of attack where the strongest underprediction is often found at the smallest pitch angle of 0 degrees. This can be considered as an indication that the 3D correction, see section 3.1 should be made pitch angle dependent. This is already recognised in [10] and [8] where pitch angle dependent 3D corrections have been developed, which, consistently to the present observations, give a stronger increase in c_l at lower pitch angle.

- At 30% span and $\alpha < 15$ degrees (approximately), the differences between calculated and measured normal forces are generally $< 10\%$. At the higher angles of attack there is a considerable underprediction (in the order of 50%), which is consistent with the observations from section 4.1.1 on the very high measured values of the normal force at high tunnel speeds. Since the normal force is highly dominated by the lift force, the underprediction indicates a too low 3D correction on the c_l from the equations 1 and 2 at the high angles of attack.

- At 47% span the observations are more or less similar to the observations at 30% span, but the underprediction is less severe and in the order of 25%. This again indicates a too low 3D correction. It is interesting to note that after the continous deterioration of the results between approximately α = 5 degrees and α = 20 degrees, the agreement improves again between α = 20 degrees and α = 25 degrees. This improvement can be related to the 'dip' in measured normal forces at $V_{tun} \approx 13$ m/s (see Figure 8) which brings the measured result 'down' and closer to the calculated curve. The calculated curve shows a similar dip, but to a smaller extent and at a lower tunnel speed. This might indicate a 'longer stall delay' than assumed in the PHATAS model from section 3.1.

- The observations at 63% span are very similar to the observations at 47% span. For $\alpha < 15$ degrees (approximately), the normal forces are again predicted well but for higher angles of attack the normal force is underpredicted with $\approx 25\%$. For $\alpha > 25$ degrees (approximately), an improvement in agreement is visible.

- At 80% span the measured normal forces are predicted well until say α = 20 degrees. For higher angles of attack, the normal force is underpredicted with 25%.

- At 95% span the normal force is overpredicted until say α = 10 degrees. The overprediction is in the order of 25%. At the much higher angles of attack (say $\alpha > 15$ degrees) there is (again) a slight underprediction of the normal forces.

Altogether the results indicate that the present PHATAS calculations suffer from a too low 3D stall correction. This conclusion should be considered with care, since it depends heavily on the basic 2D airfoil characteristics, which are input for the PHATAS code (See section 3.1). However, the conclusion is confirmed by results from the Annexlyse project (see [6]), where similar observations were made on field measurements which are taken on different turbines.

The final observation, i.e. the overprediction of the normal force at 95%, is also consistent with observations from the Annexlyse project where an overpredicted normal force at the tip of other

wind turbines is found. This overprediction is explained by the fact that the Prandtl tip factor (as implemented in PHATAS) only corrects the non-uniformity of the flow from the finite number of blades. Apart from these tip effects, the two dimensional airfoil coefficients that are used in PHATAS are incorrect in the region of some chord length from the tip. As an example of impact, the 2π lift gradient from 2D theory is not valid anymore. The 2π lift gradient is based on an infinite length of the bound vortex distribution, but very near the tip, this bound vortex distribution becomes closer to semi infinite (only in direction of the root) by which it yields a lower aerodynamic load. Currently ECN is developing a tip model which is based on a physical near wake description by which the finite length of the bound vortex strength is automaticallly taken into account.

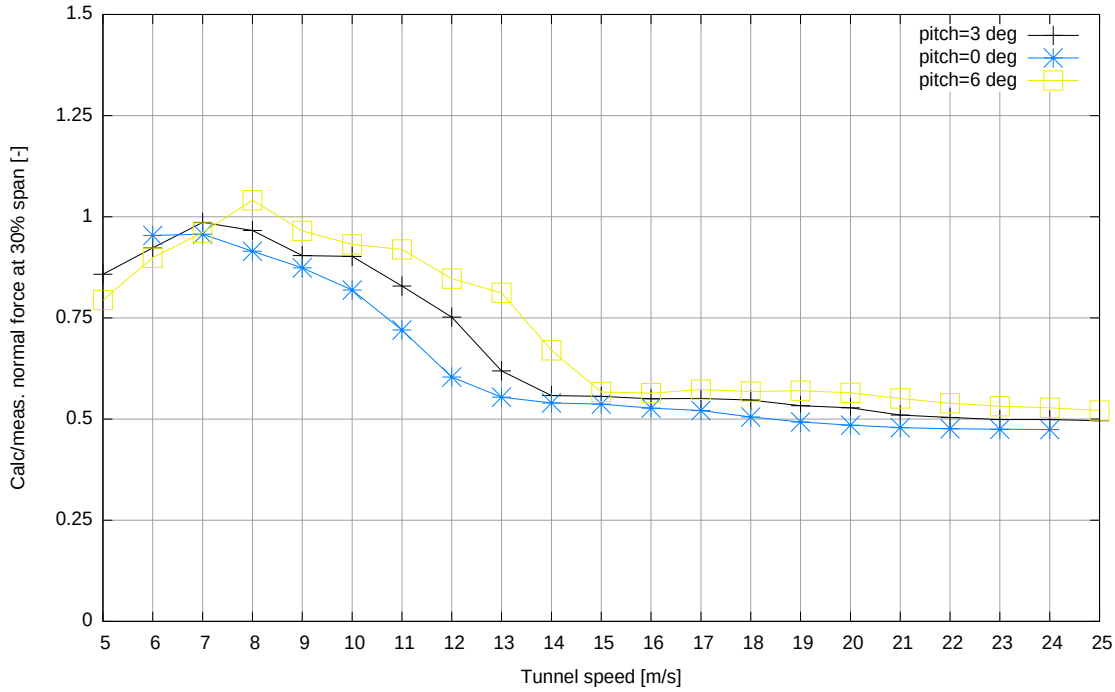

Figure 16: Ratio between calculated and measured normal force as function of tunnel speed at 30% span

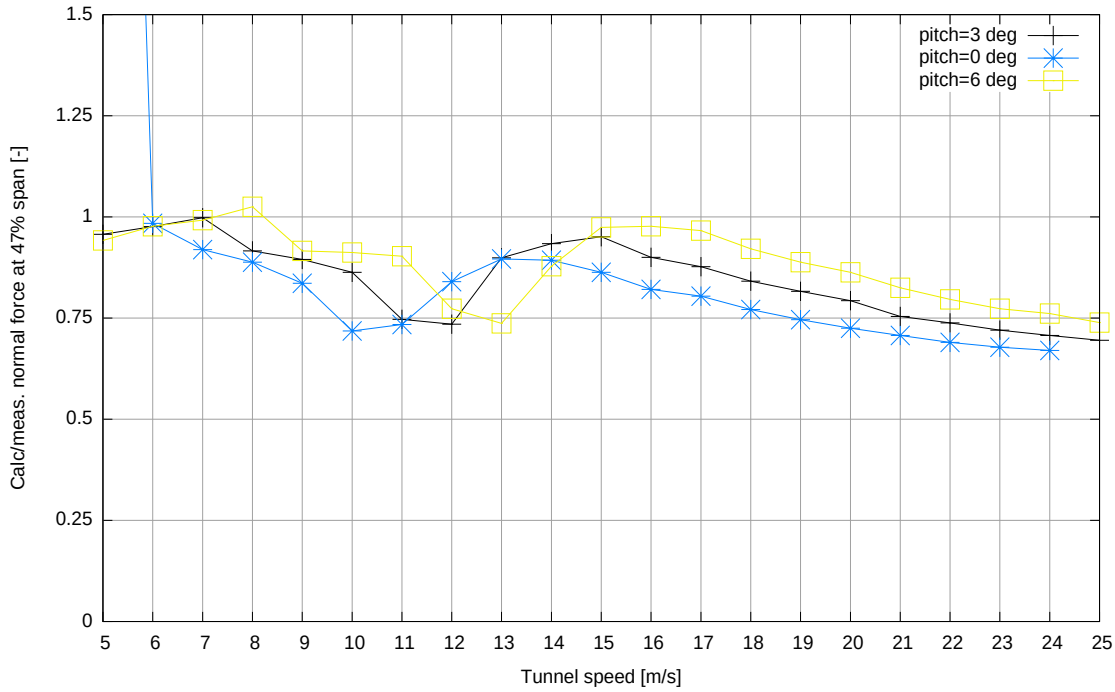

Figure 17: Ratio between calculated and measured normal force as function of tunnel speed at 47% span

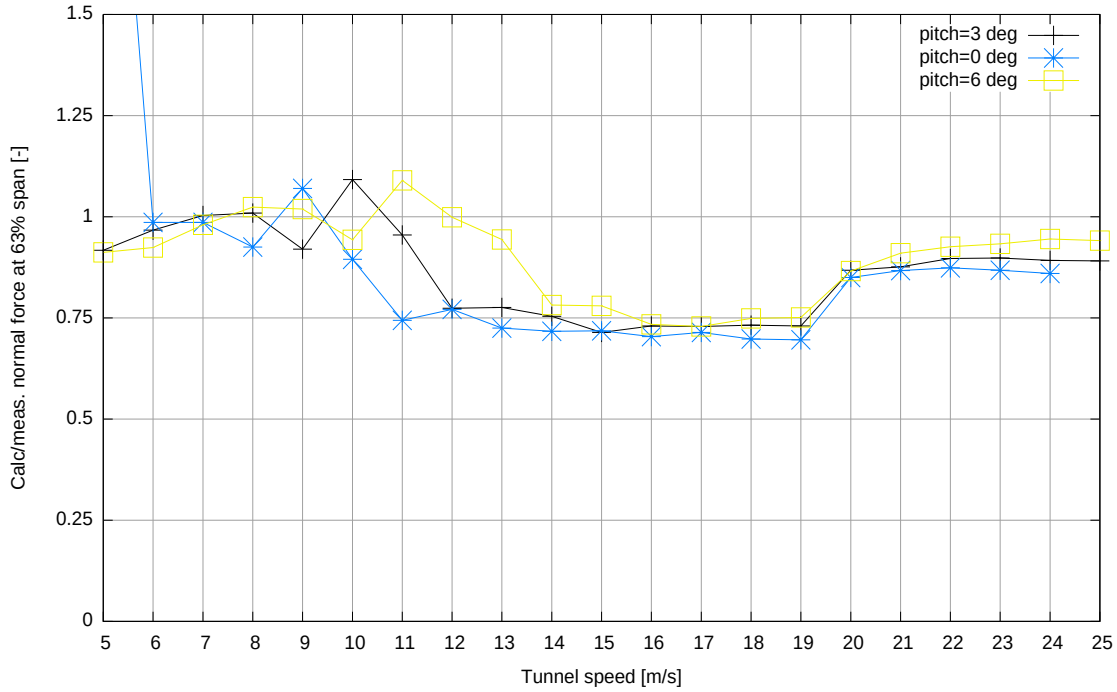

Figure 18: Ratio between calculated and measured normal force as function of tunnel speed at 63% span

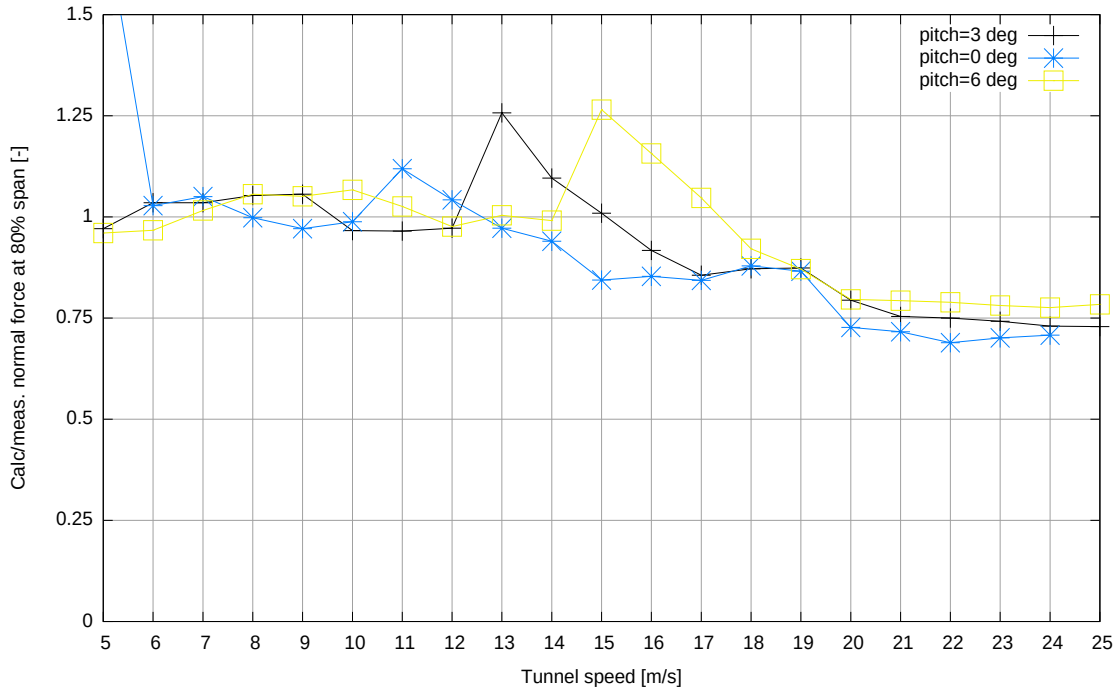

Figure 19: Ratio between calculated and measured normal force as function of tunnel speed at 80% span

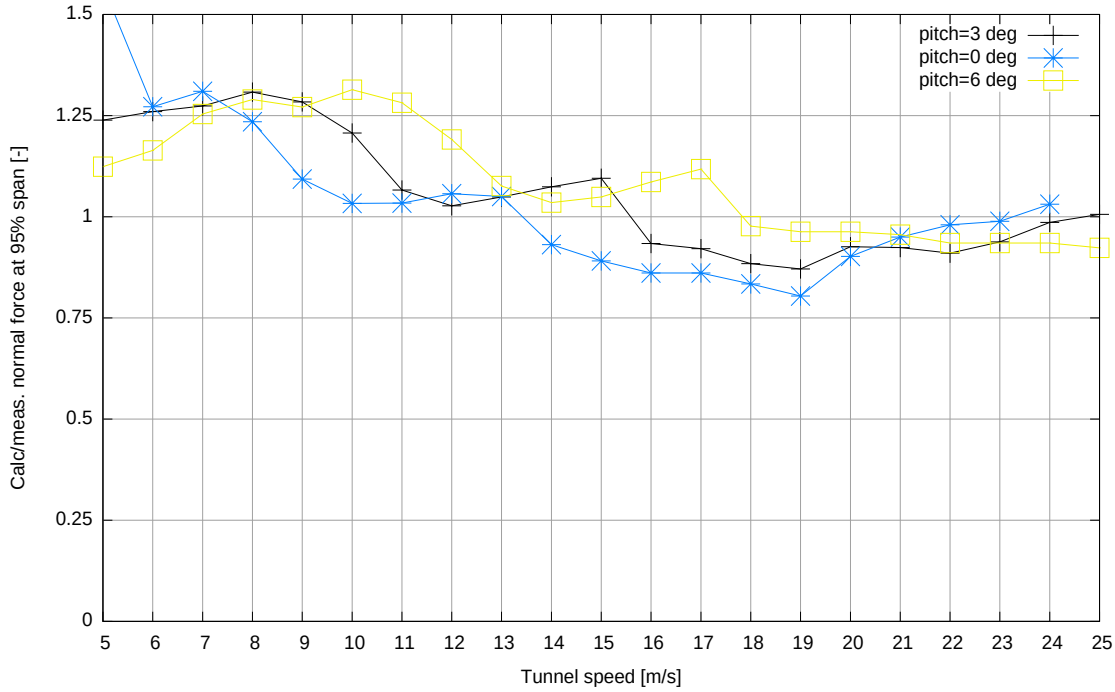

Figure 20: Ratio between calculated and measured normal force as function of tunnel speed at 95% span

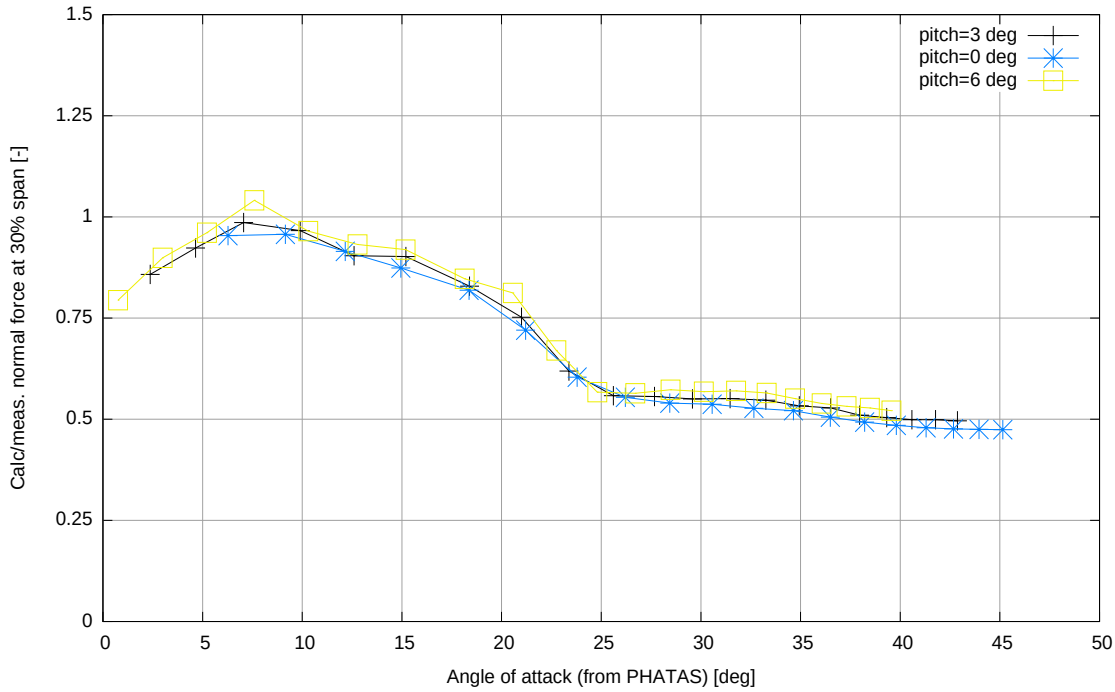

Figure 21: Ratio between calculated and measured normal force as function of angle of attack at 30% span

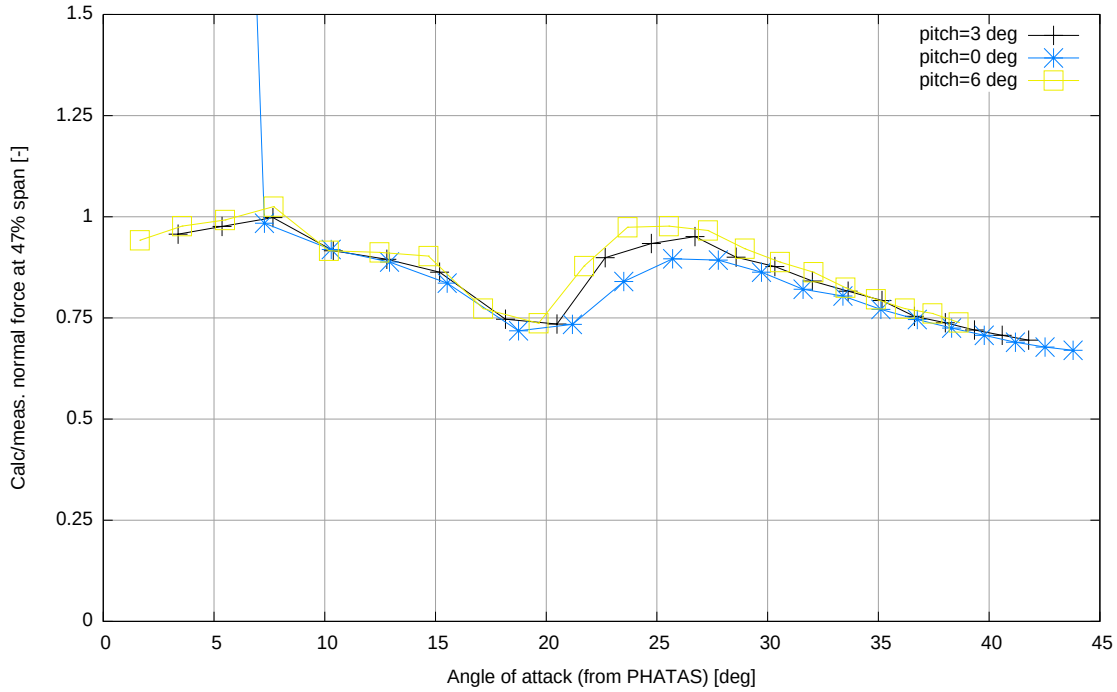

Figure 22: Ratio between calculated and measured normal force as function of angle of attack at 47% span

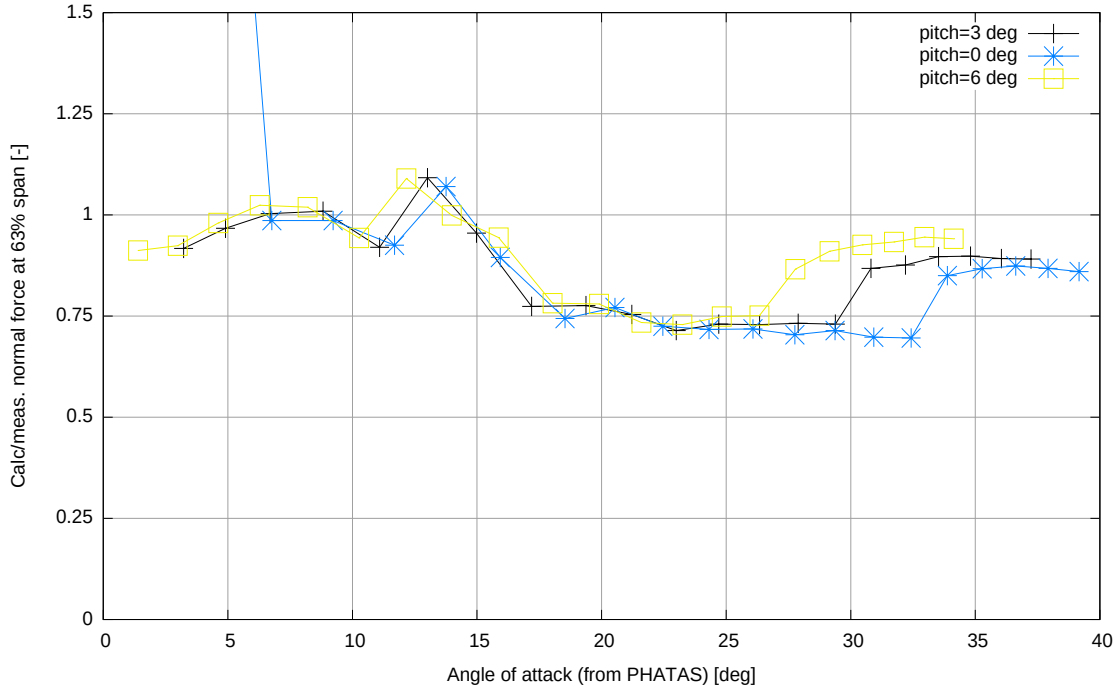

Figure 23: Ratio between calculated and measured normal force as function of angle of attack at 63% span

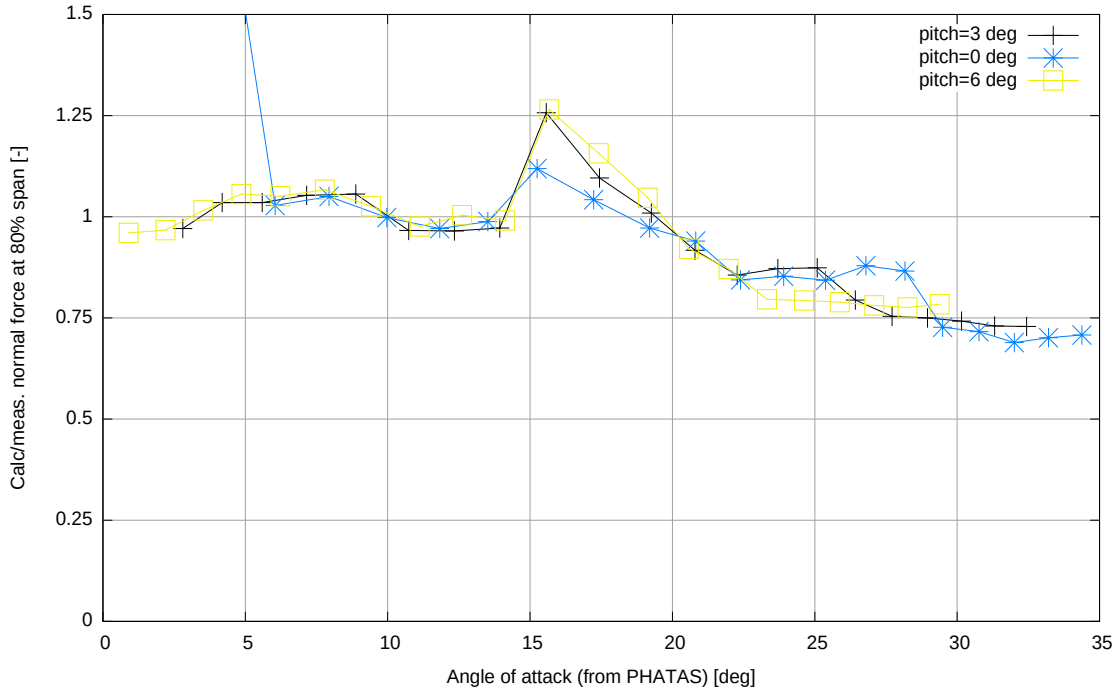

Figure 24: Ratio between calculated and measured normal force as function of tunnel speed at 80% span

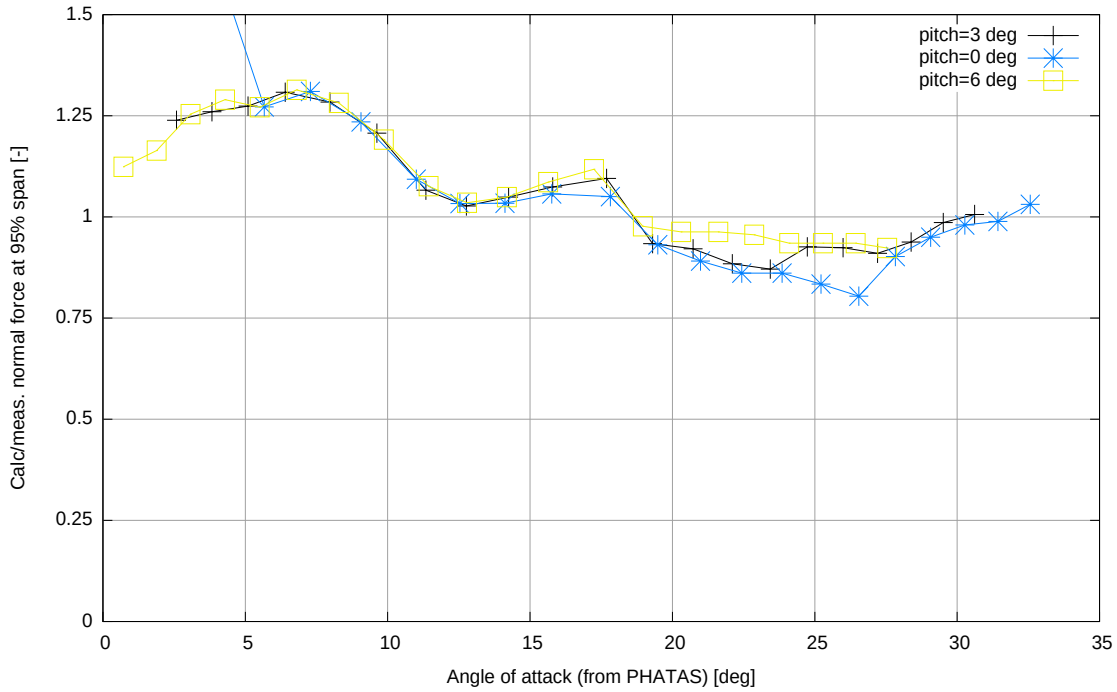

Figure 25: Ratio between calculated and measured normal force as function of tunnel speed at 95% span

4.1.3 Measured and (PHATAS/AWSM) calculated normal forces and angles of attack as function of radial position

In the figures 26 to 43 a comparison is made between the measured normal forces and the normal forces calculated with PHATAS and AWSM for three tunnel speeds: 5, 7 and 9 m/s and three pitch angles: 3, 0 and 6 degrees (i.e. the sequences H, I, J respectively). The results are plotted as function of radial position. In addition the corresponding angles of attack are plotted (no measured angles of attack are available).

It can be concluded that the normal forces calculated with AWSM are usually very close to the normal forces calculated with PHATAS, where the agreement between the PHATAS results and the measurements at these wind speeds is already known to be very good (see section 4.1.2). Generally speaking the angles of attack at 47%, 63% and 80% calculated with AWSM are (very slightly) higher than the angles of attack calculated with PHATAS. An important improvement from the AWSM code is visible at the 95% station. At this station the PHATAS calculated normal force is considerably overestimated, where AWSM overpredicts the normal force to a smaller extent. This is consistant with the smaller angle of attack as predicted by AWSM at this station (Note that for V_{tun} = 9 m/s and θ = 0 degrees, i.e. the figures 36 and 37, the stall angle of attack is exceeded by which an increase in angle of attack corresponds to a decrease in lift). As explained in section 4.1.2, PHATAS applies the so-called Prandtl tip correction. This correction is based on an analysis from a simplified vortex wake model, where the AWSM code models the flow around the tip in a more realistic sense, probably leading to a more realistic angle of attack. However, it does not fully prevent the overprediction of the normal force which can be explained by the fact that AWSM, similar to PHATAS uses the two dimensional (non-rotating) airfoil characteristics, which is incorrect near the very tip, see section 4.1.2.

A similar observation can be made on the angle of attack at the 30% section: Generally speaking, the angle of attack, as calculated by AWSM is lower than the angle of attack from PHATAS, possibly due to root effects. These differences are not reflected into the normal force which may partly be a result of the fact that the angle of attack is close to the stalled angle of attack (where $dc_n/d\alpha$ is small) .

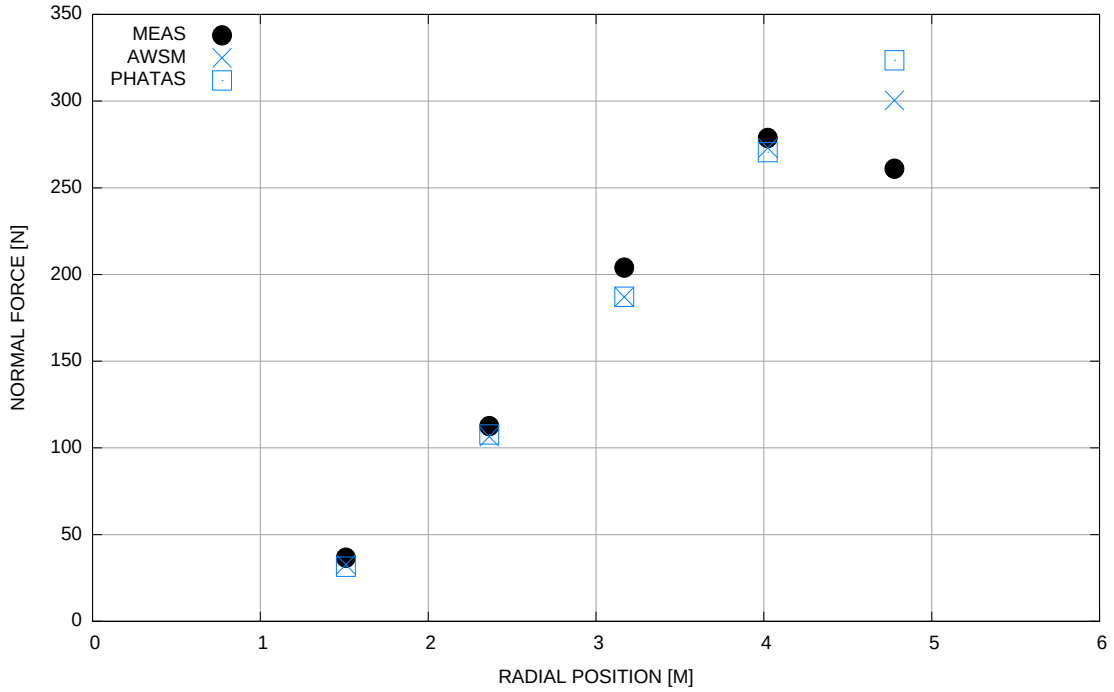

Figure 26: Comparison between calculated and measured normal force as function of radial position at V_{tun} = 5 m/s and θ =3 degrees

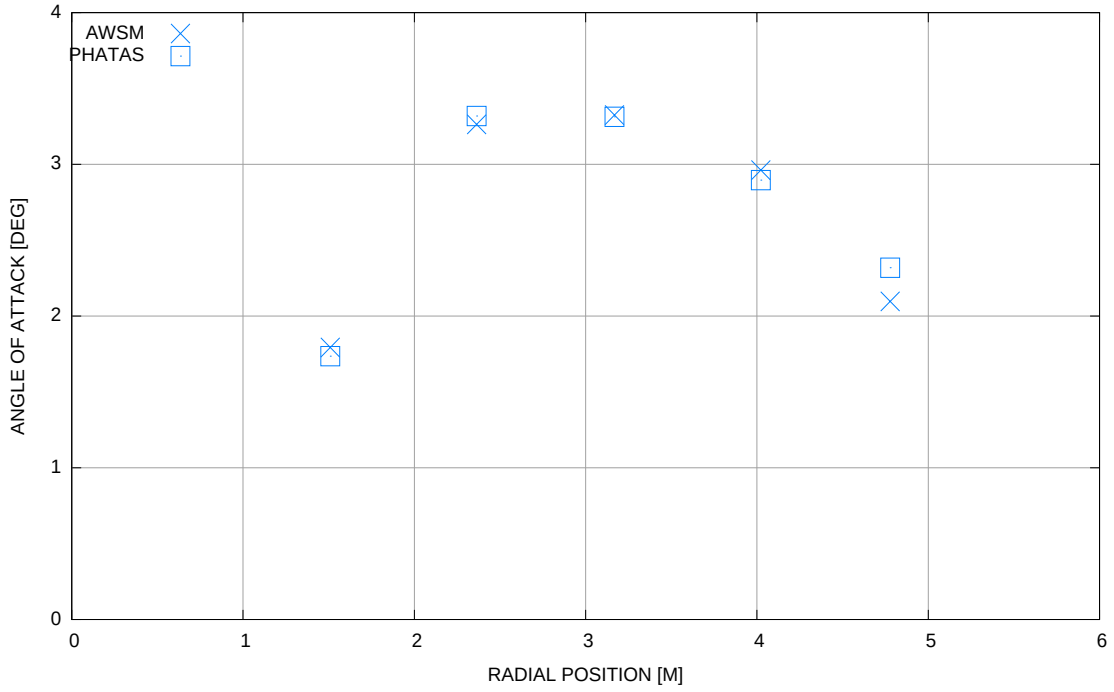

Figure 27: Comparison between PHATAS and AWSM calculated angle of attack as function of radial position at V_{tun} = 5 m/s and θ =3 degrees

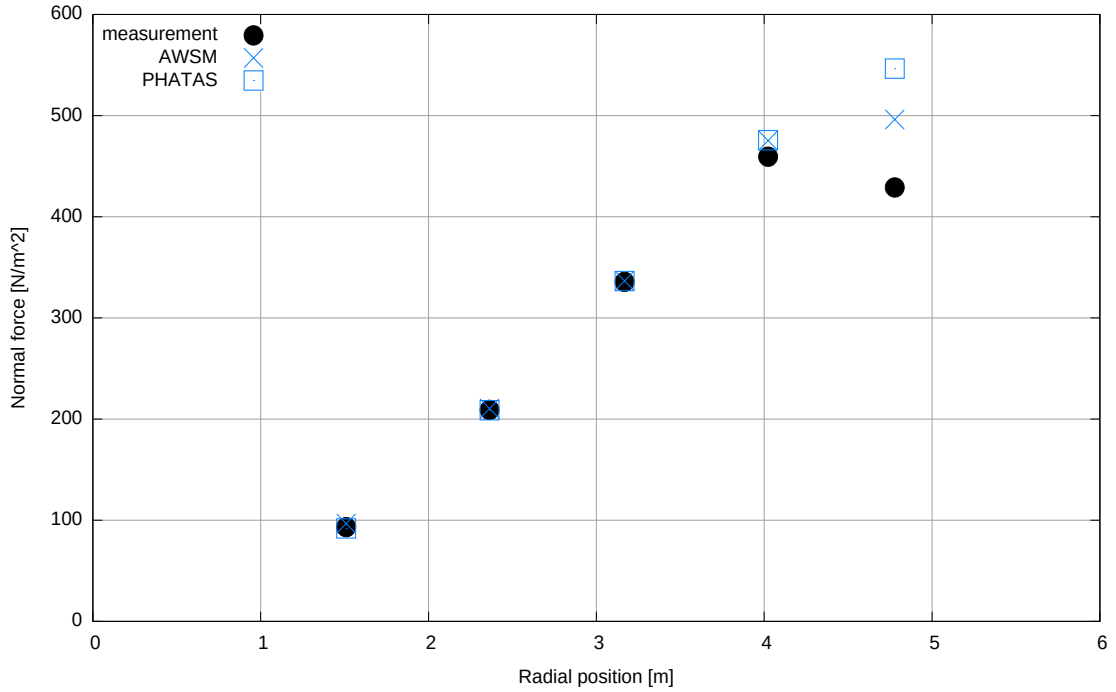

Figure 28: Comparison between calculated and measured normal force as function of radial position at V_{tun} = 7 m/s and θ =3 degrees

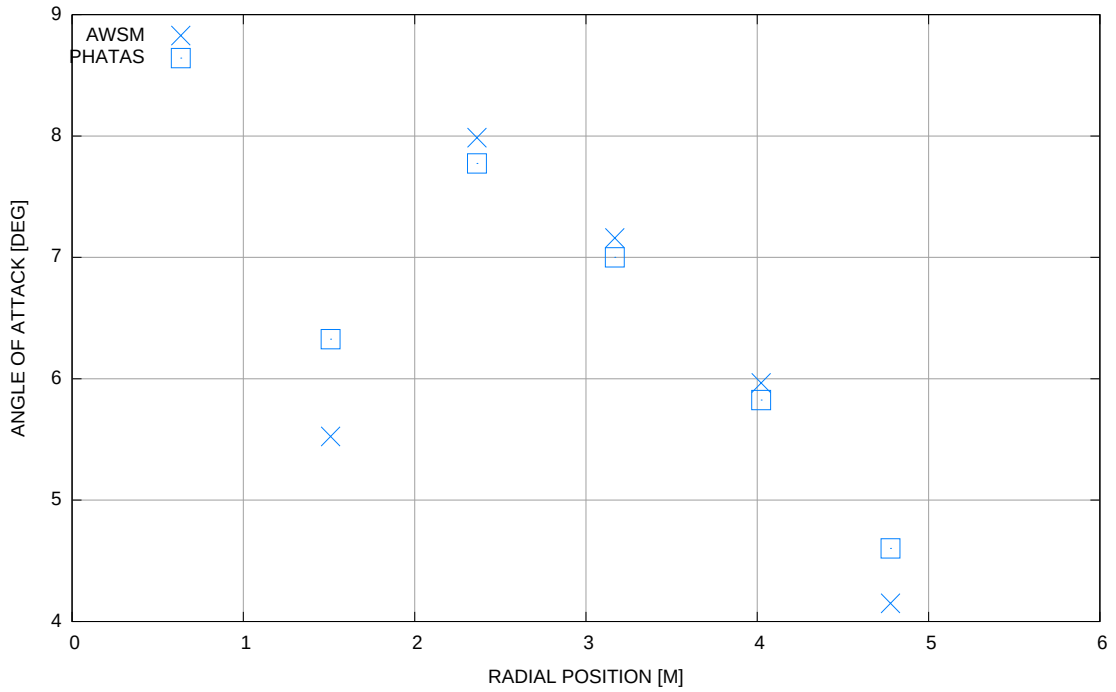

Figure 29: Comparison between PHATAS and AWSM calculated angle of attack as function of radial position at V_{tun} = 7 m/s and θ =3 degrees

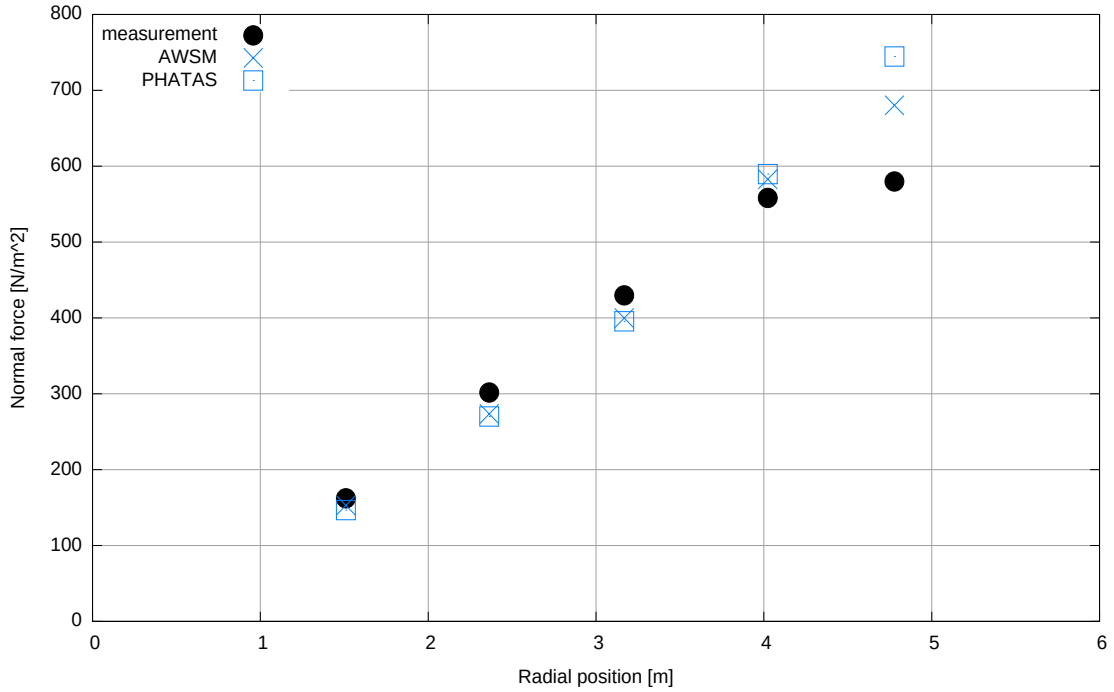

Figure 30: Comparison between calculated and measured normal force as function of radial position at V_{tun} = 9 m/s and θ = 3 degrees

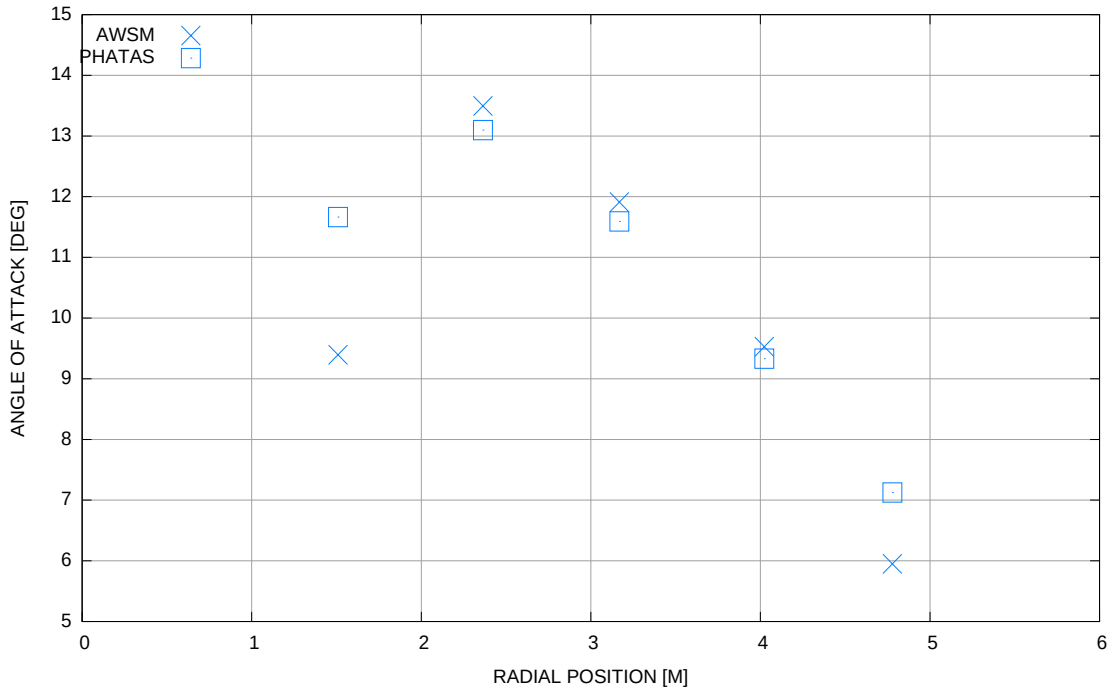

Figure 31: Comparison between PHATAS and AWSM calculated angle of attack as function of radial position at V_{tun} = 9 m/s and θ =3 degrees

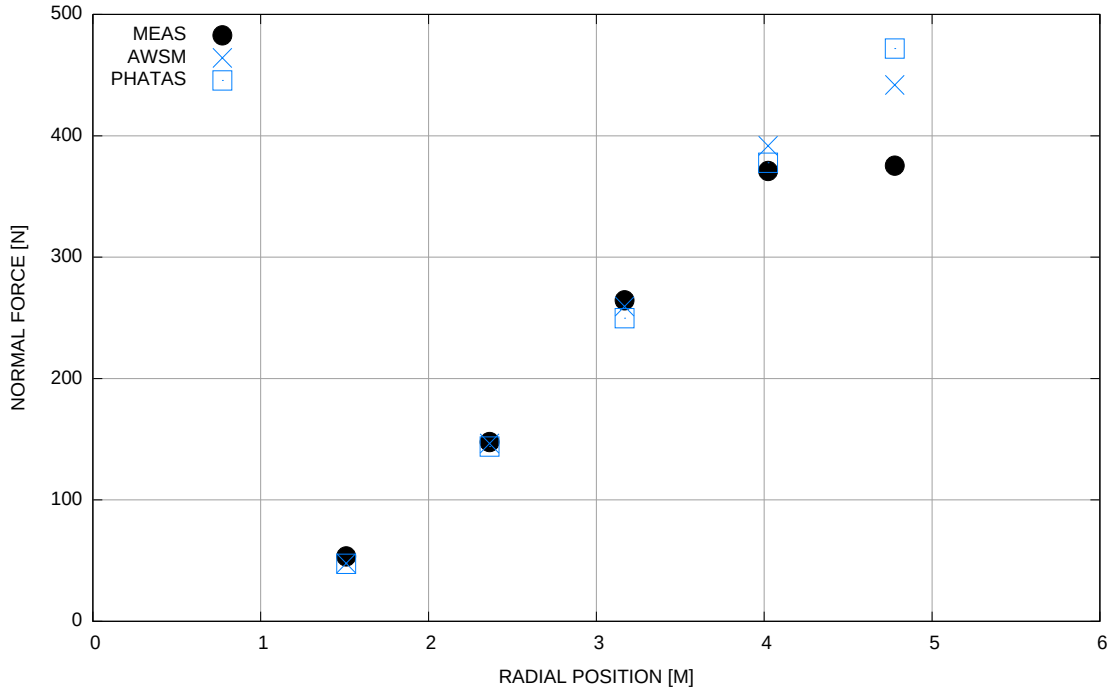

Figure 32: Comparison between calculated and measured normal force as function of radial position at V_{tun} = 5 m/s and θ =0 degrees

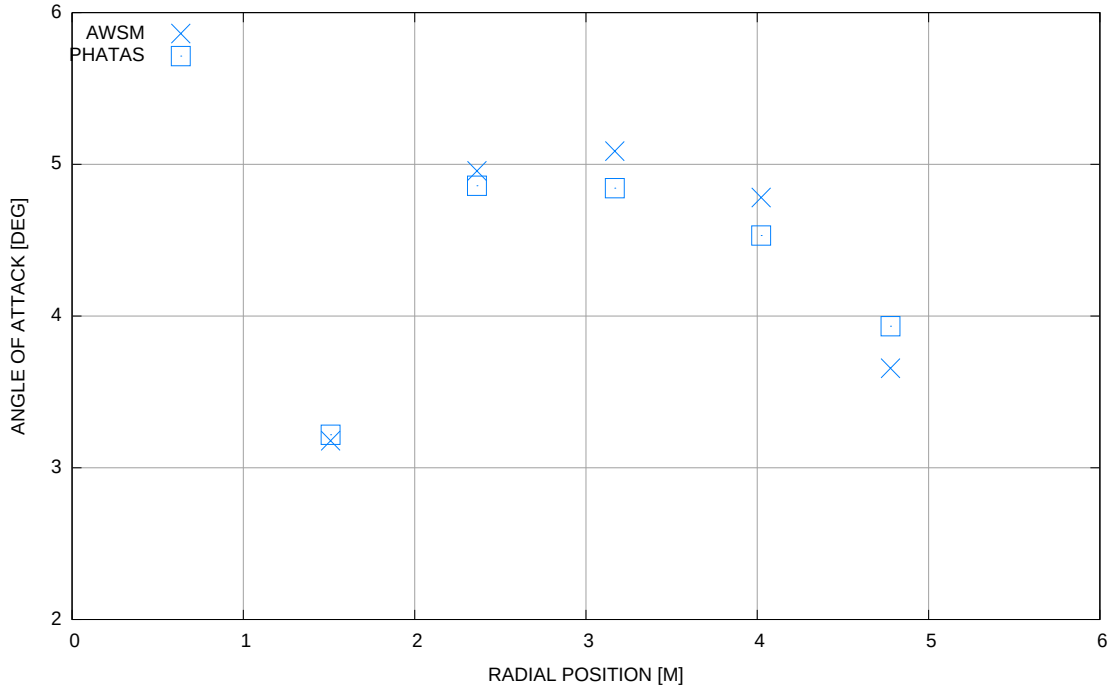

Figure 33: Comparison between PHATAS and AWSM calculated angle of attack as function of radial position at V_{tun} = 5 m/s and θ =0 degrees

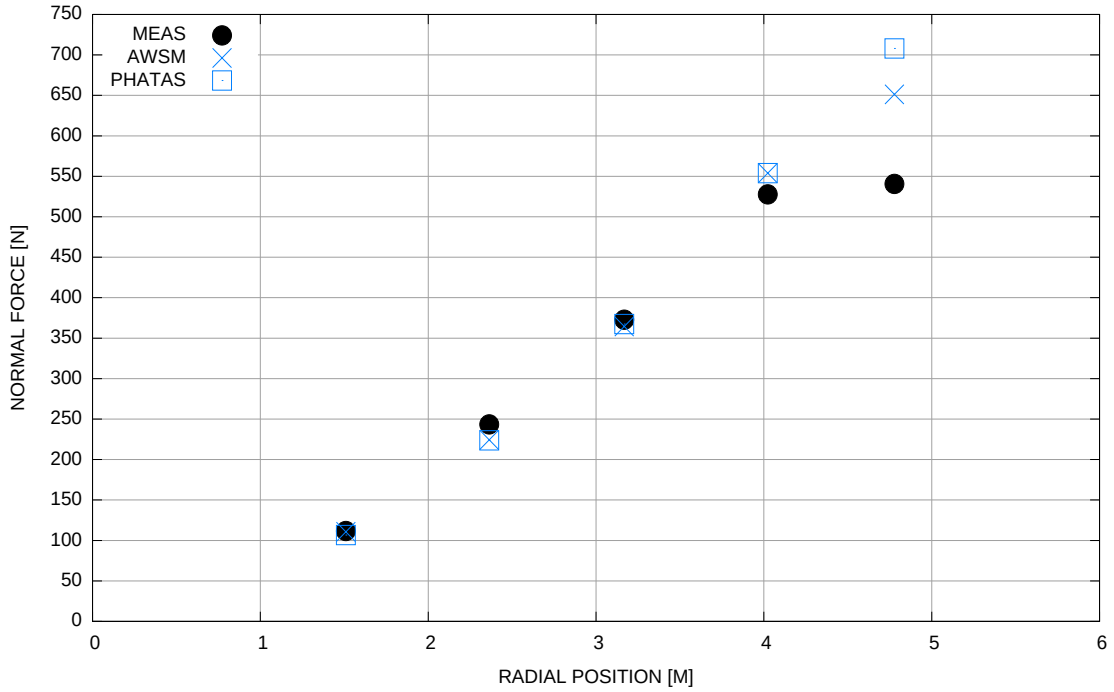

Figure 34: Comparison between calculated and measured normal force as function of radial position at V_{tun} = 7 m/s and θ =0 degrees

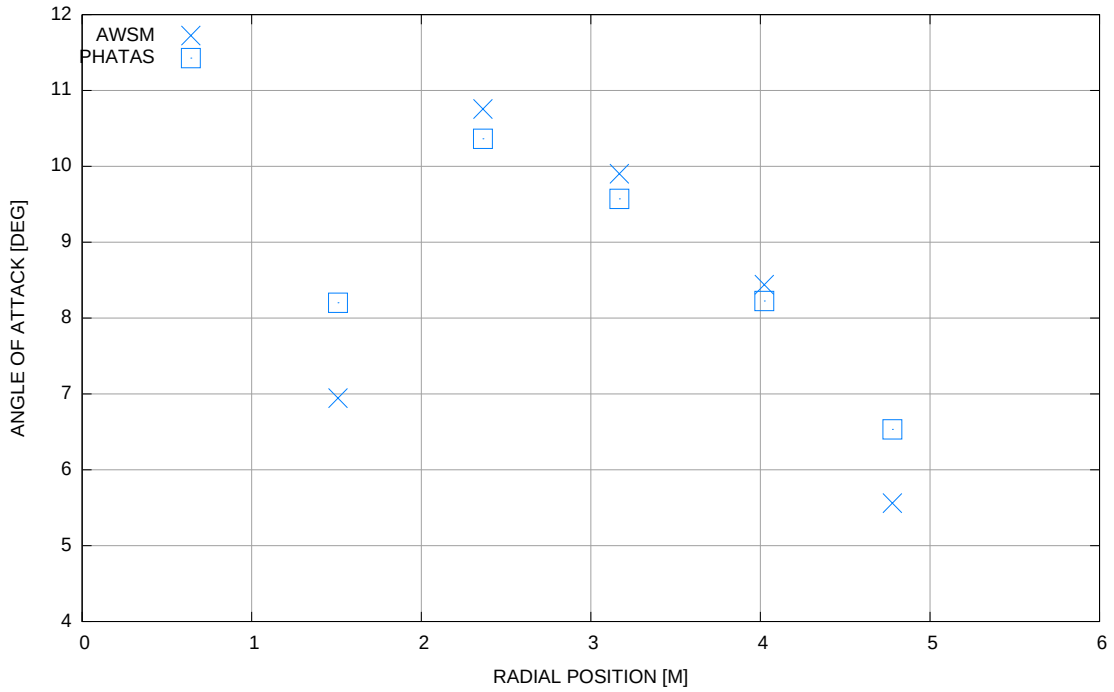

Figure 35: Comparison between PHATAS and AWSM calculated angle of attack as function of radial position at V_{tun} = 7 m/s and θ =0 degrees

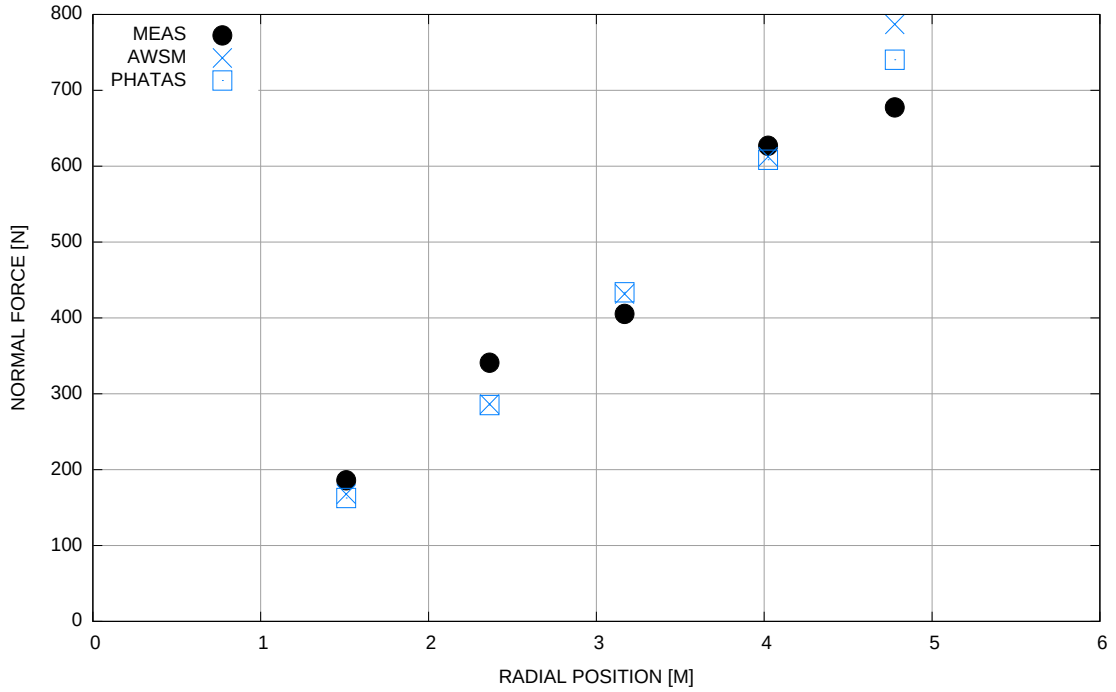

Figure 36: Comparison between calculated and measured normal force as function of radial position at V_{tun} = 9 m/s and θ = 0 degrees

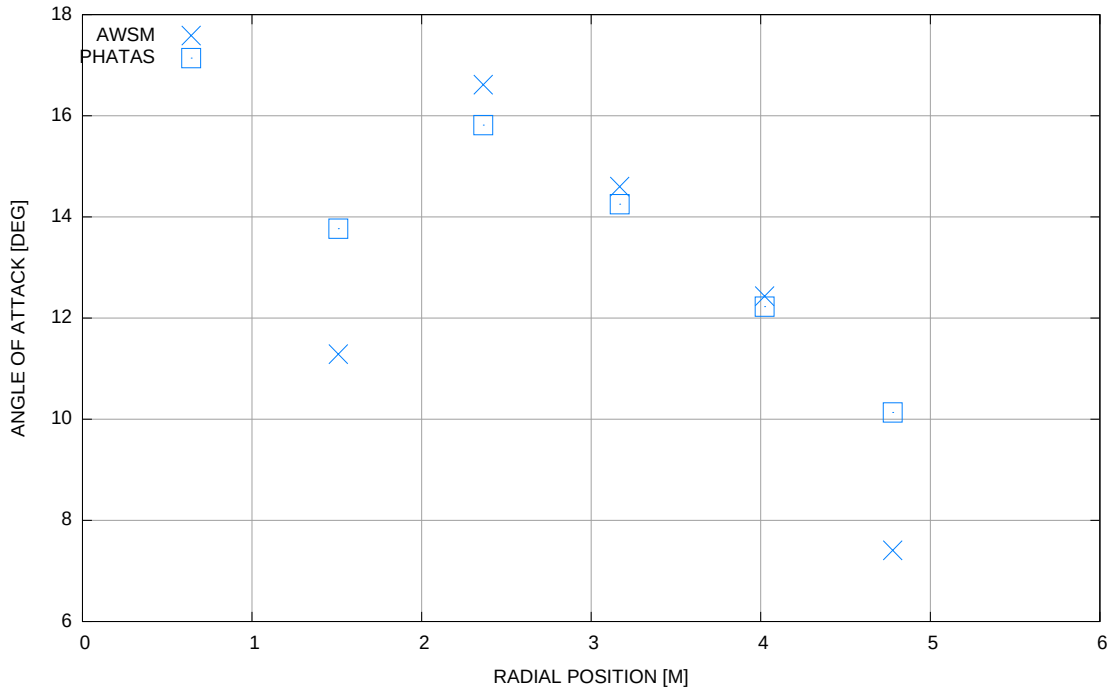

Figure 37: Comparison between PHATAS and AWSM calculated angle of attack as function of radial position at V_{tun} = 9 m/s and θ =0 degrees

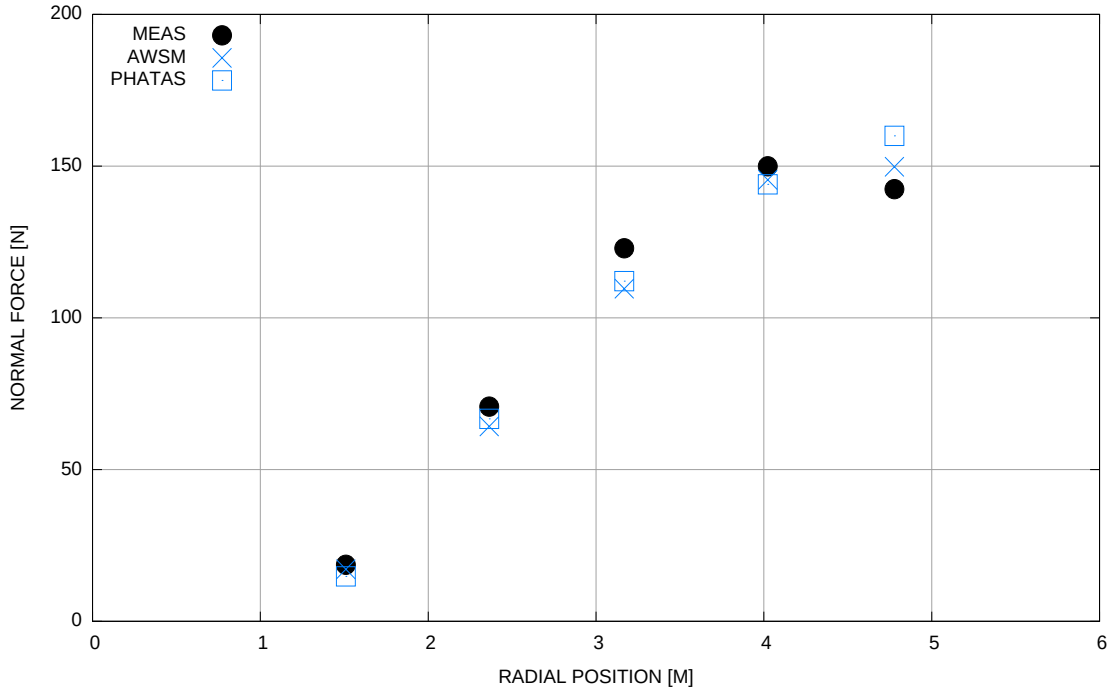

Figure 38: Comparison between calculated and measured normal force as function of radial position at V_{tun} = 5 m/s and θ =6 degrees

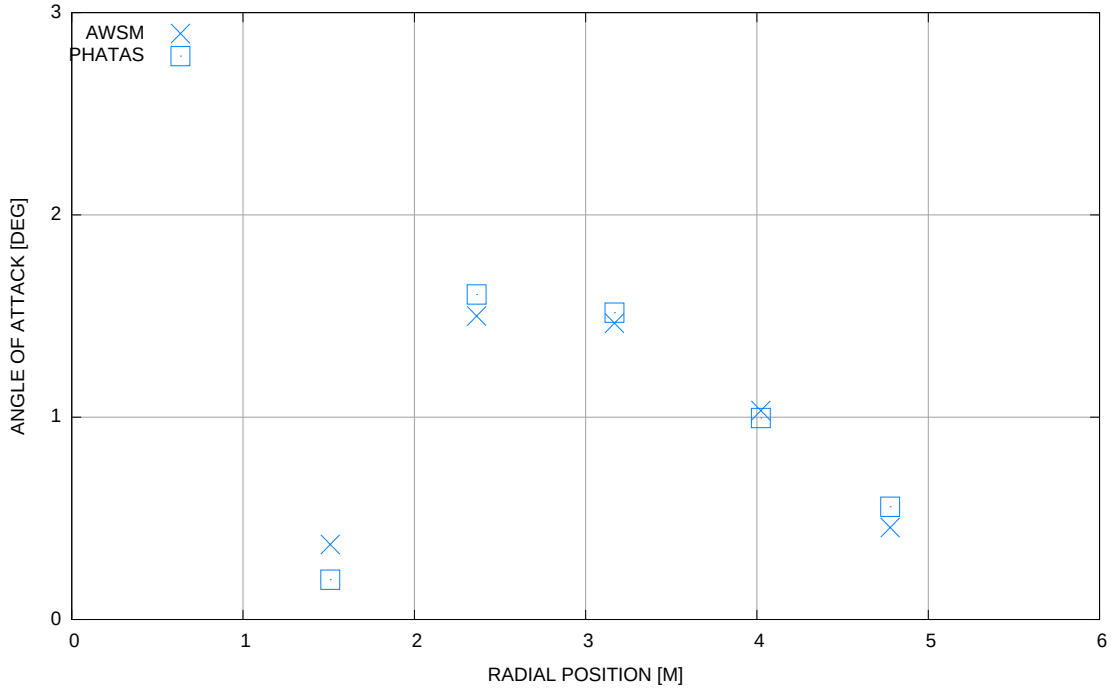

Figure 39: Comparison between PHATAS and AWSM calculated angle of attack as function of radial position at V_{tun} = 5 m/s and θ =6 degrees

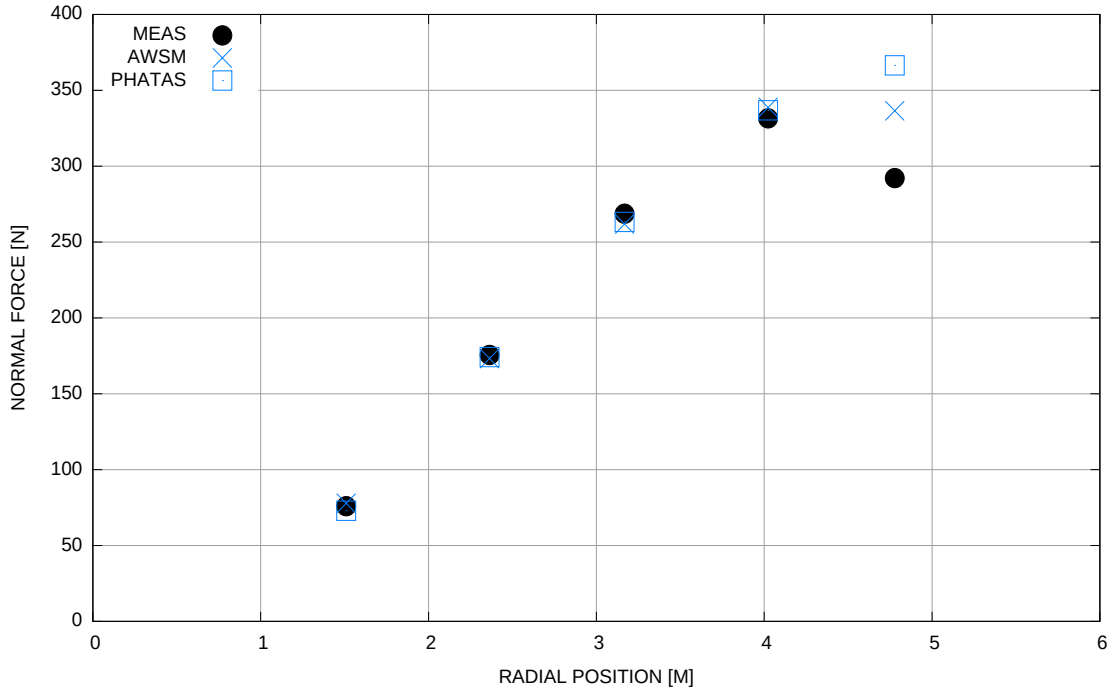

Figure 40: Comparison between calculated and measured normal force as function of radial position at V_{tun} = 7 m/s and θ =6 degrees

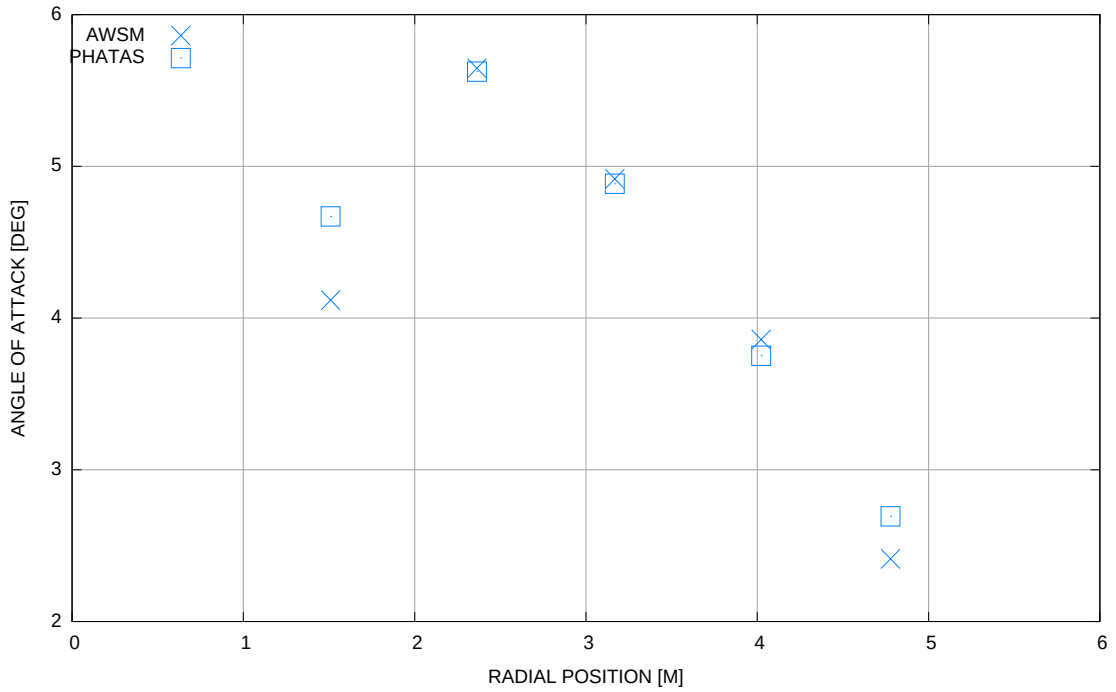

Figure 41: Comparison between PHATAS and AWSM calculated angle of attack as function of radial position at V_{tun} = 7 m/s and θ =6 degrees

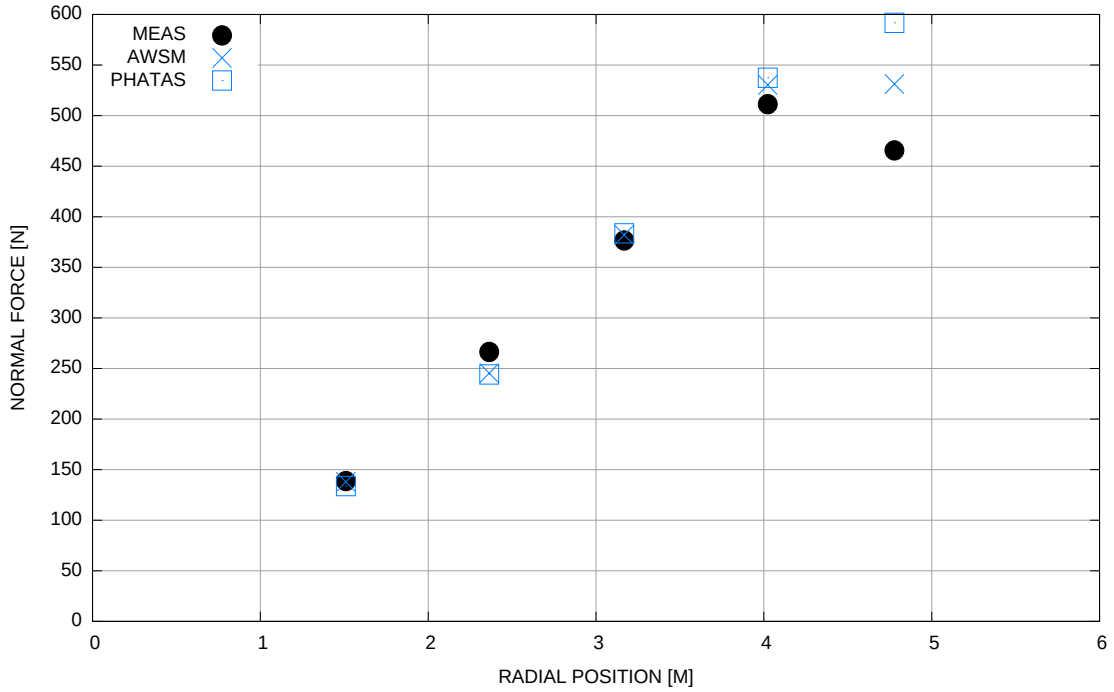

Figure 42: Comparison between calculated and measured normal force as function of radial position at V_{tun} = 9 m/s and θ = 0 degrees

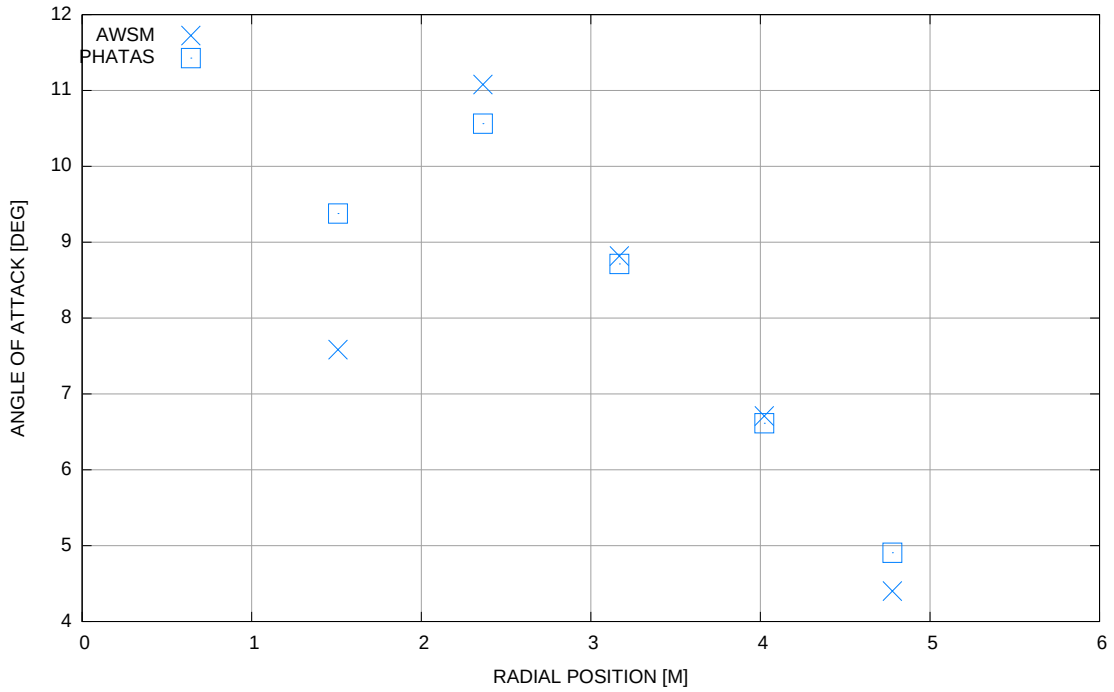

Figure 43: Comparison between PHATAS and AWSM calculated angle of attack as function of radial position at V_{tun} = 9 m/s and θ =6 degrees

4.1.4 Measured and (PHATAS) calculated normal force as function of azimuth angle

In Figures 44 and 45 the azimuthally binned averaged normal forces at 30% span, 47% span and 80% span are presented for V_{tun} = 5 and 25 m/s. The azimuth angle is defined in such a way that it is 0 degrees at the '12 o clock position' and positive for clockwise rotation (As a matter of fact the actual rotor rotates anti-clockwise, but in view of the non-yawed tunnel conditions, the flow is symmetrical along the vertical line through the rotor centre, which allows the assumption of a clock-wise rotation).

The differences in time averaged normal forces which were discussed in the sections 4.1.1 and 4.1.2 are now reflected into an off-set of the level of the azimuthally binned normal force. At a tunnel speed of 5 m/s the agreement between calculated and measured normal forces is good. The variation in normal force over the azimuth angle is limited, where the main variation comes from the tower shadow (near ϕ_r = 180 degrees). At a tunnel speed of 25 m/s the calculated variation is still limited but the measured curves at high tunnel speeds show a considerable variation over the rotor plane (possibly due to instationary aerodynamic effects and/or non-uniformity which is not taken into account in the modelling).

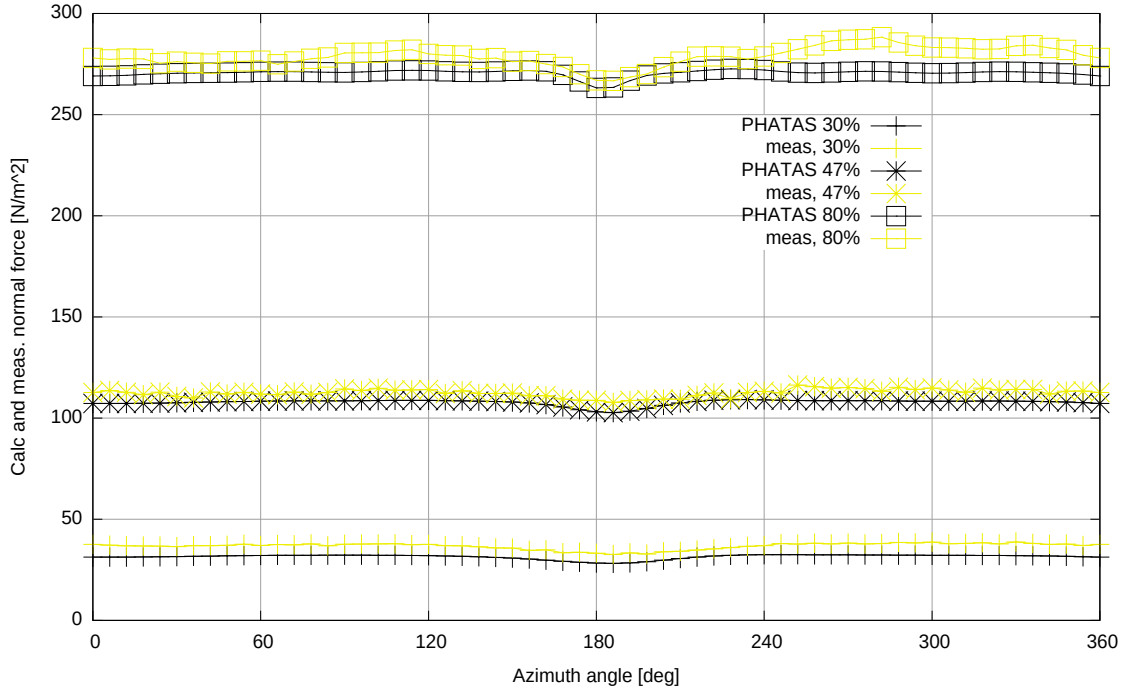

Figure 44: Azimuthally binned averaged normal forces at 30%, 47% and 80% span, at V_{tun}=5 m/s and at θ = 3 degrees: Measured and PHATAS calculated result

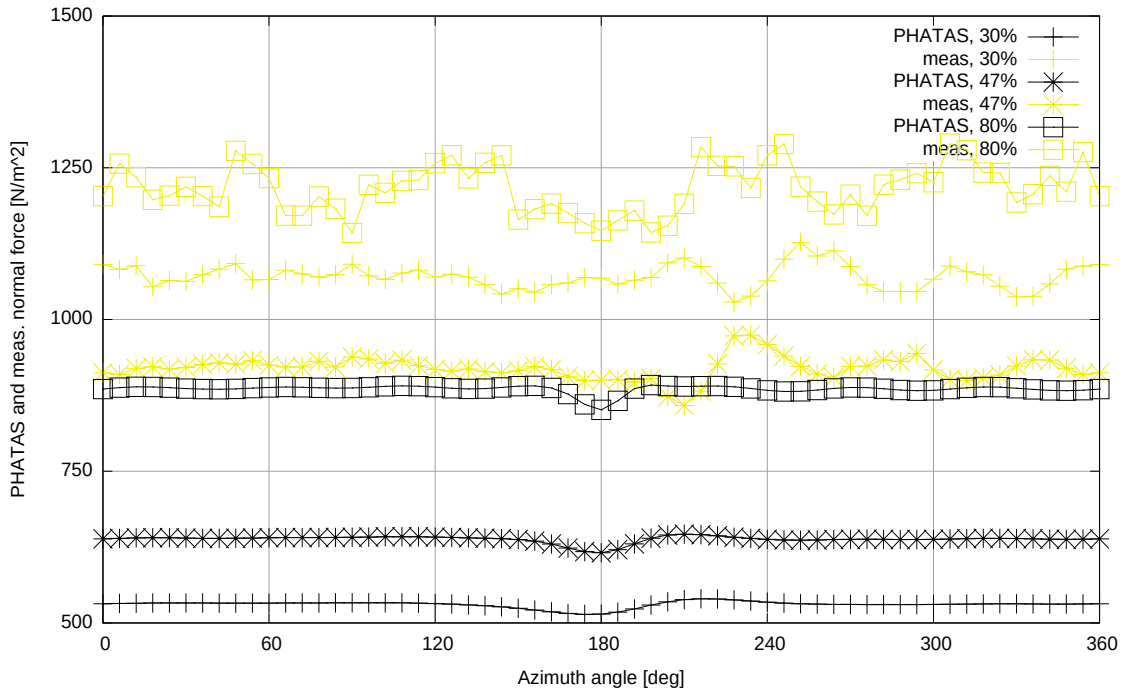

Figure 45: Azimuthally binned averaged normal forces at 30%, 47% and 80% span, at V_{tun}=25 m/s and at θ = 3 degrees: Measured and PHATAS calculated result

4.2 Tangential forces

In this section the results of the sectional tangential forces are analysed. The comparison between calculated and measured results is largely similar to the comparison which has been made on the normal forces (section 4.1). Thereto section 4.2.1 presents the mean calculated and measured tangential forces as function of tunnel speed and pitch angle, where the measured and calculated results are given in separate figures. In section 4.2.2 the ratios between the calculated and measured results are discussed.

It must be noted that the results are presented as the tangential forces divided by the chord length (i.e. $c_t \cdot 0.5\rho V^2$).

The tangential force (in both PHATAS and in the measurements) is defined such that it is positive towards the leading edge. Hence an increase in lift and a decrease in drag yields a larger (i.e. a more positive) tangential force.

4.2.1 Measured and (PHATAS) calculated tangential forces as function of tunnel speed and pitch angle

In Figures 46, 48, 50, 52, 54, the measured mean tangential forces are presented as function of tunnel speed for the 3 pitch angles considered.

In Figures 47, 49, 51, 53, 55, the corresponding results obtained with PHATAS are plotted. The discussion of these results will take place in the next section but at first sight already, some striking differences between the calculated and measured results become apparent at the high tunnel speed at the inner part of the blade: At these conditions the measured tangential force drops to zero where the calculated data continue to rise, or at least remain at a value far above zero.

4.2.2 Ratios between measured and (PHATAS) calculated tangential forces as function of tunnel speed and pitch angle

In Figures 56 to 60, the ratios between the calculated and measured tangential forces is given. Only those data are presented where the ratios remain between reasonable limits (say between 1.0 and 2.0). Generally speaking this is true for low tunnel speeds, say between V_{tun} =5 m/s and $V_{tun} \approx 10$ m/s.

For higher tunnel speeds the the measured tangential forces approach zero (see the figures which are presented in section 4.2.1), where the calculated forces remain at much higher positive values. This makes the ratio between the calculated and measured values extremely large and nonsensical.

As a result, it can be concluded that the agreement between calculated and measured tangential forces is reasonable to good, as long as the tunnel speed is below 10 m/s (i.e. at below stall angles of attack). For higher tunnel speeds the differences are large where the calculated tangential force is (strongly) positive and the measured tangential force ≈ 0. This implies the prediction of too strong a force towards the leading edge similar to the observations made in [8] for other wind turbines. Although it should be recalled from section 2.1 that the measured tangential force is suspected to be rather inaccurate, the differences may also be caused by a too low drag force in the calculations. Alternatively it could be caused by a too high lift force in the calculations but this is unlikely in view of the underpredicted normal forces from the previous section.

4.3 Rotorshaft torque and flatwise moment

In this section the results of the blade root flatwise moment and the rotor shaft torque are analysed. Thereto section 4.3.1 presents the calculated and measured mean rotorshaft torque and flatwise moment as function of tunnel speed and pitch angle, where the measured and calculated results are given in separate figures. In section 4.3.2 the calculated and measured results are compared by presenting the ratios between the calculated and measured data.

The flatwise moment has been measured at the root of both blades. Usually the differences between the flatwise moments from the two blades appeared to be limited to 3-5% but in particular near a tunnelspeed of 10-11 m/s some (much) larger differences were found. The present comparison is based on the flatwise moment of blade 3 (i.e. the blade which is instrumented with pressure taps and five hole probes), since this quantity is expected to be most closely related to the local aerodynamics loads as discussed in the previous sections.

The flatwise moment is defined in the direction perpendical to the tip chord, positive in downwind direction.

4.3.1 Measured and (PHATAS) calculated rotorshaft torque and flatwise moment as function of tunnel speed and pitch angle

In Figure 61 and 63 the measured flatwise moments and rotorshaft torque are presented as function of tunnel speed. In Figures 62 and 64 the corresponding calculated results are given.

4.3.2 Ratios between measured and (PHATAS) calculated rotorshaft torque and flatwise moment

In Figure 65 the ratios between the calculated and measured flatwise moments and rotorshaft torques are presented (i.e. the data from Figure **??** are divided by the data from Figure **??**). The following observations can be made:

- For $V_{tun} < 14$ m/s, the flatwise moments are overpredicted. For higher tunnel speeds, the flatwise moments are underpredicted. This is consistent with the strong underprediction of the normal forces at the high tunnel speeds since the flatwise moment is strongly determined by normal force distribution along the blade.
- The rotorshaft torque is generally predicted well for $V_{tun} < 10$ m/s but at higher tunnel speeds there is a considerable overprediction. The overprediction is consistent with the strong overprediction in tangential forces, although the underprediction in normal force tends to reduce the overprediction of the torque.

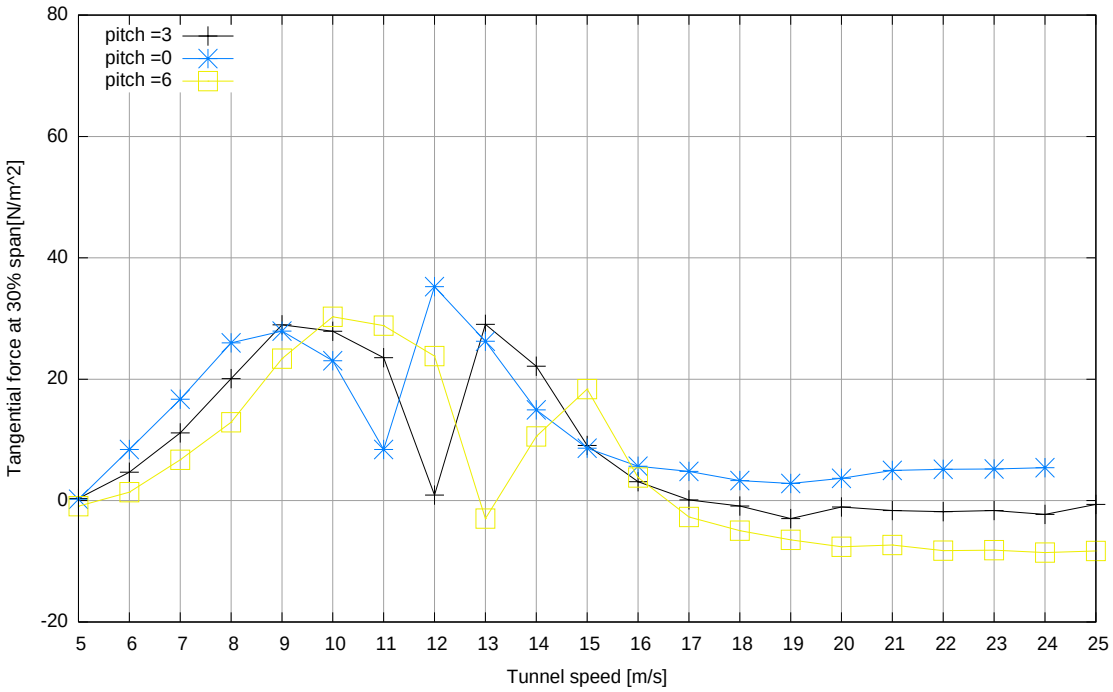

Figure 46: Measured tangential force as function of tunnel speed for 30% span

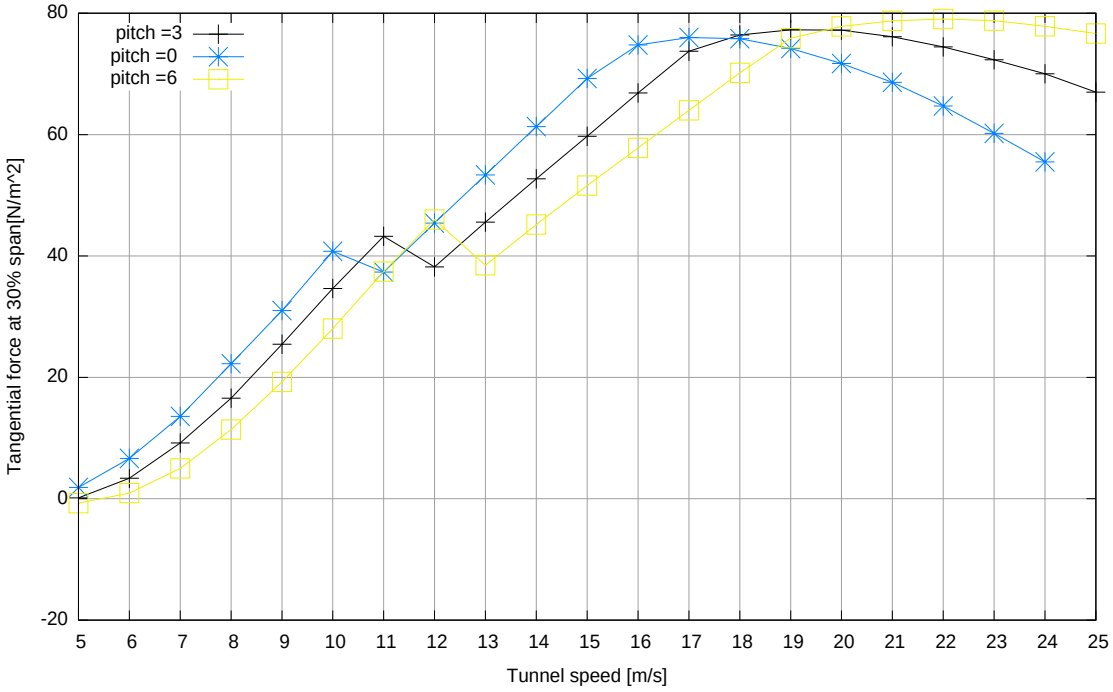

Figure 47: Calculated tangential force as function of tunnel speed for 30% span

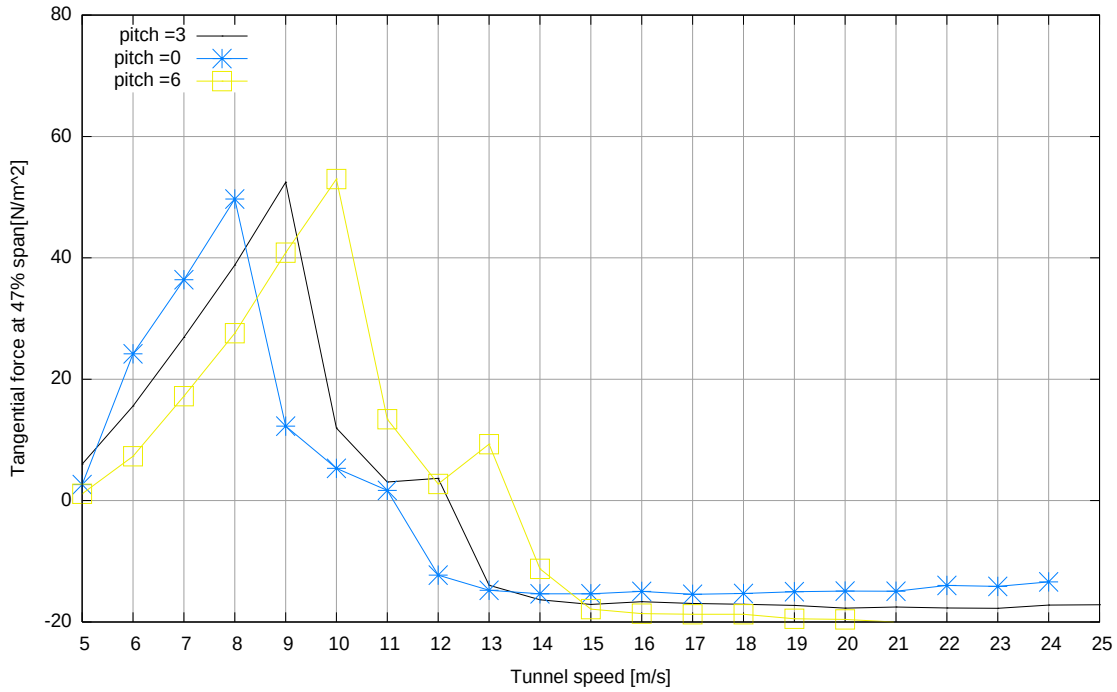

Figure 48: Measured tangential force as function of tunnel speed for 47% span

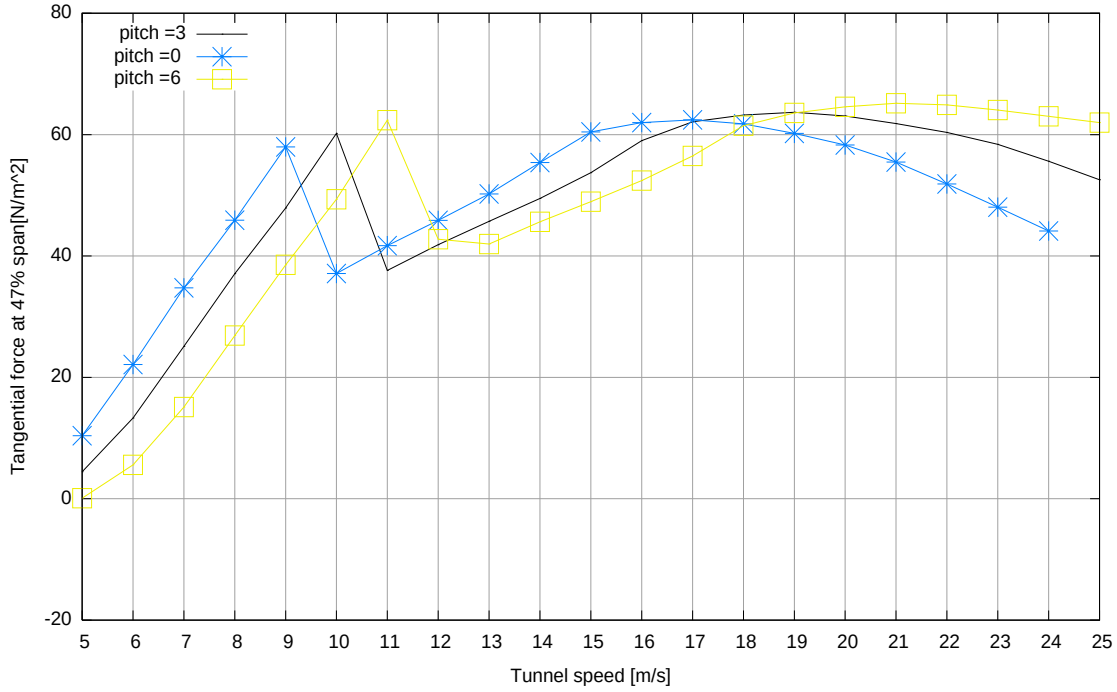

Figure 49: Calculated tangential force as function of tunnel speed for 47% span

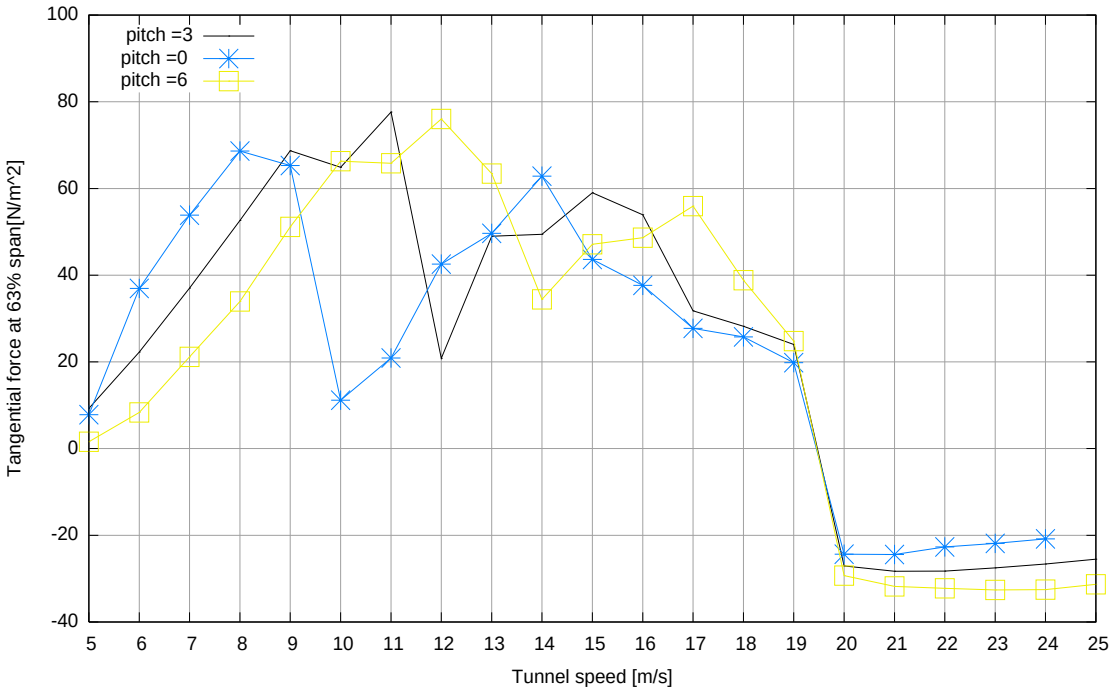

Figure 50: Measured tangential force as function of tunnel speed for 63% span

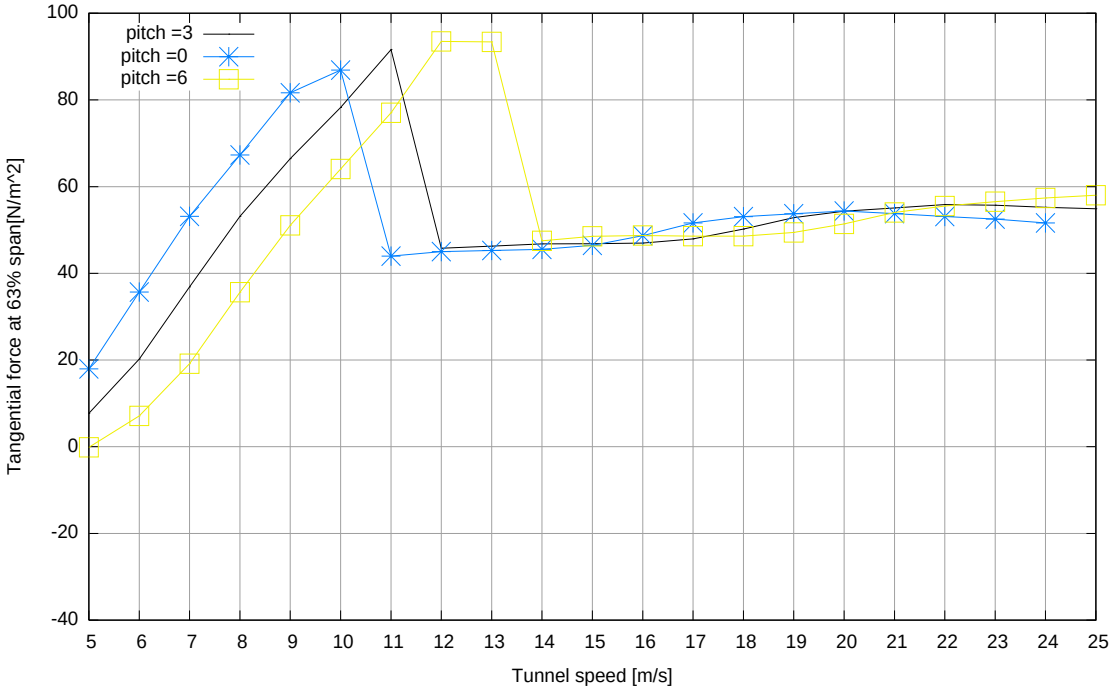

Figure 51: Calculated tangential force as function of tunnel speed for 63% span

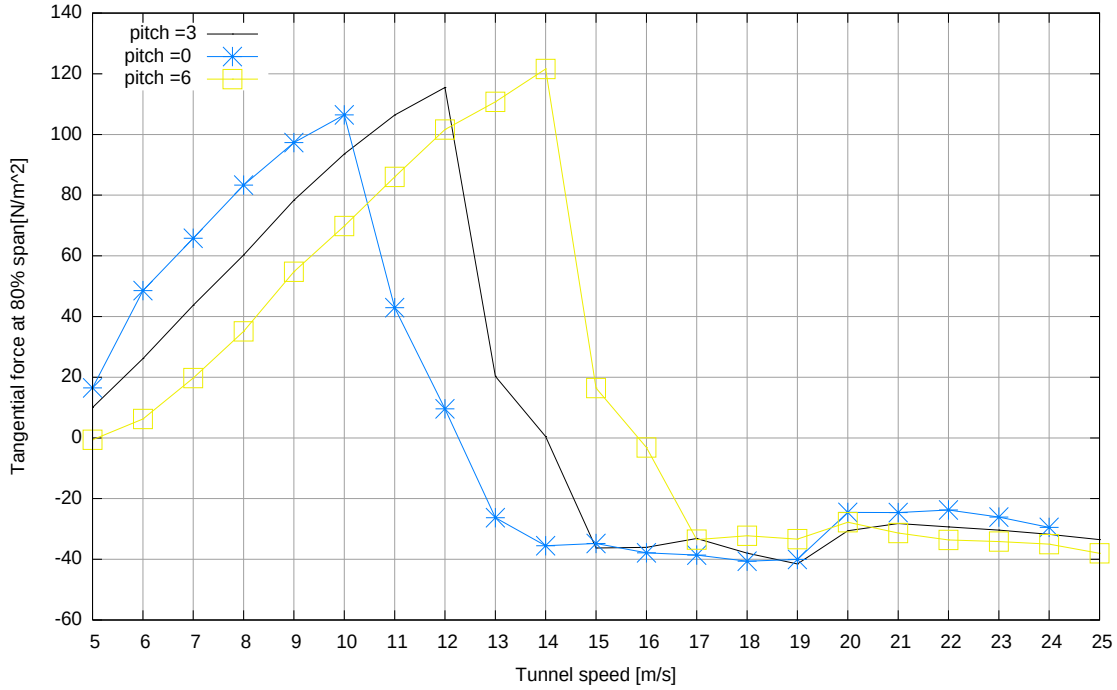

Figure 52: Measured tangential force as function of tunnel speed for 80% span

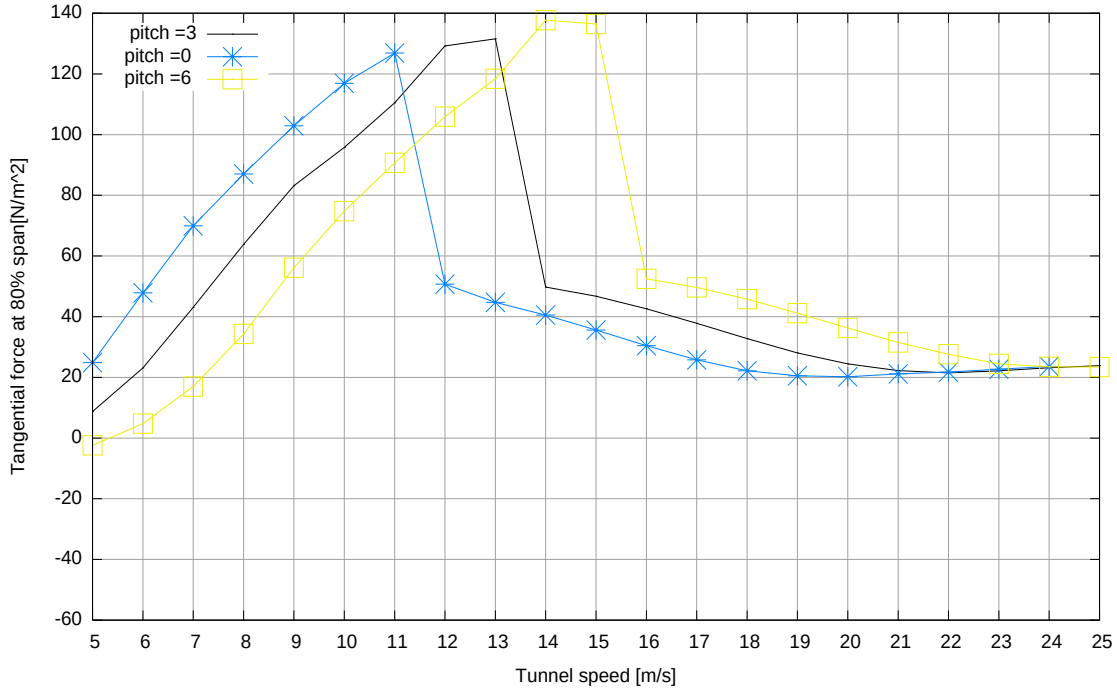

Figure 53: Calculated tangential force as function of tunnel speed for 80% span

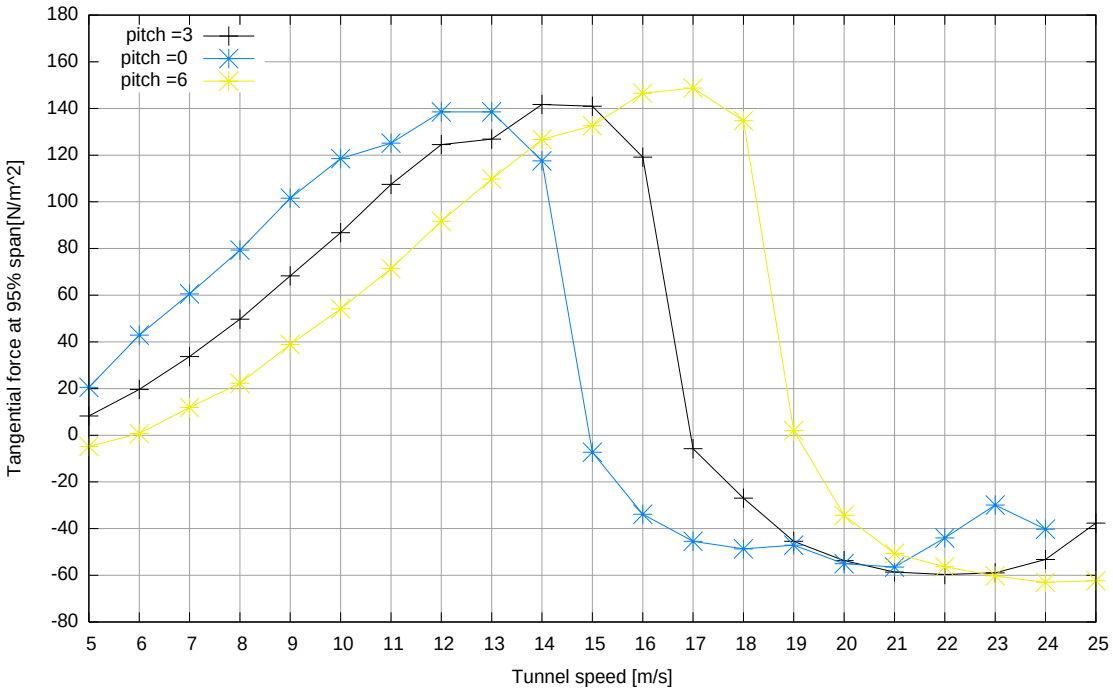

Figure 54: Measured tangential force as function of tunnel speed for 95% span

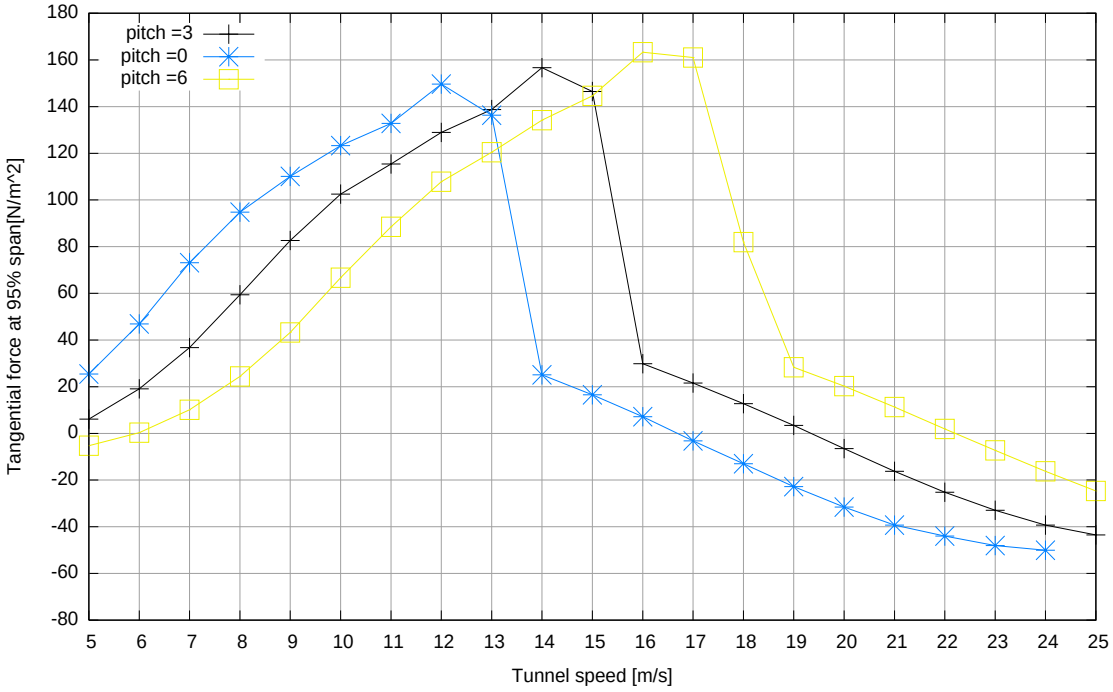

Figure 55: Calculated tangential force as function of tunnel speed for 95% span

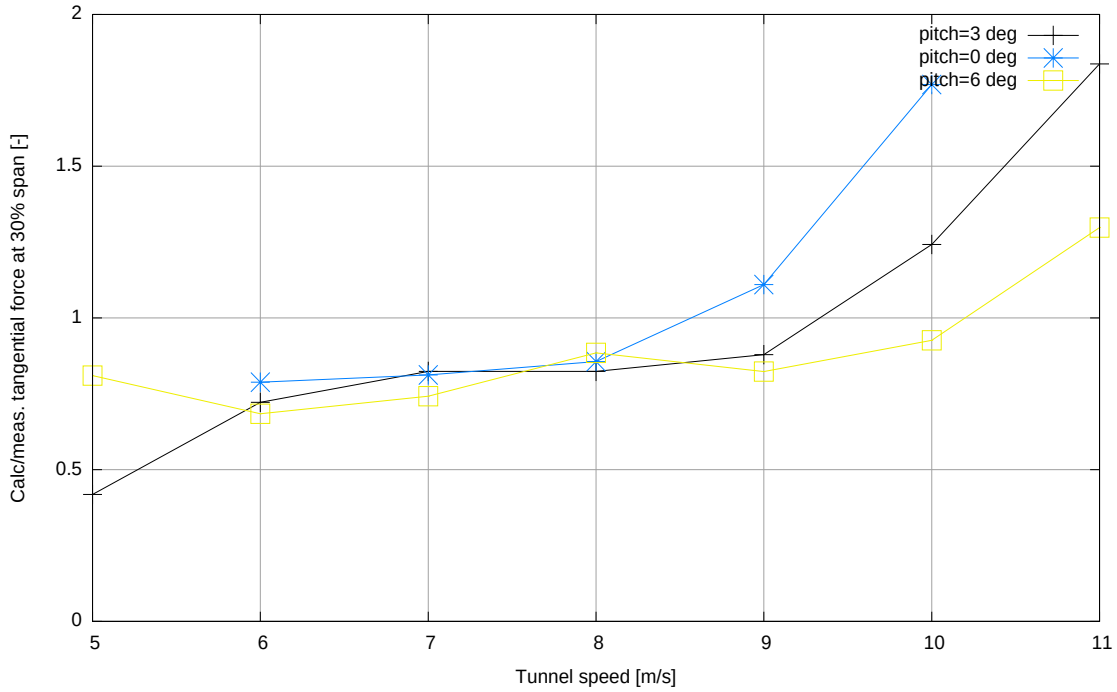

Figure 56: Ratio between calculated and measured tangential force as function of tunnel speed at 30% span

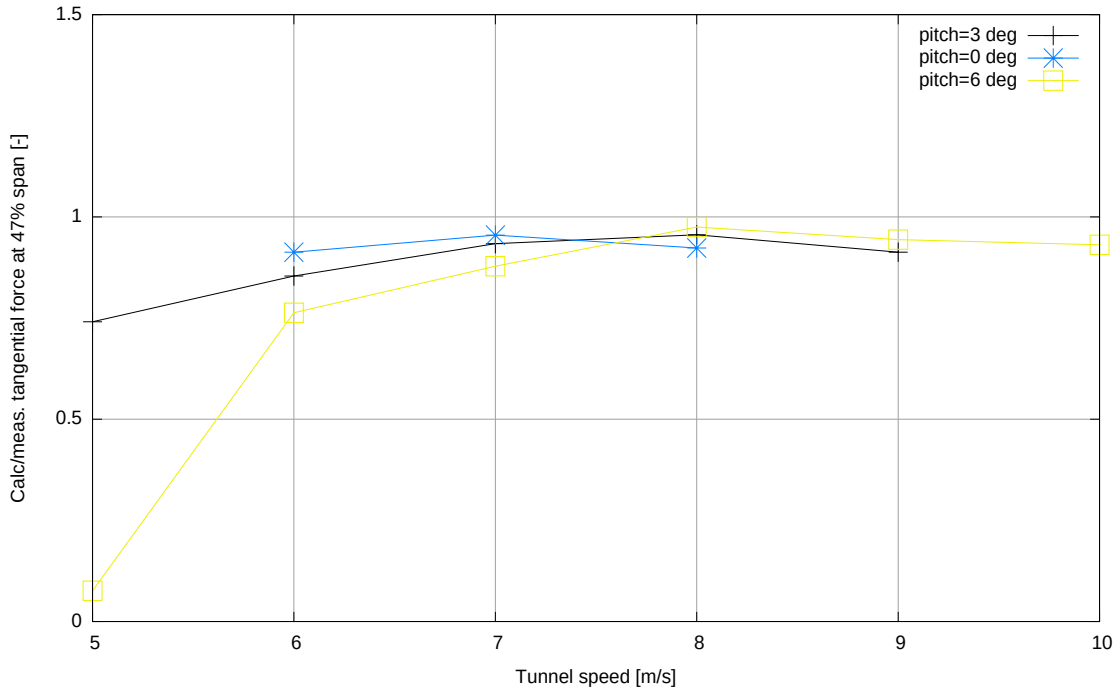

Figure 57: Ratio between calculated and measured tangential force as function of tunnel speed at 47% span

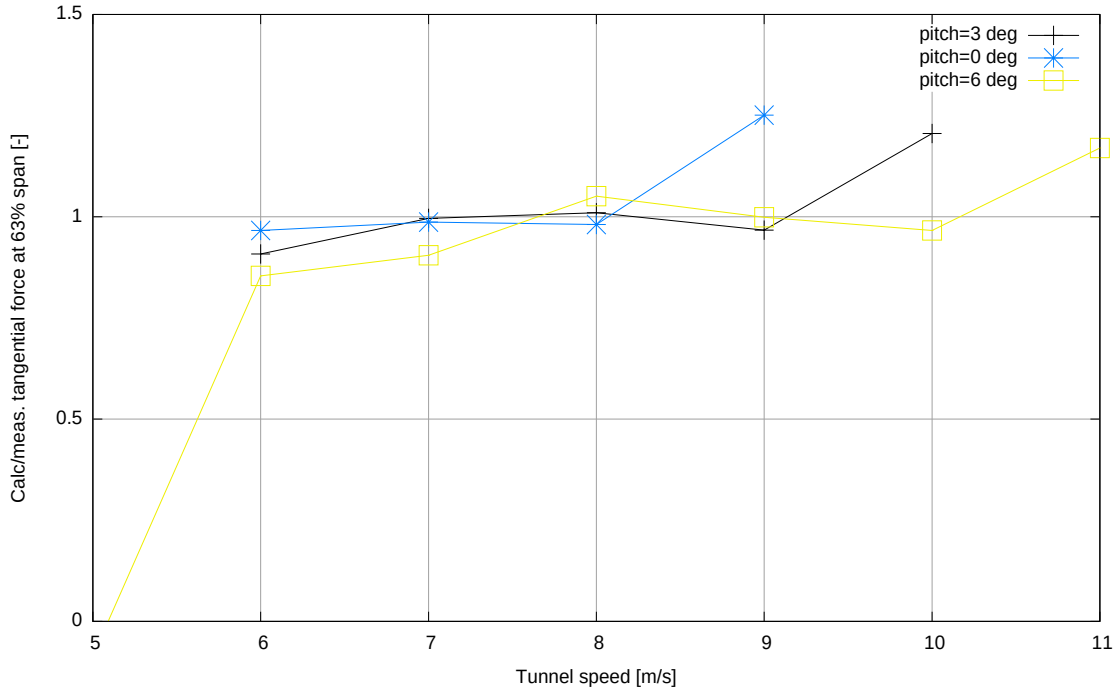

Figure 58: Ratio between calculated and measured tangential force as function of tunnel speed at 63% span

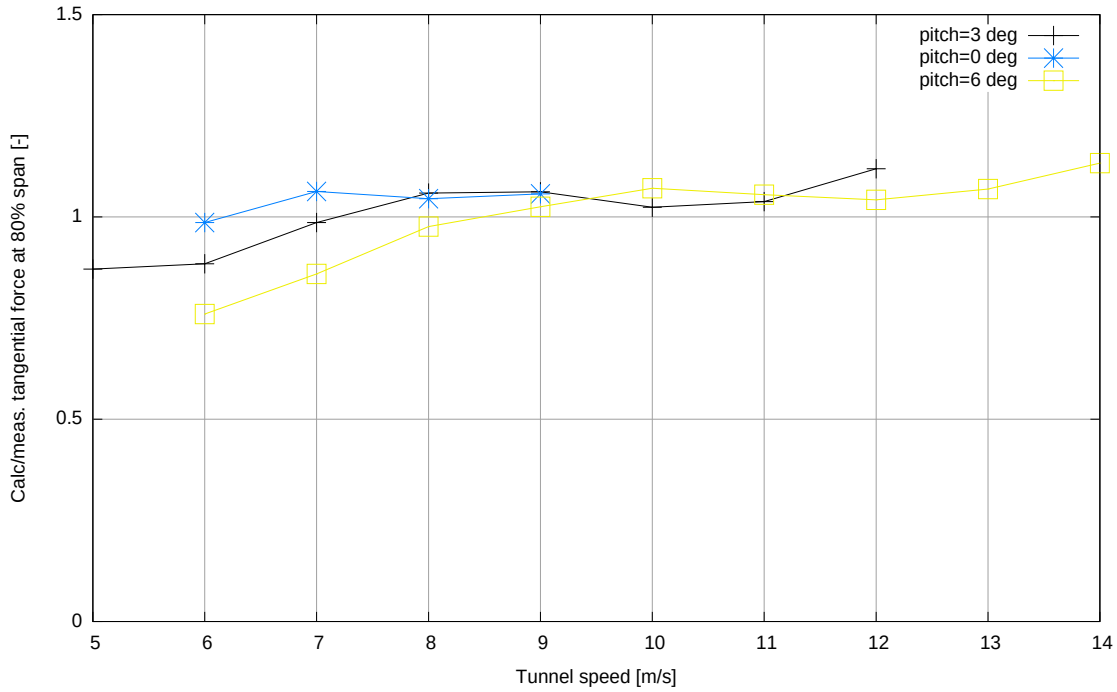

Figure 59: Ratio between calculated and measured tangential force as function of tunnel speed at 80% span

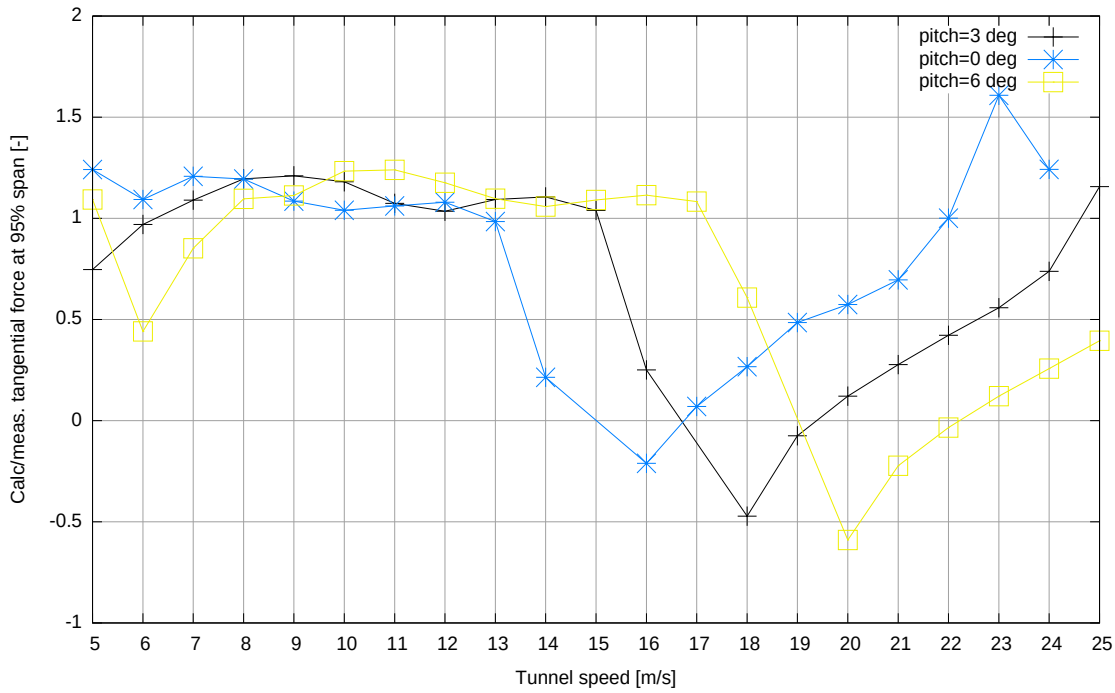

Figure 60: Ratio between calculated and measured tangential force as function of tunnel speed at 95% span

4.4 Summary of observations on the comparison between PHATAS calculations and measurements at high angles of attack

In the previous section the most pronounced differences have been found at large tunnel speeds (i.e. large angles of attack). These differences can be attributed to 3 dimensional (rotational) effects in stall since it is well known that these effects are difficult to model. The present calculations are based on the 3D model from [5] which is described in section 3.1. From the underpredicted normal forces at the inner part of the blade it can be concluded that this model predicts a too low increase in lift. The overpredicted tangential forces indicates an underprediction of the drag (note that currently no 3D correction on the drag coefficient is applied). Finally it is found that the 3D corrections should be made pitch angle dependent such that the strongest 3D correction is applied at small pitch angles. The physical explanation for the pitch angle dependancy lies in the fact that the 3D correction is 'driven' by an apparent Coriolis force in the rotorplane, which adds to the acceleration along the airfoil, where the angle between this force and this acceleration is approximately equal to the pitch (+twist) angle.

The observations are largely in line with earlier observations see e.g. [2]. These observation were however based on a direct assesment of the c_l and c_d coefficients as function of angle of attack. As mentioned before, these coefficients are disturbed by the uncertainty in dynamic pressure and angle of attack. The observations are also consistent with the findings from the Annexlyse project where the aerodynamic measurements on wind turbines in the free atmosphere are analysed, see section 5.2.

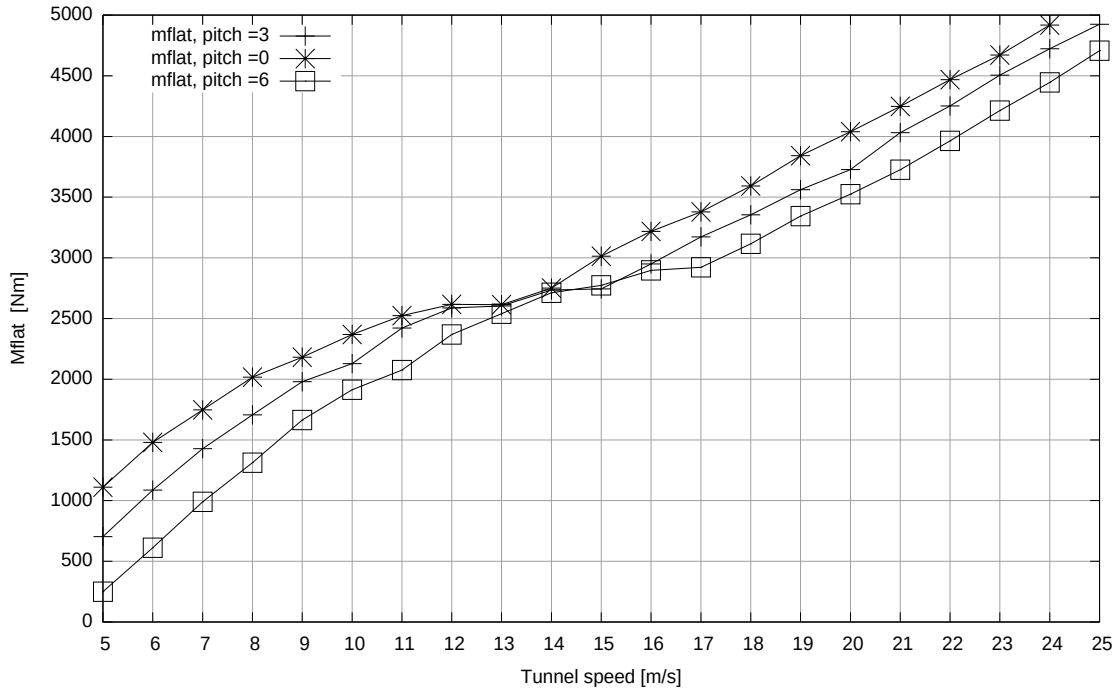

Figure 61: Measured flatwise moment as function of tunnel speed

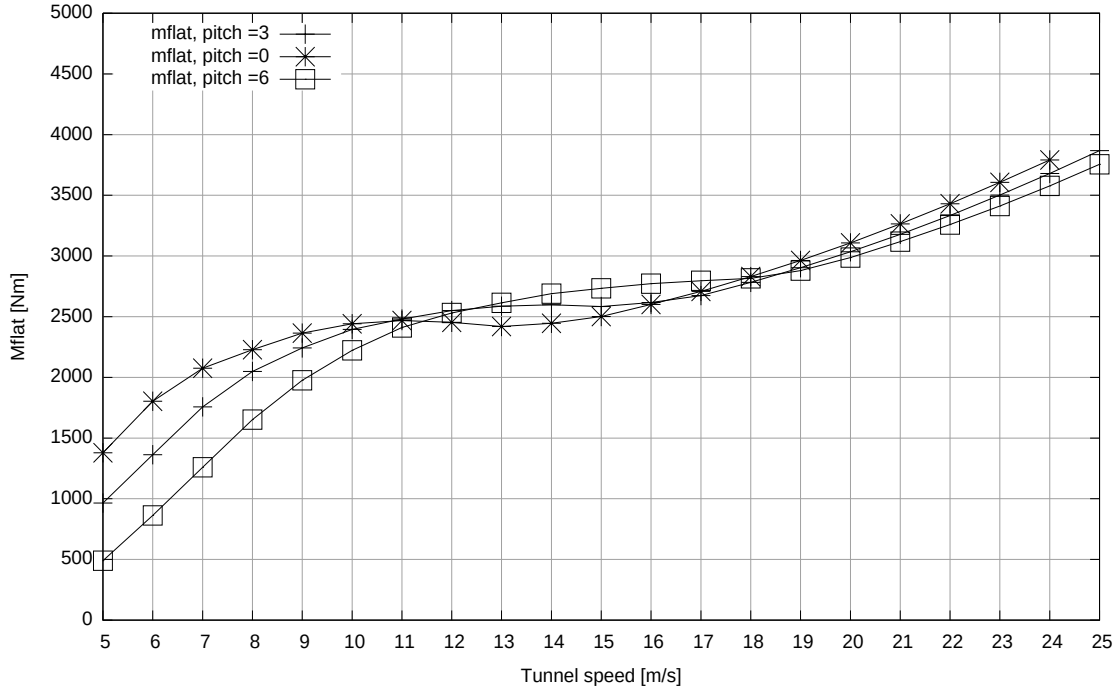

Figure 62: Calculated flatwise moment as function of tunnel speed

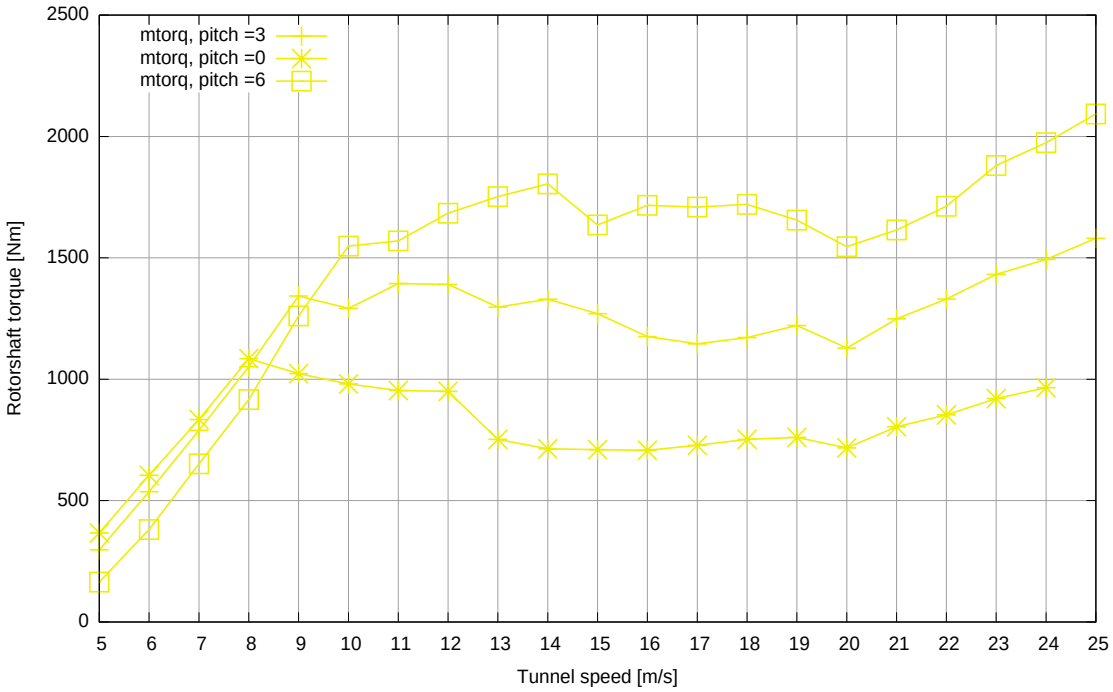

Figure 63: Measured rotorshaft torque as function of tunnel speed

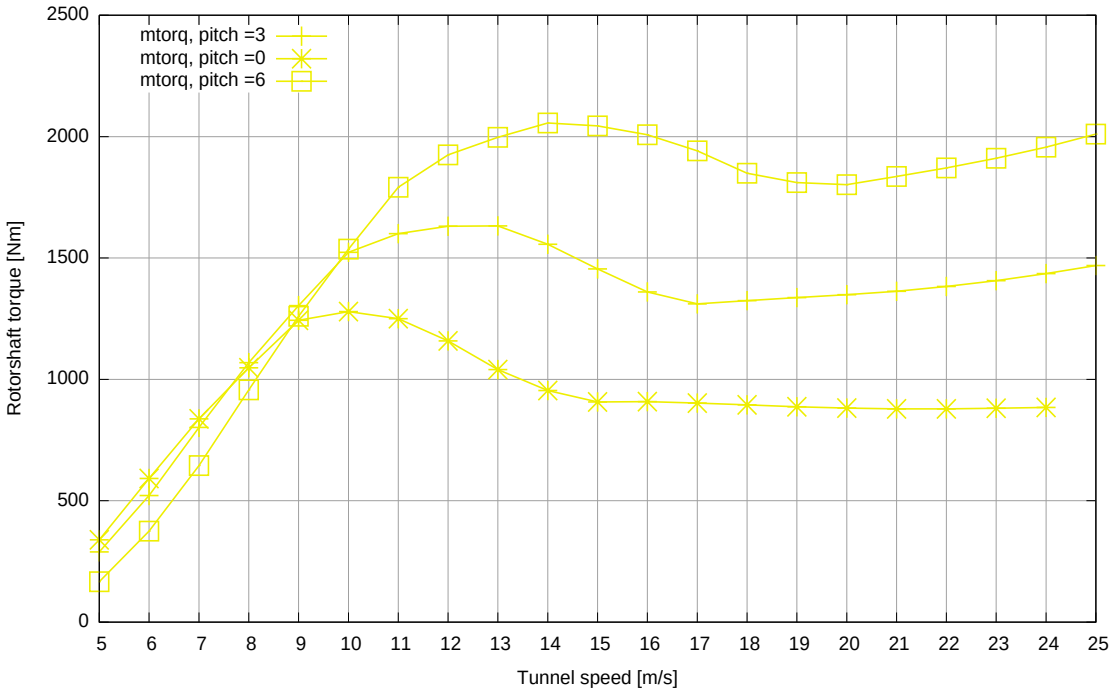

Figure 64: Calculated rotorshaft torque as function of tunnel speed

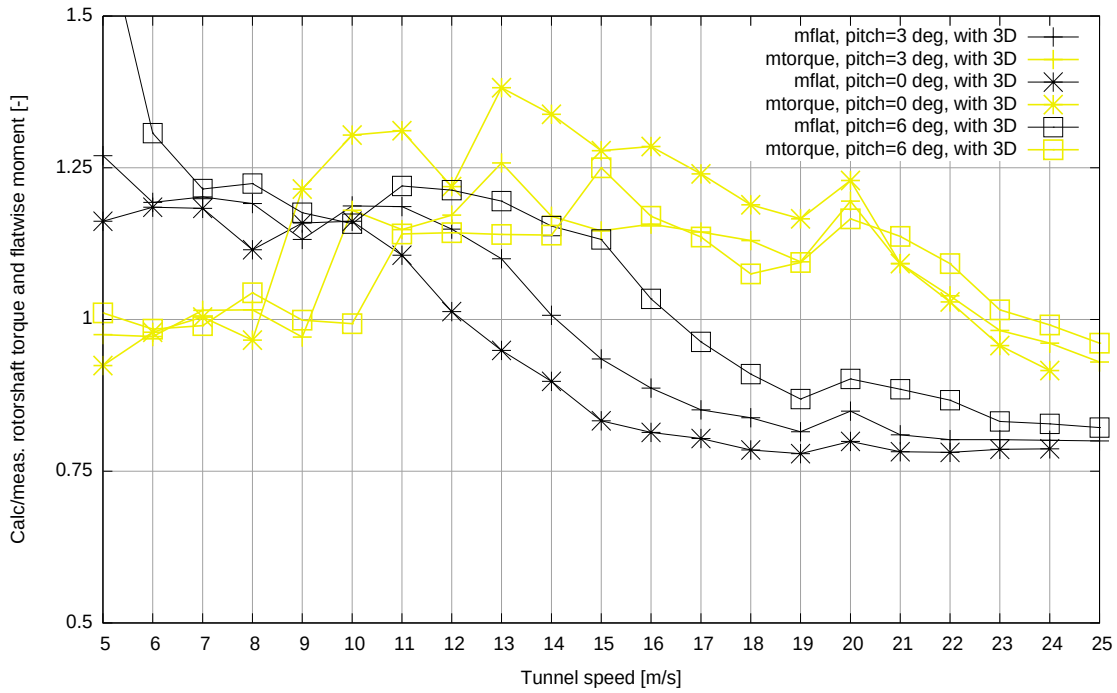

Figure 65: Ratio between calculated and measured flatwise moment and rotorshaft torque as function of tunnel speed

5 Effect of 3D (rotational) correction

5.1 Effect of 3D (rotational) correction as implemented in PHATAS

In order to assess the influence of the 3D stall correction, the PHATAS calculations have also been performed without this correction and compared to the calculations with the 3D correction. The calculations of the mean normal and tangential force at 30%, 63% and 80% span for a pitch angle of 3 degrees (Sequence H) are shown in Figures 66 and 67. As expected the influence of the 3D correction is mainly visible at the higher tunnel speeds and the inner part of the blade, where it increases the normal (and tangential) force. It can be concluded that the 3D correction generally improves the agreement between the calculated and measured normal forces at the high wind speeds, although as already observed in the previous sections, the normal forces at the inner part of the blade are still far too low. Generally speaking the agreement in tangential forces remains equally poor at the high wind speeds.

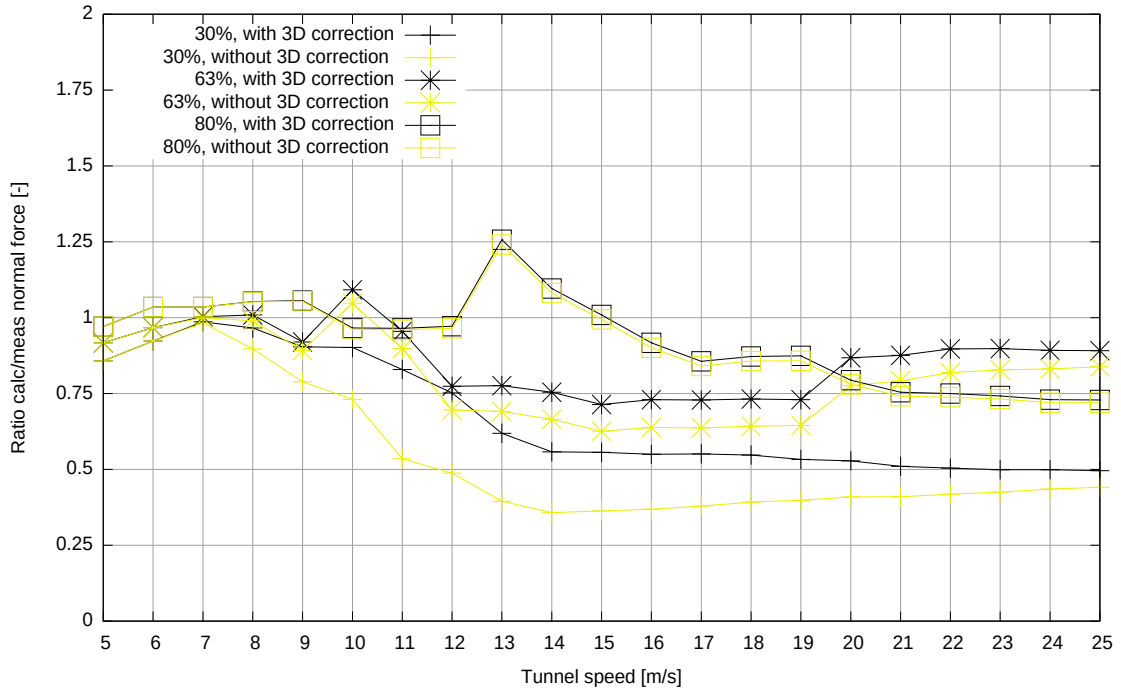

Figure 66: Calculated normal forces at 30%, 63% and 80% span and at θ = 3 degrees, with and without 3D correction

5.2 3D (rotational) correction from Annexlyse project

As already mentioned in section 4.4 the observations on the present measurements are largely in line with earlier observations made in the Annexlyse project, [8]. The main aim of the Annexlyse project was to analyse the measurements which have been taken within IEA Annex XVIII (http://www.ecn.nl/wind/other/IEA/index.en.html and [7]). In IEA Annex XVIII the pressure distributions and the resulting local aerodynamic forces have been measured at different spanwise locations. Measurements were available on 5 different turbines with diameters ranging between 10 and 28 m by which a general validation could be performed. Although the character of the measurement programs as performed in IEA Annex XVIII is largely comparable to the NASA-Ames measurements (in the sense that local aerodynamic forces are measured) a main difference lies in the fact that the IEA Annex XVIII measurements have been carried out at field conditions, where the NASA-Ames measurements have been taken in a wind tunnel environment.

In the Annexlyse project a comparison has been made between the IEA Annex XVIII measurements and calculations from the 'default' PHATAS version (using the 3D model from the equations 1 and 2, i.e. the same model as applied in the present study). The conclusions which were drawn from this comparison were very similar to the present conclusions (i.e. the normal forces

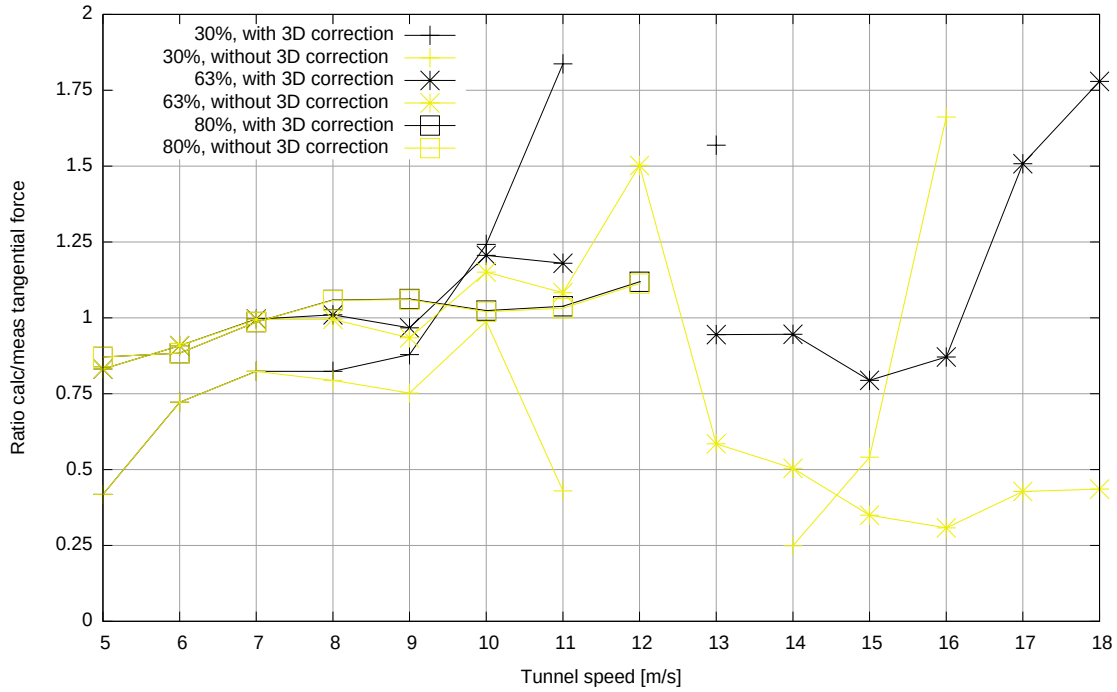

Figure 67: Calculated tangential forces at 30%, 63% and 80% span and at $\theta = 3$ degrees, with and without 3D correction

at the inner part of the blade are underestimated at high wind speeds where the tangential forces are overestimated. Furthermore a slight dependency of the 3D correction on the pitch angle is found). In addition the value of f_{cl}, showed a strong dependency on the angle of attack.

In a further attempt to improve the agreement between calculations and IEA Annex XVIII measurements, a 3D model was developed which was largely based on a previous model made by CRES, [10]. This CRES model already assumes an increased drag and it also takes into account a dependency on the pitch angle. Some further refinements were necessary (mainly by means of 'trial and error'), in order to include the dependency of f_{cl} on the angle of attack. The resulting model generally led to an improved prediction of the normal sectional forces and overall rotor(blade) loads. The agreement in tangential forces remained of the same order. It must be noted however that these observations are only true in a general sense and that many exceptions appeared.

In order to check the validity of this 'Annexlyse model' for the present NASA-Ames configuration, it has been used to simulate the measurements from the H-series (i.e. the measurements at a 3 degrees pitch angle). The results are presented in terms of ratios between calculated and measured normal forces, tangential forces, flatwise moments and rotor shaft torque, see Figures 68, 69 and 70.

A comparison between Figure 68 and Figure 16 reveals that the prediction of the normal force at the 30% section at the high wind speeds has improved (i.e the large underprediction has been corrected or it has turned into a smaller overprediction). However, the underprediction in normal forces at the other locations, as calculated by the default PHATAS version, has now turned into an overprediction of equal, or even larger, sign (compare the results from Figure 68 with the results from Figures 16 to 19). A more or less similar observation can be made on the comparison between calculated and measured tangential forces: The overprediction of tangential forces at higher tunnel speeds has now often turned into an underprediction.

As a net result the underprediction of the flatwise moment has turned into an overprediction of equal sign (compare Figure 70 with Figure 65) where the overprediction of the rotorshaft has even been enhanced. The latter observation is explained by the stronger overprediction in normal force which is apparently not sufficiently compensated by the underpredicted tangential forces.

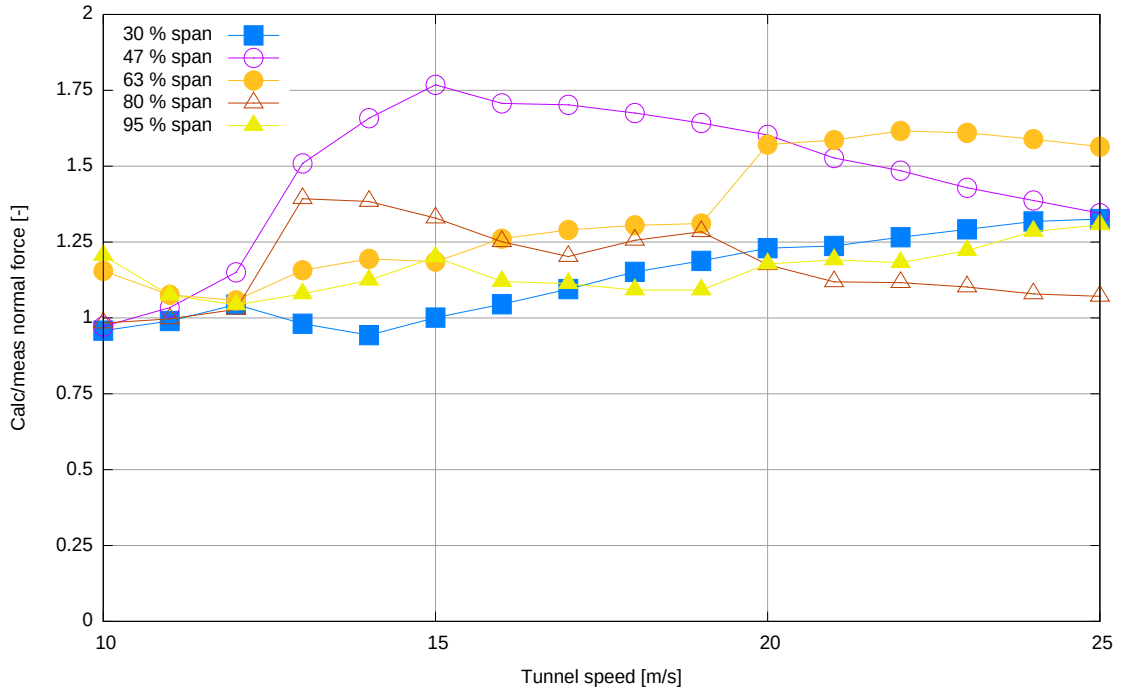

Figure 68: Calculated and measured normal forces as function of tunnel speed for θ = 3 degrees, using the corrections from the Annexlyse project

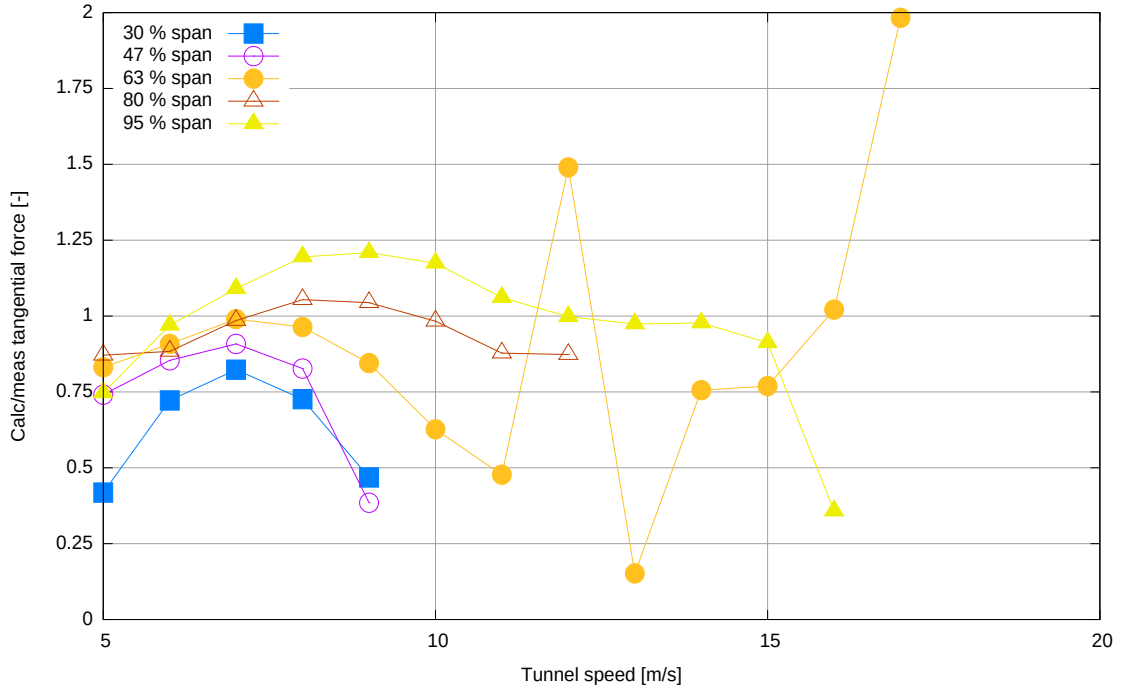

Figure 69: Calculated and measured tangential forces as function of tunnel speed for θ = 3 degrees, using the corrections from the Annexlyse project

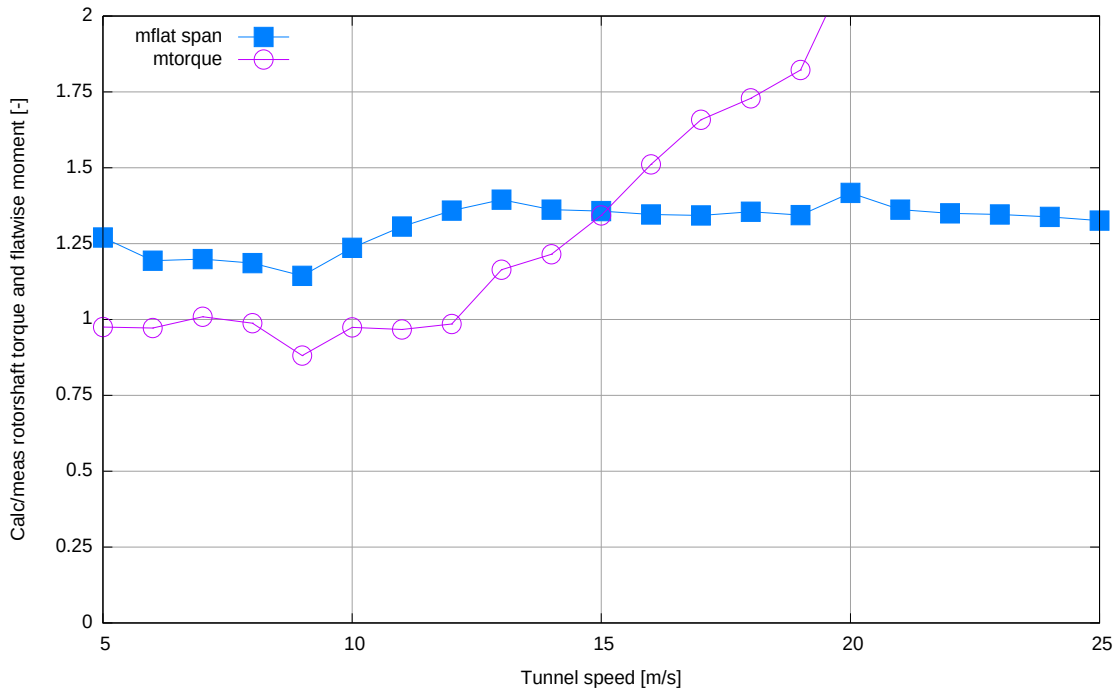

Figure 70: Calculated and measured rotorshaft torque and flatwise moment at $\theta = 3$ degrees, using the corrections from the Annexlyse project

6 Conclusions

- In the present report a comparison is made between calculated and measured loads on the NREL 10 m diameter wind turbine which was placed in the NASA-Ames wind tunnel. Measurements at non-yawed conditions have been considered where the tunnel speed ranges between 5 and 25 m/s and where the pitch angle varies between 0 and 6 degrees. Measurements of dimensional aerodynamic loads have been used as a basis for the comparison by which the uncertainty in dynamic pressure and angle of attack, which is often experienced in aerodynamic wind turbine measurements, does not play a role.

- Most investigated loads are predicted well with ECN's aero-elastic code PHATAS as long as the tunnel speed is relatively low (say below 10-12 m/s which corresponds to an angle of attack below the stall angle of attack). The most pronounced exception is the overprediction of the normal force at 95% span. This overprediction can be explained by the fact that the 2D airfoil characteristics which are used in the calculations, are incorrect near the very tip;

- At higher tunnel speeds, the PHATAS code underpredicts the normal forces and overpredicts the tangential forces. The latter observation implies the prediction of too strong a force towards the leading edge. These deficiencies are most likely caused by 3D effects in stall. It implies that the 3D correction from [5] as implemented in PHATAS yields a too low increase in lift coefficient, where at the same time the drag should be increased. It is noted that similar observations were found in the Annexlyse project, see [6], where field measurements on different turbines were analysed. The empirical corrections which have been derived from those measurements, lead for the present configuration, to an 'overcorrected' lift increase and drag increase;

- The overpredicted tangential force is reflected into an overprediction of the rotor shaft torque at the high tunnel speeds. The underpredicted normal force is reflected into an underpredicted flatwise moment;

- The calculations from the free wake lifting line code AWSM code (which are only performed for low tunnel speeds) show a good agreement with the measured loads. Even at the 95% span the agreement is reasonable and better than the agreement from the corresponding PHATAS calculation;

References

[1] A. van Garrel (2003): *"Development of a wind turbine aerodynamics simulation module "*. ECN-C –03-079, Energy Research Center of the Netherlands, ECN.

[2] C. Lindenburg (2003): *"Investigation into rotor blade aerodynamics, Analysis of the stationary measurements of the UEA Phase IV rotor in the NASA-Ames wind tunnel"*. ECN-C –03-025, Energy Research Center of the Netherlands, ECN.

[3] C. Lindenburg (2005): *"PHATAS – IV, Release "NOV-2003" and "Apr-2005" User's manual"*. ECN–I- 05-005, Energy Research Centre of the Netherlands, ECN.

[4] H. Snel (1997): *"Heuristic modelling of dynamic stall characteristics "*. Proceedings of the EWEC 1997 Conference held at Dublin. pages 429–433.

[5] H. Snel, R. Houwink and J. Bosschers (1993): *"Sectional prediction of lift coefficients on rotating wind turbine blades in stall "*. ECN-C –93-052, Energy Research Centre of the Netherlands, ECN.

[6] J.G. Schepers and R. van Rooij (2005): *"Final report of the Annexlyse project: Analysis of aerodynamic field measurements on wind turbines"*. ECN-C 05-064, Energy Research Center of the Netherlands, ECN.

[7] J.G Schepers et al (2002): *"Final report of IEA Annex XVIII' Enhanced Field Rotor Aerodynamics Database"'*. ECN-C- 02-016, Energy Research Centre of the Netherlands, ECN.

[8] J.G. Schepers, L. Feigl, R. van Rooij and A. Bruining (2004): *"Analysis of detailed aerodynamic measurements, using results from an aero-elastic code "*. Wind Energy Journal'. pages 7:357–371.

[9] M.M. Hand et al (2001): *" Unsteady Aerodynamics Experiment Phase VI Wind Tunnel Test Configurations and Available Data Campaigns"*. NREL/TP- 500-29955, National Renewable Energy Laboratory, NREL.

[10] P.K. Chaviaropoulos and M.O.L. Hansen (2000): *"Investigating 3D and rotational effects on wind turbine blades by means of a quasi-3D Navier Stokes Solver"*. Journal of Fluids Engineering, 122(2):330–336.

[11] R. van Rooij (2005): *"The effect of the test set-up on the steady state aerodynamic data (IEA-Annex XX)"*. Proceedings of the IEA Aerodynamics Symposium held at CENER, Pamplona.

A Airfoil data

Angle of attack deg	c_l [-]	c_d [-]	c_m [-]
-180.000	0.000	0.014	0.000
-175.000	0.474	0.028	0.237
-170.000	0.800	0.084	0.401
-160.000	0.642	0.256	0.252
-150.000	0.756	0.466	0.308
-140.000	0.764	0.678	0.338
-130.000	0.691	0.870	0.349
-120.000	0.557	1.026	0.347
-110.000	0.382	1.140	0.337
-100.000	0.181	1.206	0.322
-95.000	0.076	1.222	0.313
-90.000	-0.030	1.225	0.303
-85.000	-0.137	1.217	0.293
-80.000	-0.241	1.196	0.281
-75.000	-0.342	1.163	0.270
-70.000	-0.438	1.119	0.257
-65.000	-0.527	1.064	0.244
-60.000	-0.607	0.997	0.231
-55.000	-0.676	0.920	0.216
-50.000	-0.733	0.834	0.201
-45.000	-0.774	0.740	0.185
-40.000	-0.797	0.639	0.168
-35.000	-0.799	0.534	0.150
-30.000	-0.778	0.428	0.131
-25.000	-0.758	0.325	0.109
-22.000	-0.770	0.269	0.091
-21.000	-0.776	0.252	0.085
-20.000	-0.782	0.235	0.079
-19.000	-0.788	0.218	0.072
-18.000	-0.794	0.202	0.066
-17.000	-0.799	0.187	0.059
-16.730	-0.800	0.183	0.057
-14.630	-0.790	0.079	0.044

Angle of attack deg	c_l [-]	c_d [-]	c_m [-]
-12.630	-0.700	0.055	0.032
-10.730	-0.630	0.040	0.020
-8.730	-0.580	0.027	0.007
-6.730	-0.610	0.019	-0.005
-4.630	-0.400	0.013	-0.018
-2.630	-0.160	0.009	-0.031
-1.040	0.015	0.009	-0.041
-0.010	0.134	0.008	-0.043
1.020	0.253	0.009	-0.046
2.050	0.372	0.009	-0.049
3.070	0.491	0.009	-0.051
4.100	0.610	0.009	-0.054
5.130	0.729	0.009	-0.056
5.640	0.787	0.009	-0.057
6.160	0.842	0.009	-0.057
6.410	0.868	0.009	-0.056
6.670	0.882	0.010	-0.054
6.920	0.892	0.011	-0.052
7.180	0.902	0.013	-0.051
8.200	0.944	0.017	-0.044
9.210	0.973	0.021	-0.037
9.570	0.965	0.023	-0.038
10.200	0.952	0.026	-0.040
10.670	0.950	0.029	-0.037
11.210	0.947	0.033	-0.035
11.670	0.974	0.037	-0.038
12.230	1.007	0.046	-0.042
12.770	1.020	0.055	-0.042
13.220	1.031	0.062	-0.042
13.670	1.042	0.068	-0.042
14.230	1.055	0.069	-0.042
14.670	1.058	0.070	-0.042
15.229	1.062	0.080	-0.042
15.230	1.061	0.080	-0.042
15.231	1.061	0.080	-0.042
15.670	1.053	0.088	-0.043
16.220	1.043	0.097	-0.045
16.670	1.014	0.104	-0.045
17.200	0.979	0.121	-0.046
17.210	0.977	0.121	-0.046
17.570	0.900	0.133	-0.049
18.190	0.832	0.197	-0.054

Angle of attack deg	c_l [-]	c_d [-]	c_m [-]
19.000	0.826	0.211	-0.064
20.000	0.818	0.228	-0.075
21.000	0.809	0.245	-0.086
22.000	0.801	0.263	-0.097
23.000	0.792	0.282	-0.108
24.000	0.784	0.300	-0.118
25.000	0.777	0.320	-0.127
26.000	0.771	0.339	-0.136
28.000	0.766	0.379	-0.151
30.000	0.771	0.421	-0.162
32.000	0.783	0.463	-0.171
35.000	0.793	0.526	-0.183
40.000	0.791	0.630	-0.203
45.000	0.768	0.730	-0.222
50.000	0.728	0.823	-0.239
55.000	0.672	0.909	-0.256
60.000	0.604	0.985	-0.271
65.000	0.525	1.051	-0.285
70.000	0.437	1.106	-0.299
75.000	0.342	1.151	-0.311
80.000	0.242	1.183	-0.323
85.000	0.139	1.204	-0.335
90.000	0.034	1.213	-0.345
95.000	-0.071	1.210	-0.355
100.000	-0.175	1.195	-0.364
110.000	-0.374	1.129	-0.378
120.000	-0.548	1.017	-0.386
130.000	-0.681	0.863	-0.386
140.000	-0.754	0.674	-0.372
150.000	-0.747	0.463	-0.338
160.000	-0.634	0.255	-0.274
170.000	-0.800	0.085	-0.401
175.000	-0.474	0.029	-0.237
180.000	0.000	0.014	0.000

Table 2: 2D airfoil calculations